Role of oxidative stress and mitophagy in the development of amiodarone-induced pulmonary fibrosis

Inauguraldissertation
zur Erlangung des Grades eines Doktors der Humanbiologie
des Fachbereichs Medizin
der Justus-Liebig-Universität Gießen

vorgelegt von
Shalini Venkatesan
Aus
Madurai, Indien

Gießen, 2016

Aus der Universitätsklinik für Innere Medizin
Des Fachbereichs Medizin der Justus-Liebig-Universität
Med. Klinik und Poliklinik II
Leiter/Direktor: Prof. Dr. W. Seeger
Klinische Forschergruppe "Lungenfibrose"
Leiter: Prof. Dr. A. Günther

Gutachter

Prof. Dr. Andreas Günther

PD Dr. Eva Peters

Tag der Disputation

05-Apr-2017

Dedicated to my beloved family, friends & teachers...

TABLE OF CONTENTS

List of figures:

List of abbreviations:

µg	Microgram
µM	Micromolar
AD	Amiodarone
AECII	Alveolar epithelial cells type II
AECs	Alveolar epithelial cells
AIF	Apoptosis inducing factor
AIPT	Amiodarone induced pulmonary toxicity
AMBRA	Activating molecule in beclin-1 regulated autophagy
ARE	Antioxidant response element
ATG	Autophagy related genes
ATP	Adenosine triphosphate
BALF	Bronchoalveolar lavage fluid
BH3	Bcl-2 homology 3
BMP	bis(monoacylglycero)phosphate
Bnip3	Bcl-2/E1B-19kDa interacting protein 3
Bnip3L	Bcl-2/E1B-19kDa interacting protein 3-like
BPE	Bovine pitutary extract
BSA	Bovine serum albumin
C57Bl/6	C57 black 6
Ca^{2+}	Calcium ions
CC	Coiled coil
CE	Cholesterol esters
Cer	Ceramides
CMH	1-hydroxy-3-methoxycarbonyl-2,2,5,5tetramethylpyrrolidine
CO_2	Carbon dioxide
COX II	Cytochrome c oxidase subunit II
COX IV	Cytochrome c oxidase subunit IV
CQ	Chloroquine
CT	Chest tomography
Cyt C	Cytochrome C
DEA	N-destehylamiodarone
DFCP-1	double-FYVE containing protein-1
DMSO	Dimethyl sulfoxide

DPPC	Dipalmitoylphosphotidylcholine
Drp-1	Dynamin-related protein 1
DYm	Mitochondrial membrane potential
E.g.	Example
EDTA	Ethylenediaminetetraaceticacid
ELF	Epithelial lining fluid
EMT	Epithelial-mescenchymal transition
ER	Endoplasmic reticulum
ESR	Electron Spin Resonance
FC	Free cholesterol
FDA	Food and drug administration
FIP 200	Focal adhesion kinase family interacting protein of 200kDa
FW	Four tryptophan
GABARAP	Gamma aminobutyrate receptor associated protein
GbL	G-protein-b-subunit-like protein
GSH	Glutathione
HE	Hematoxylin-eosin
hEGF	human epidermal growth factor
HEPES	4-(2-hydroxyethyl)-1-piperazineethanesulfonic acid
HIF-1	hypoxia-inducible factor-1
HO-1	Heme oxygenase - 1
HPSIP	Hermansky-pudlak syndrome interstitial pneumonia
Hsc 70	Heat shock cognate 70
hSP-CI73T	Human surfactant protein C mutation of threonine for isoleucine at codon 73
ILD	Interstitial lung disease
Ischemia-reperfusion	IR
ITS	Insulin, transferrin, selenite
kDa	Kilodalton
Keap1	Kelch-like erythroid cell-derived protein with CNC homology [ECH]-associated protein 1
KGF	Keratinocyte growth factor
KIR	Keap interacting region
LAMP2A	Lysosomal-associated membrane protein 2A
LIR	LC3 interacting region

LPC	Lysophosphotidylcholine
MAP1LC3	microtubule-associated protein 1 light chain-3
mATG2	mammalian autophagy related genes 2
mATG9	mammalian autophagy related genes 9
MEFs	Mouse embryonic fibroblasts
ml	Millilitre
MLE12	Mouse lung epithelial 12 cells
mM	Millimolar
mPTP	Mitochondrial permeability transition pore
mtDNA	Mitochondrial DNA
mtDNA/gDNA	Mitochondrial to genomic DNA
mTOR	Membrane target of rapamycin
mTORC1	Membrane target of rapamycin complex 1
NAC	N-acetyl-L-Cysteine
NBR1	Neighbor of BRCA1 gene 1
NES	Nuclear export signal
NLS	Nuclear localization signal
nM	Nanomolar
Nrf2	Nuclear factor erythroid 2 [NF-E2]-related factor 2
PARL	Presenilins-associated rhomboid-like protein
PB1	Phox and Bem1
PC	Phosphotidylcholine
PE	Phosphotidylethanolamine
PE	phosphotidylethanolamine
PE-P	Phosphotidylethanolamine based plasmalogens
PG	Phosphotidylglycerol
PI	Phosphotidylinositol
PI3P	Phosphotidyl-inositol-3-phosphate
PINK1	PTEN-induced putative kinase 1
PL	Phospholipids
PMSF	Phenylmethylsulfonyl fluoride
PPARGC1A	Peroxisome proliferator-activated receptor gamma co-activator 1-alpha
PRAS40	Proline rich AKT substrate 40 kDa
proSP	Prosurfactant
PS	Phosphotidylserine

pSOD	Polyethylene glycol
Raptor	Regulatory associated protein of mTOR
ROS	Reactive oxygen species
RT	Room temperature
Sat	Saturated
siRNA	Small interfering RNA
SM	Sphingomyelin
SnPP	Tin protoporphyrin
SP	Surfactant protein
SQSTM1	Sequestosome
TEMED	N,N,N',N'-tetramethyl-1,2-diaminomethane
TGF-b	Transforming growth factor-b
TNF-a	Tumour necrosis factor - alpha
Ub	Ubiquitin
UBA	Ubiquitin-associated domain
ULK1	Uncoordinated-51 (unc-51) - like kinase 1
Unsat	Unsaturated
UPS	Ubiquitin proteasomal system
US	United States
UV	Ultraviotet
UVRAG	UV radiation resistance associated gene
V-ATPase	Vacuolar ATPase
Veh	Vehicle
WIPI1	WD repeat protein interacting with phosphoinositides 1
WIPI2	WD repeat protein interacting with phosphoinositides 2

1. Introduction

1.1. Amiodarone

1.1.1. Historical Perspective

Amiodarone (AD) is a bi-iodinated benzofuran derivative (Figure 1.1), that was described as an antianginal agent in the early 1960s. AD was later serendipitously found to suppress arrhythmias and was used by Argentinian physicians in 1970s to treat resistant arrhythmias. In 1985, the United States (US) Food and Drug Administration approved the use of AD for treating life-threatening ventricular tachyarrhythmia. The prescription of AD had doubled between 1989 and 1994, with a subsequent increase in use. According to Vaughan-Williams classification, AD is classified as class III antiarrhythmic agent, as it prolongs myocardial repolarisation homogenously *via* blocking the potassium channel. The drug also possesses some characteristics of class I, II and IV antiarrhythmic drugs (Papiris *et al*., 2010, Vassallo *et al.,* 2007).

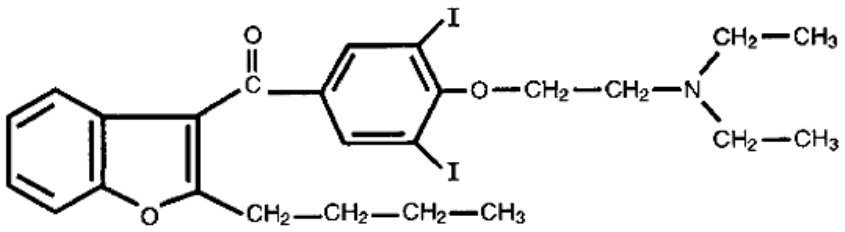

Figure 1.1: Chemical structure of AD. (Taylor *et al*., 2003).

1.1.2. Pharmacokinetics

Being a cationic (due to its N-diethyl amino side chain) amphiphilic drug, AD exhibits high lipophilicity. It hence has a very large volume of distribution (66L/Kg) leading to a delayed onset of action (from 2 days to 3 weeks in case of oral therapy) and a longer elimination half-life spanning from 13 to 142 days for the depletion of the tissue stores upon cessation of the chronic therapy, following a 50% reduction in the plasma concentration during the initial 3 to 10 days (Vassallo *et al.,* 2007, Dharmarajan *et al.,* 2008). AD is primarily metabolized in the liver by Cytochrome P450 (CYP) enzymes such as CYP2C8 and CYP3A4 and excreted in the faeces (Papiris *et al*., 2010, Vassallo *et al.,* 2007, Dharmarajan *et al.,* 2008). The excretion *via* the renal system is minimal (< 1% in urine) (Vassallo *et al.,* 2007).

1.1.3. Adverse effects

Despite its therapeutic potential, AD inflicts several cardiac and extra-cardiac side effects (Chang *et al.,* 2007) (Figure 1.2). Hence, standard guidelines recommend the prescription of AD by clinicians only in the absence of pre-excitation when other anti-arrhythmic agents are either contra-indicated or have failed (January *et al.,* 2014). The lipophilic moiety of the drug aids in the accumulation of the drug and its metabolite, N-desethylamiodarone (DEA) in high lipid content organs *viz* adipose tissue, thyroid, liver, lungs and other organs like eyes, skin, heart, neuromuscular system, gastrointestinal- and genitourinary- tract (Papiris *et al*., 2010). This results in potentially adverse effects such as hypo- (6%) and hyper- thyroidism (0.9 - 2%), hepatotoxicity (solely elevated liver enzyme levels, 15 - 30%; hepatitis and cirrhosis, < 3%), pulmonary toxicity (1 - 17%), microscopic corneal crystalline deposition (> 90%), blue-gray skin discolouration (4 - 9%), optic neuropathy/neuritis (≤ 1 - 2%), tremor and ataxia (3 - 35%), peripheral neuropathy (0.3%) and symptomatic bradycardia (Range *et al.,* 2013, Chang *et al.,* 2007, Vassallo *et al.,* 2007). Although AD mediated thyroid and ophthalmic off-target effects are more prevalent than AD-induced pulmonary toxicity (AIPT), the latter is often fatal (Papiris *et al*., 2010). AIPT (AD pneumonitis) was first reported in early 1980's in the US and similar cases were also documented in Europe (Chang *et al.,* 2007, Papiris *et al*., 2010).

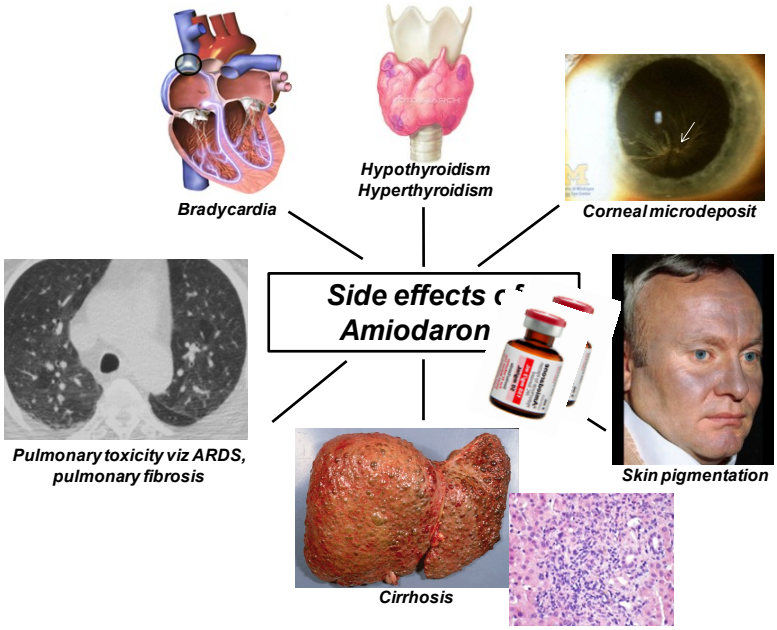

Figure 1.2: Potential side effects of AD.
(https://en.wikipedia.org/wiki/Bradycardia#/media/File:Blausen_0099_bradycardia.png, http://www.fotosearch.com/LIF001/9720b/,http://www.kellogg.umich.edu/theeyeshaveit/sideeffects/images/amiodarone.jpg,http://www.dermaamin.com/site/images/clinicalpic/a/amiodarone_hyperpigmentation/amiodarone_hyperpigmentation2.jpg,http://www.gastrohep.com/classcases/case29062007_fig_2.jpg,http://transplantationliver.com/wp-content/uploads/201308/Cirrhosis-Hospitals.gif, http://photos1.blogger.com/img/250/1358/1024/ Amiodarone%206.jpg).

1.1.4. Pulmonary toxicity of AD is part of the adverse effects

Two separate drug agency reports rank AIPT as the third and fourth common complications (approximately 11%) among all reported adverse effects of AD (Van Cott *et al.,* 2013; Ernawati *et al.,* 2008). The incidence of AIPT varies greatly depending on the various risk factors involved such as age, dose & duration of AD therapy (cumulative dosage) and pre-existing pulmonary disease (Papiris *et al*., 2010). An increased occurrence of AIPT has been reported in adult populations. In comparison with patients below 60 years of age, a threefold increase in risk of AIPT has been predicted for every 10 years of age in patients above 60 years of age (Ernawati *et al*., 2008). Rather than the serum levels, the incidence of AIPT could be better correlated with the cumulative dosage of AD. Patient cohorts receiving higher dosages of AD (≥ 400 mg/day) displayed increased frequency of developing severe pulmonary toxicity than patient cohorts receiving low doses (≤300 mg/day) (Papiris *et al*., 2010, Dharmarajan *et al.,* 2008). Around 6 % of the patients receiving 400 mg/day of AD for 2 or months develop AIPT, with a mortality rate of 10 - 20% (Chang *et al.,* 2007). Although lower doses of AD (200 mg/day) were considered to be safer alternative, reports have shown pulmonary complications even at low doses of AD therapy (Ott *et al.,* 2003, Chang *et al.,* 2007) (Figure 1.3). Patients receiving a cumulative dose of 10g - 150g of AD and/or for a time span of 6 -12 months present higher risks of developing AIPT (Papiris *et al*., 2010).

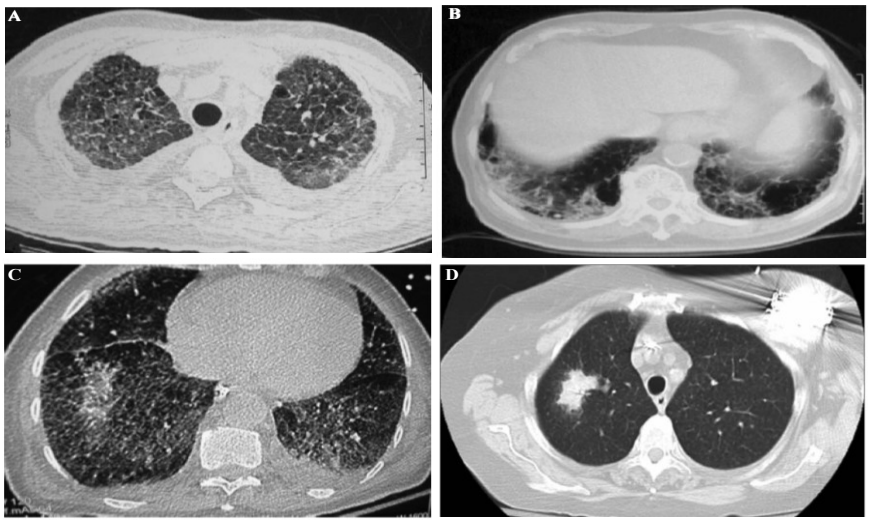

Figure 1.3: AIPT in patients receiving low AD dosage of 200mg/day.
Chest computer tomography (CT) of patients receiving 200 mg/day of AD- (**A**) -for 9 months, showing multiple ground-glass opacities in both lungs. (**B**) -for 6 months, showing fibrotic changes in both lungs with confluent fibrosis and honeycomb appearance evident in the lower part of both lungs. (**C**) -for one year, displaying bilateral pulmonary interstitial fibrosis. (**D**) -for four years, showing irregular hyperdense mass (amiodaronoma) in the right upper lobe of a patient. (Chang *et al.,* 2007, Dharmarajan *et al.,* 2008 and Jarand *et al.,* 2007).

Intravenous administration of AD may significantly increase the lung parenchymal concentration of AD even exceeding that of the heart (Papiris *et al.,* 2010). The active metabolite of AD, n-desethylAD, also harbour a longer half-life and penetrates tissues including lungs approximately five times more than AD (Vassallo *et al.,* 2007, Papiris *et al.,* 2010). Although pre-existing pulmonary disease was found to be associated with higher risk of AIPT, it did not increase the rate of pulmonary death (Olshansky *et al.,* 2005).

AIPT may clinically manifest in the form of pulmonary fibrosis, chronic interstitial pneumonia (CIP), bronchiolitios obliterans organizing pneumonia (BOOP), acute fibrinous and organizing pneumonia (AFOP), desquamative interstitial pneumonia (DIP), nodules or mass-like lesions (amiodaronoma) (Figure 1.3D), non-specific interstitial pneumonia (NSIP), idiopathic pulmonary fibrosis (IPF)-like interstitial pneumonia, diffuse alveolar haemorrhage (DAH), acute lung injury (ALI)/ acute respiratory distress syndrome (ARDS) or rarely as pleural/pericardial disease (Ott *et al.,* 2003, Papiris *et al*., 2010).

1.1.5. Mechanisms of AD-induced pulmonary toxicity

The precise molecular mechanisms underlying AIPT still remain obscure. It is however understood that, the interplay between several direct and indirect mechanisms such as cytotoxic insult, immune mediated inflammatory process and angiotensin system activation might contribute towards AIPT (Range *et al*., 2013, Jarand *et al.,* 2007) (Figure 1.4).

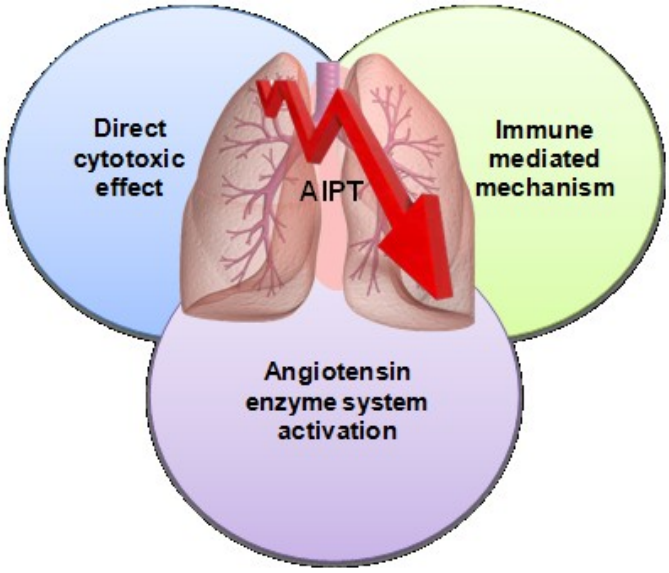

Figure 1.4: Possible mechanisms involved in AIPT.

AD-induced direct cytotoxicity involves accumulation of phospholipids, inhibition of mitochondrial function, generation of toxic oxygen radicals, disturbance of calcium homeostasis, inhibition of ionic pumps, alterations in physical properties of the cell membrane and influence on the activity of G proteins (Baritussio *et al.,* 2001, Range *et al*., 2013). The direct exposure to AD induces apoptosis in various mammalian lung cell types including human alveolar epithelial cells (AECs) *in vitro* (Bargout *et al.,* 2000).

As a cationic amphiphilic compound, AD accumulates in the acidic milieu of the lysosomes to levels higher than the extracellular concentration and inhibits lysosomal phospholipases *viz* phospholipase A_1 and A_2 (Baritussio *et al.,* 2001), thereby blocking phospholipid catabolism. This results in the accumulation of phospholipid-bound AD within the lysosomes of cells such as macrophages, type II pneumocytes, endothelial cells, interstitial and other intra-alveolar inflammatory cells of the lung and cells within other organs, thus leading to phospholipidosis. The drug induced phospholipidosis takes the form of a "foamy cell response", where whorled ultrastructural lamellar inclusion bodies are found in the foamy lipid-laden macrophages (Jarand *et al.,* 2007, Papiris *et al.,* 2010) (Figure 1.5).

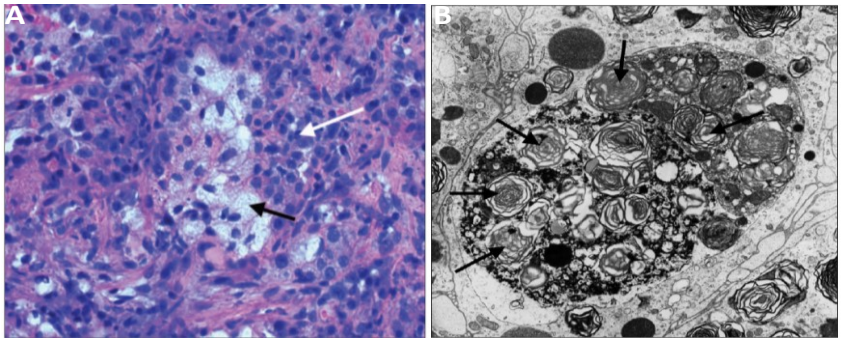

Figure 1.5: Foamy macrophages in AIPT.
(**A**) Hematoxylin-eosin (HE) staining of percutaneous fine-needle aspirate of the right upper lung lobe of a patient treated with AD (200 mg/day) for four years displaying numerous myofibroblasts and aggregates of foamy macrophages (black arrow) and chronic interstitial inflammation (white arrow). (**B**) Transmission electron micrograph of the same patient showing multiple lamellar bodies within macrophages. (Jarand *et al.,* 2007).

Such laminated inclusions are also witnessed in other hereditary lysosomal storage diseases *viz* the Niemann-Pick disease, Fabry disease and other amphiphilic drug induced phospholipidosis (Chung *et al.,* 2005). When such foamy cells occupy the intra-alveolar or the interstitial region, they may effectively reduce the surface for gas exchange. This type of storage lung disorder is referred as "lipoid pneumonia" (Papiris *et al.,* 2010, Bedrossian *et al.,* 1997).

AD is also a potential mitochondrial toxicant, well known to cause mitochondrial dysfunction and generate reactive oxygen species (ROS) (Nicolescu *et al.,* 2008; Bolt *et al.,* 2001). The negative membrane potential of the inner mitochondrial membrane drives the accumulation of this cationic drug into the mitochondria. AD gets protonated in the acidic intermembrane space and accrues electrophoretically into the mitochondrial matrix, where it releases the acquired proton due to the alkaline milieu. This leads to an initial uncoupling effect. Further, the concentrated drug in the matrix inhibits β-oxidation of fatty acids and also hinders complex I and complex II of the respiratory chain, thereby decreasing ATP formation (Fromenty *et al.,* 1990a,b, Felsar *et al.,* 2013). This respiratory chain inhibition results in enhanced ROS formation, which eventually induces lipid peroxidation. These events might further hamper the respiratory chain, thereby inflicting even more oxidative damage, ultimately resulting in rapid loss of mitochondrial membrane potential (ΔΨm), release of cytochrome c (Cyt C) and cell death (Begriche *et al.,* 2006; Marceau *et al.,* 2012).

Immunological mechanisms such as an imbalance between T helper (Th) type I and type II lymphocyte subpopulations and production of cytokines *viz* tumour necrosis factor-α and transforming growth factor-β (TGF-β) have also been implicated in contributing to AIPT. (Chung *et al.,* 2001, Papiris *et al*., 2010, Van Cott *et al.,* 2013). The third mechanism proposed to be involved in AIPT is the angiotensin II, which is chronically induced during congestive heart failure. Angiotensin II has been demonstrated to enhance AD mediated apoptosis of human lung AECs (Nikaido *et al.,* 2010) and promote fibrosis in a rat bleomycin model by stimulating angiotensin II type I receptor and TGF-β (Otszka *et al.,* 2004). AD-induced apoptosis of AECs was significantly abrogated by angiotensin converting enzyme inhibitor (Captopril) and angiotensin receptor blocker (Losartan) *in vitro* (Bargout *et al.,* 2000, Uhal *et al.,* 1998). AD-induced pulmonary fibrosis in rats was also averted by co-administration of angiotensin system antagonists Captopril or Losartan, which was evident by reduced incidence of alveolar epithelial cells type II (AECII) apoptosis and decreased collagen deposition in the alveolar walls (Uhal *et al.,* 2003).

1.1.6. Murine model of AD-induced pulmonary fibrosis

Since a murine model for AD-induced pulmonary fibrosis had not been described earlier (except a study elaborating the protective effects of the neferine in AD treated mice), a systemic analysis of surfactant alterations, lysosomal and endoplasmic reticulum (ER) stress had been performed and published recently by our research group (Mahavadi *et al.,* 2014).

Intratracheal administration of AD (0.8mg/kg) in C57 black 6 (C57BL/6) mice on every fifth day resulted in the development of full blown fibrosis in the lungs with marked septal thickening, patchy interstitial fibrosis, lymphoplasmacellular infiltration, extracellular matrix deposition (marked by increased collagen) and increased AECII size from day 7 onwards in comparison to the vehicle (Veh) treated C57BL/6 mice (Figure 1.6 A - C). Decreased lung compliance and increased lung hydroxyproline levels have also been reported in this model (Figure 1.6 D and E). Transmission electron micrographs of day 7 of AD treated mice revealed fragmented alveolar lining, denuded basal lamina and interstitial edema (Mahavadi *et al.,* 2014) (Figure 1.6 F).

Bronchoalveolar lavage fluids (BALF) obtained from AD treated mice displayed a prominent increase in the total phospholipids (PL), with modest changes in the PL profile in the lipidomics analysis of the alveolar surfactant pool (Mahavadi *et al.,* 2014).

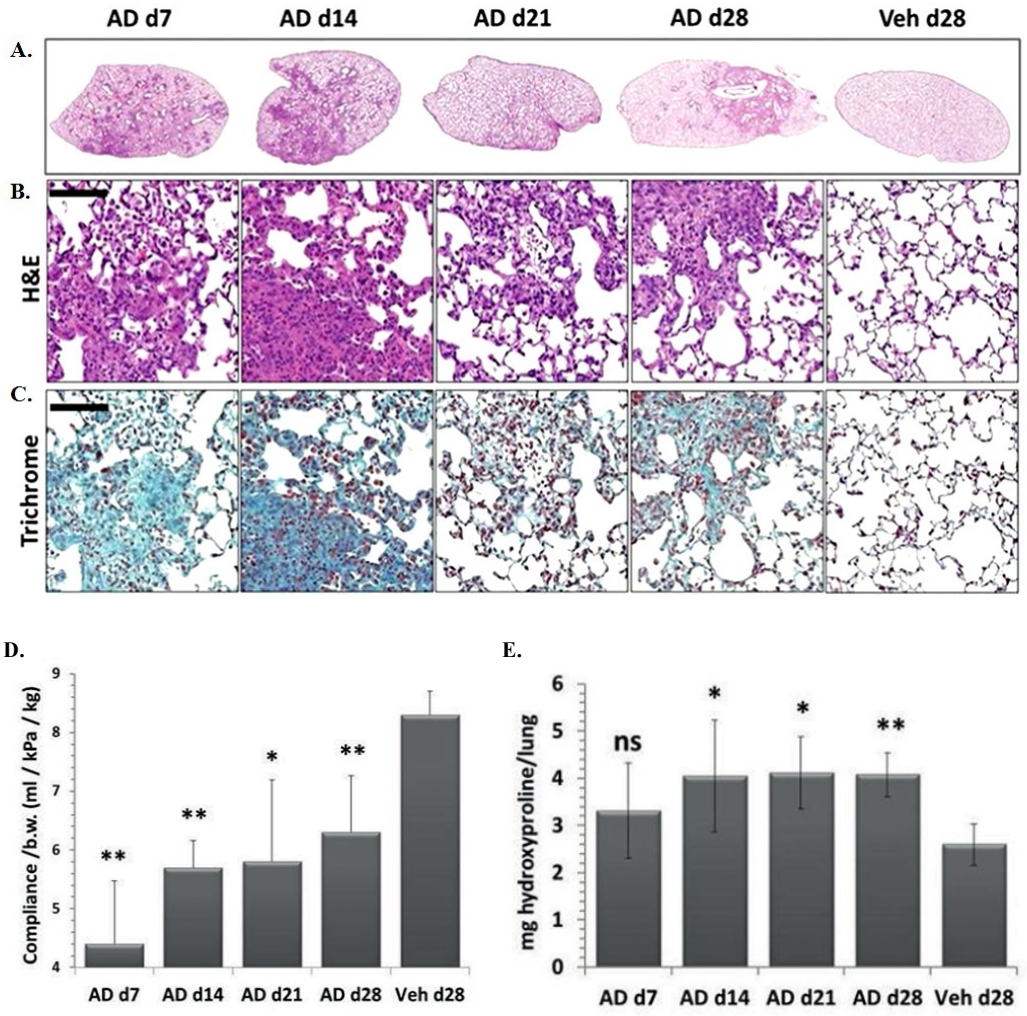

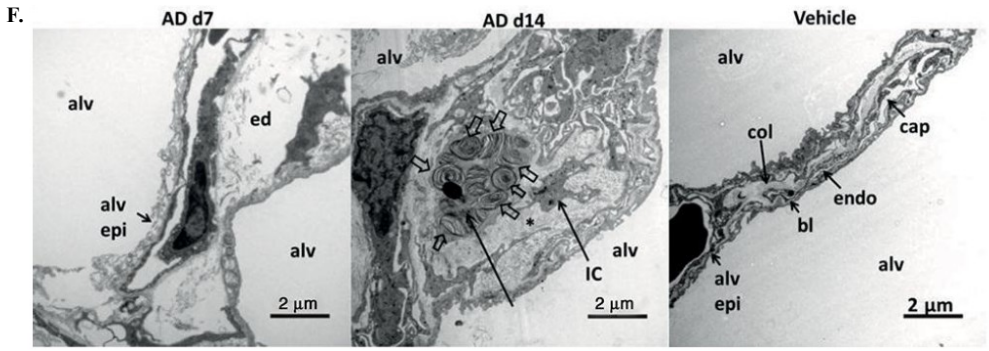

Figure 1.6: AD-induced pulmonary fibrosis in C57Bl/6 mice. (A, B, C) H&E and trichrome staining showing the development of fibrosis and increased collagen deposition in the complete left lung of C57Bl/6 mice from day 7 until day 28 of AD treatment. (D) Graphical representation of decreased lung compliance and (E) increased hydroxyproline content in the total right lung of day 7, 14, 21 and 28 of AD treated mice. (F) Transmission electron micrographs showing fragmented alveolar lining, denuded basal lamina and interstitial edema in day 7 of AD treated mice lung tissue and thickened septal walls (asterisk) and AECII with abundant and enlarged lamellar bodies (block arrows) in day 14 of AD treated mice lung tissue. Alv: alveolar space, alv epi: alveolar epithelium, ed: edema, bl: basal lamina, col: collagen, endo: endothelium, cap: capillary. (Mahavadi *et al.,* 2014).

Same analysis also revealed distinct changes in the fatty acid profiles, where a significant reduction in dipalmitoylphosphotidylcholine (DPPC), saturated phosphotidylcholine (PC) and saturated phosphotidylglycerol (PG) had been observed with their respective unsaturated counterparts (unsaturated phosphotidylcholine and unsaturated phosphotidylglycerol) reportedly increased in the BALF of AD treated mice (Mahavadi *et al.,* 2014). Phosphotiylethanolamine based plasmalogens (PE P) were also increased in the AD treated BALF samples. Mature forms of surfactant proteins (SP), SP-B and SP-C remained unchanged between the BALF of AD- versus Veh- treated mice (Mahavadi *et al.,* 2014).

Not just the BALF of AD treated mice; the lungs of the AD treated mice as well displayed an increased amount of PL. In addition, significantly increased levels of surfactant proteins (prosurfactant (pro) proteins: proSP-B and proSP-C and mature surfactant protein forms: mature SP-B and mature SP-C) were witnessed in AD treated mice lungs versus the Veh and an increase in proSP-C were also noted in AD treated mouse lung epithelial (MLE)12 cells (MLE12) for various time points (8-, 16- and 24- hours of AD treatment) (Figure 1.7 C). Corroborating this, an increased number and size of lamellar bodies were observed in hyperplastic AECII found around the areas of interstitial fibrosis in day 14 of AD treated mice lung with abundant intra-alveolar surfactant. In addition, lipidomics analysis from the lungs of AD treated mice revealed a significant increase in bis (monoacylglycero) phosphate (BMP)/ lysobisphosphatidic acid (LBPA), the biomarker for AD-induced phospholipidosis that is present within the internal vesicles of multivesicular bodies (MVBs) alongside with

cholesterol esters and other PLs were also elevated in the lipidomics analysis of AD treated mice lungs (Mahavadi *et al.,* 2014).

Three different theories have been proposed regarding the mechanism by which chronically injured AECII could drive lung fibrosis (Günther *et al.,* 2012). The first theory believes in the epithelial-mesenchymal transition (EMT), where the injured epithelial cells are suggested to transdifferentiate into active fibroblasts, which proliferates and results in fibrosis. The second theory claims a loss of control over the mesenchymal cells by the dying AECII and releasing a number of pro-fibrotic factors *viz* TGF-β and factor X, facilitating the fibroblast proliferation and collagen synthesis leading to pulmonary fibrosis. The third suggested mechanism is the chronically injured AECII releasing factors such as stromal cell-derived factor-1 by, which would attract the circulating fibrocytes into lung and aid in the expansion of the local fibroblast population, thus developing fibrosis (Günther *et al.,* 2012).

Under AD treatment, significantly increased apoptosis of AECII had been documented accompanied with elevated lysosomal and ER stress. Prominently increased amounts of apoptosis protein: cleaved caspase 3, lysosomal protein: cathepsin D and ER stress marker proteins: activating transcription factor (ATF) - 6 and C/EBP homologous protein (CHOP) were found in the lung homogenates of AD treated mice against the Veh treated control mice (Figure 1.7 A and B) and in 8-, 16- and 24- hours of AD treated MLE12 cells (Figure 1.7 C). Immunohistochemical analysis of day 7 of AD- and day 28 of Veh- treated mice serial lung sections for cleaved caspase 3, cathepsin D, ATF6 and proSP-C demonstrated localization of increased cleaved caspase 3, cathepsin D and ATF6 to the AECII of day 7 of AD-treated mice versus the day 28 of Veh treated controls (Mahavadi *et al.,* 2014) (Figure 1.7 D - F).

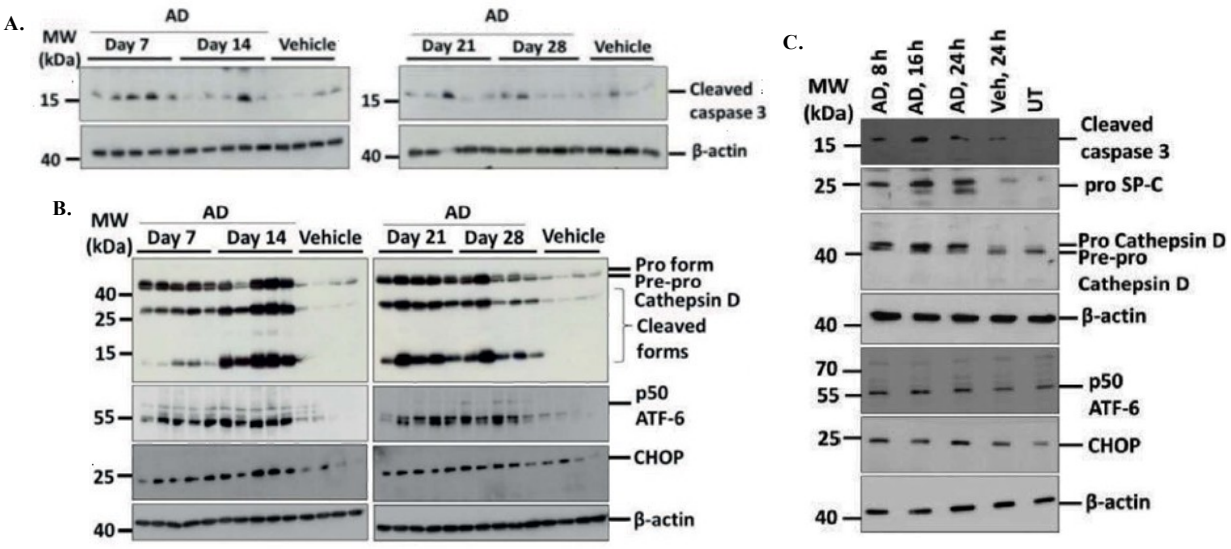

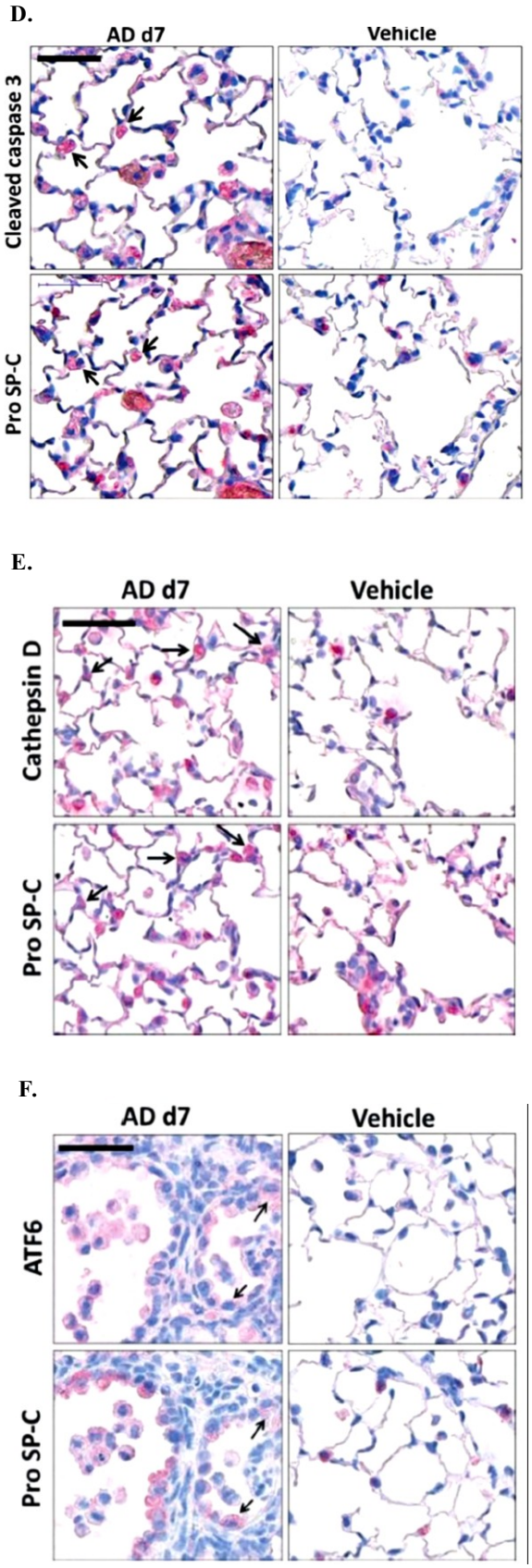

Figure 1.7: Elevated apoptosis, lysosomal and ER stress under AD treatment. (A, B) Western blot images showing increased expression of cleaved caspase 3, cathepsin D, ATF6 and CHOP in the lung homogenates of day 7, 14, 21 and 28 of AD treated mice. (C) Western blot images depicting elevated expression of cleaved caspase 3, proSP-C, cathepsin D, ATF6 and CHOP in 8-, 16- and 24- hours of AD treated MLE12 cell lysates

(D - F) Immunohistochemical analysis of serial lung sections of AD (day 7) treated mice displaying increased expression of cleaved caspase 3, cathepsin D and ATF6 in AECII (proSP-C). (Mahavadi *et al.,* 2014).

1.2. Autophagy

1.2.1. Introduction

In order to maintain cellular homeostasis, an exquisite balance is demanded between anabolism (biosynthesis) and catabolism (degradation) of macromolecules. In eukaryotic cells, there are two main systems involved in degradation namely the ubiquitin proteasomal system (UPS) and the autophagy-lysosomal system (Puissant *et al.,* 2012). UPS involves polyubiquitination of short-lived target proteins *via* a series of enzymatic reactions that are eventually delivered to the 26S proteasomes for degradation. Protein targets with a minimum of four ubiquitin chains interconnected through lysine48 (K48) are are delivered into the proteasome. Large protein complexes and protein aggregates are poor substrates of the UPS system (Korolchuk *et al.,* 2010, Puissant *et al.,* 2012). In contrast, the latter highly conserved catabolic process known as autophagy (Greek for "self eating") encompasses sequestering and degradation of long-lived and bulkier substrates such as macromolecules like proteins (misfolded, oligomers or aggregates), lipids or nucleic acids or damaged organelles *via* lysosomes. Substrates with lysine63 (K63)-linked ubiquitin chains or monoubiquitination are usually targeted to the autophagy-lysosomal system (Korolchuk *et al.,* 2010). Autophagy has been implicated in several different processes *viz* development, differentiation, innate and adaptive immunity, ageing and cell death. It ensures to replenish the cell with nutrient supply during starvation and acts as a quality control mechanism to protect the cell from toxic macromolecules, damaged organelles or invading pathogens. Accumulating evidence demonstrates a pathomechanistic role of autophagy in several human diseases (Johansen and Lamark, 2010, Wirawan *et al.,* 2012).

1.2.2. Types of autophagy

Autophagy has been categorized into three types namely i) Chaperone mediated autophagy (CMA) ii) Microautophagy and iii) Macroautophagy (Wirawan *et al.,* 2012) (Figure 1.8).

CMA is a selective form of autophagy that involves sequestering of proteins with degenerate pentapeptide sequence motif 'KFERQ' that binds to a complex of heat shock cognate 70 (Hsc70) and its co-chaperones, which later associates with lysosomal receptor, lysosomal-associated membrane protein-2A (LAMP2A) and transports the substrate protein into the

lumen of lysosome for degradation (Johansen and Lamark, 2010, Wirawan *et al.,* 2012). Microautophagy refers to the direct invagination of the lysosomal membrane to engulf parts of cytoplasm, which are subsequently degraded once they are completely enclosed (Wirawan *et al.,* 2012).

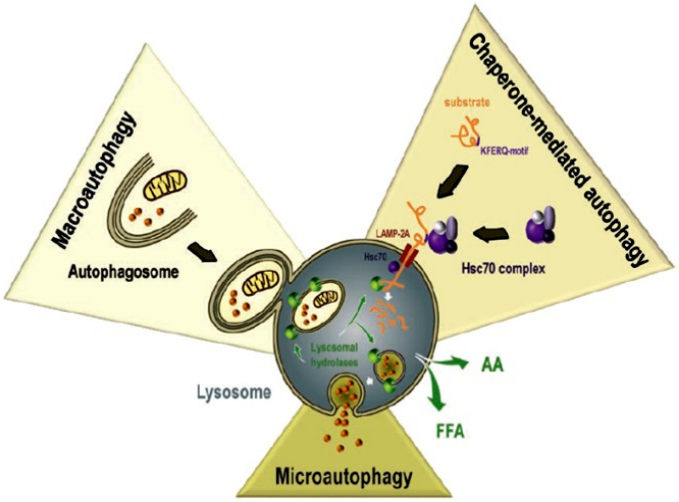

Figure 1.8: Types of autophagy (Wirawan *et al.,* 2012).

Macroautophagy is the most well studied form of autophagy that generally involves non-selective bulk degradation marked by expansion of a crescent shaped double membranous structure called the phaghophore (isolation membrane) into a double-membrane vesicle called the autophagosome, encompassing the cytoplasmic contents to be degraded, eventually fusing with the lysosome to form autolysosome to degrade its contents (Johansen and Lamark, 2010) (Figure 1.9). A total of around 30 AuTophaGy-related genes (Atg) proteins have been identified so far in yeast, many of these have known orthologs (ATG) in higher eukaryotes (Feng *et al.,* 2014) (Figure 1.10). Amidst this, 15 "core" ATG proteins are commonly required for different autophagy pathways (Johansen and Lamark, 2010, Feng *et al.,* 2014).

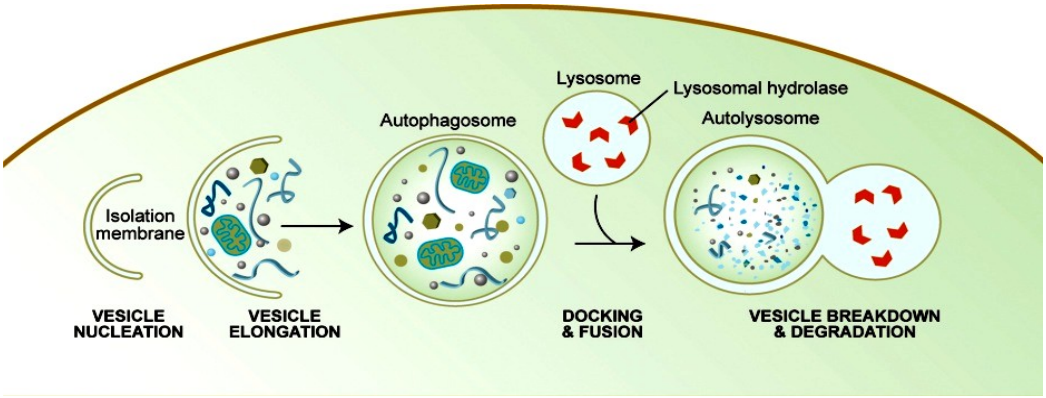

Figure 1.9: General steps in macroautophagy
(http://www.wormbook.org/chapters/www_autophagy/autophagyfig1leg.jpg).

Yeast	Mammals	Characteristics and functions
Atg1	ULK1/2	Ser/Thr protein kinase; phosphorylated by M/TORC1; recruitment of Atg proteins to the PAS
Atg13	ATG13	Regulatory subunit through phosphorylation by M/TORC1 and/or PKA, linker between Atg1 and Atg17
Atg17	RB1CC1/FIP200 (functional homolog)	Scaffold protein, ternary complex with Atg29 and Atg31. Phosphorylated by ULK1; scaffold for ULK1/2 and ATG13
Atg29		Ternary complex with Atg17 and Atg31
Atg31		Ternary complex with Atg17 and Atg29
Atg11		Scaffold protein in selective autophagy for PAS organization
	C12orf44/Atg101	Component of the complex with ATG13 and RB1CC1
Atg2	ATG2	Interacts with Atg18
Atg9	ATG9A/B	Transmembrane protein, directs membrane to the phagophore
Atg18	WIPI1/2	PtdIns3P-binding protein
Vps34	PIK3C3/VPS34	PtdIns 3-kinase
Vps15	PIK3R4/VPS15	Ser/Thr protein kinase
Vps30/Atg6	BECN1	Component of PtdIns3K complex I and II
Atg14	ATG14	Component of PtdIns3K complex I
Atg8	LC3A/B/C, GABARAP, GABARAPL1/2	Ubl, conjugated to PE
Atg7	ATG7	E1-like enzyme
Atg3	ATG3	E2-like enzyme
Atg4	ATG4A/B/C/D	Deconjugating enzyme, cysteine proteinase
Atg12	ATG12	Ubl
Atg7	ATG7	E1-like enzyme
Atg10	ATG10	E2-like enzyme
Atg16	ATG16L1	Interacts with Atg5 and Atg12
Atg5	ATG5	Conjugated by Atg12

Figure 1.10: Orthologous core Atg/ATG protein machineries in yeast and mammals. (Feng *et al.,* 2014).

1.2.3. Regulation of macroautophagy

In mammals, macroautophagy is a multistep process that includes i) initiation, ii) nucleation iii) elongation and iv) maturation/ degradation (Puissant *et al.,* 2012, Wirawan *et al.,* 2012) (Figure 1.9). Diverse input signals such as nutrients, growth factors, hormones, intracellular Ca^{2+} concentration, adenosine triphosphate (ATP) levels, hypoxia, accumulation of misfolded proteins and many other factors determine the induction of macroautophagy (Wirawan *et al.,* 2012). It is a tightly regulated process and many of these signals target membrane target of rapamycin complex 1 (mTORC1) that encompasses mTOR, regulatory associated protein of

mTOR (raptor), proline rich AKT substrate 40 kDa (PRAS40) and G-protein-β-subunit-like protein (GβL) (Puissant *et al.,* 2012, Wirawan *et al.,* 2012).

When mTORC1 is active (as during the nutrient replete state), it inhibits autophagy by phosphorylating uncoordinated-51 (unc-51) - like kinase 1 or 2 (ULK1/2, a homologue of yeast Atg1) and ATG13 (a homologue of yeast Atg13) of the ULK1/2 complex, which is known to activate autophagy initiation (Wirawan *et al.,* 2012, Feng *et al.,* 2014). ULK1 kinase can be activated both by AMP-activated protein kinase (AMPK) dependent (glucose starvation) and independent (amino acid starvation) pathways (Feng *et al.,* 2014). But when phosphorylated, there is a disruption of interaction between ULK1 and AMPK, thus inhibiting autophagy initiation. The ULK1/2 complex also harbors focal adhesion kinase family interacting protein of 200kDa (FIP200, a putative Atg17 homologue) and ATG101 protein. ATG13 acts as connecting bridge between ULK1/2 and FIP200 (Johansen and Lamark, 2010, Feng *et al.,* 2014) (Figure 1.10, 1.11).

When mTORC1 is inactive (during nutrient deprivation or in the presence of rapamycin), the mTORC1 complex dissociates from the ULK1/2 complex, promoting ULK1/2 activity and hyperphosphorylation of ATG13, FIP200 (Wirawan *et al.,* 2012, Feng *et al.,* 2014).The activated ULK1 complex also phosphorylates activating molecule in beclin-1 regulated autophagy (AMBRA1) and BECN1 of another autophagy-inducing complex, the phosphotidylinositiol-3-kinase class 3 (PIK3C3) complex (Wirawan *et al.,* 2012, Feng *et al.,* 2014). PIK3C3 complex is comprised of PIK3C3, AMBRA, Beclin-1, p150 and UV-radiation resistance associated gene (UVRAG) or ATG14L (Wirawan *et al.,* 2012). During nutrient rich conditions, PIK3C3 complex is connected to the cytoskeleton *via* AMBRA. But phosphorylation of AMBRA1 by ULK1 releases the phosphotidylinositiol-3-kinase class 3 (PIK3C3) complex from the microtubules-associated dynein motor complex and facilitates its relocation to the endoplasmic reticulum, which is considered to be a major organelle involved in the formation of autophagosome (Wirawan *et al.,* 2012). Beclin-1 (Atg6) within the PIK3C3 complex provides a platform for binding of other interactors that regulate the kinase activity of PIK3C3 (Wirawan *et al.,* 2012). This results in generation of phosphotidyl-inositol-3-phosphate (PI3P), which further recruits other ATG proteins *viz* WD repeat protein interacting with phosphoinositides 1 and 2 (WIPI1 and WIPI2), mATG2 and double-FYVE containing protein-1 (DFCP-1) to the site of autophagosome formation, facilitating a process referred as autophagosome nucleation (Wirawan *et al.,* 2012) (Figure 1.10, 1.11).

ULK1 also plays a vital role in trafficking the multispanning membrane protein, mATG9 to the site of autophagosome formation during starvation. mATG9 might be supplying lipids for autophagosomes elongation (Wirawan *et al.,* 2012) (Figure 1.10, 1.11).

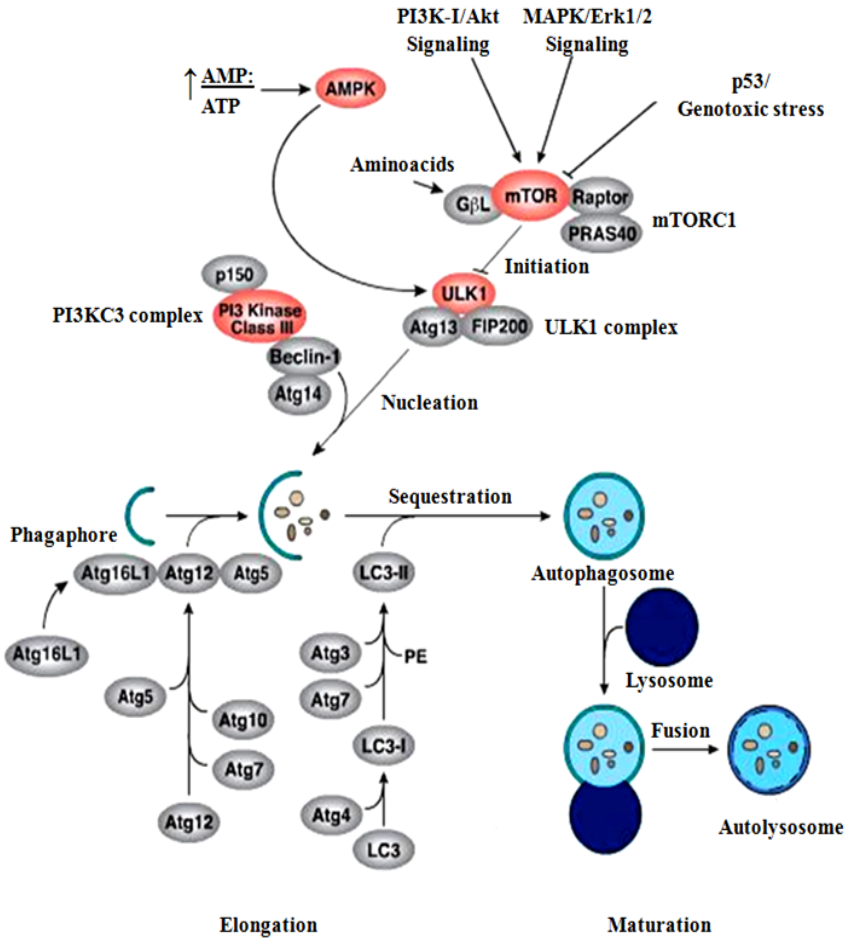

Figure 1.11: Molecular outlook of macroautophagy. (http://www.cellsignal.com).

Two ubiquitin (Ub)-like protein conjugating systems involving two Ub-like modifiers LC3/Atg8 and ATG12 (part of the evolutionarily conserved autophagic machinery) play a pivotal role in the elongation, shaping and sealing of the autophagosome (Wirawan *et al.,* 2012). ATG7 acts as the E1-like enzyme for both the conjugating systems. ATG7 activates ATG12, which subsequently gets conjugated it to ATG5 by the action of E2-like enzyme, ATG10. The ATG12-ATG5 complex further interacts with ATG16L1 to form a trimer, which homodimerizes and transiently associates with the growing outer membrane of the autophagosome and has been suggested to determine its curvature (Johansen and Lamark, 2010, Wirawan *et al.,* 2012).

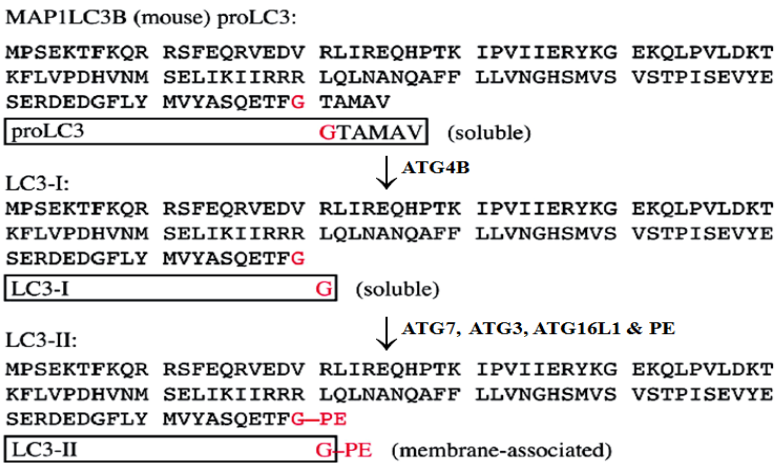

Figure 1.12: Generation of lipidated LC3 (LC3-II) from pro-LC3. (Klionsky *et al.,* 2012).

ATG16L1 complex also acts as an E3-ligase for the second conjugation reaction involving lipidation of MAP1LC3 (microtubule-associated protein 1 light chain-3), a homologue of ATG8. MAP1LC3 is produced as a soluble 'pro' form, where a pentapeptide sequence at the carboxy-terminus is cleaved by the cysteine protease, ATG4B, to generate a soluble MAP1LC3-I form. Through the concerted action of the second ubiquitin-like protein conjugation system (involving ATG7 (E1-like enzyme), ATG3 (E2-like enzyme) and ATG16L1 (E3-ligase) 'soluble' MAP1LC3-I gets converted to 'membrane bound' MAP1LC3-II by the addition of phosphotidylethanolamine (PE) (Wirawan *et al.,* 2012, Feng *et al.,* 2014) (Figure 1.11 and 1.12). MAP1LC3-II particularly localizes to the autophagosomal membrane, hence MAP1LC3-II serves as an autophagy specific marker, particularly an autophagosomal marker *per se*. Upon completion of the vesicle formation, ATG4 cleaves the MAP1LC3-II bound to the outer membrane of the autophagosome by a process of deconjugation. The MAP1LC3-II associated with the inner membrane of the autophagosomes remains intact until it fuses with the lysosomes, where it gets degraded (Johansen and Lamark, 2010, Wirawan *et al.,* 2012, Klionsky *et al.,* 2012). In mammals, there are atleast seven ATG8 homologues identified so far that has been classified into two subfamilies - i) three MAP1LC3 proteins (MAP1LC3A, B and C) and four gamma aminobutyrate receptor associated protein (GABARAP) and GABARAP-like proteins (GABARAPL1, L2 and L3). Although all except GABARAPL3 are demonstrated to be involved in autophagosome synthesis, the LC3B remains to be the most commonly examined ATG8 homologue in the mammalian system (Johansen and Lamark, 2010, Klionsky *et al.,* 2012).

Upon completion of the autophagosome formation, it either fuses with early or late endosomes to form amphisome, which then fuses with the lysosome or directly fuses with the lysosome. The outer membrane of the autophagosome fuses with the lysosomes, thereby releasing the inner autophagosomal membrane and its content into the lysosomal lumen (autophagic body) (Wirawan *et al.,* 2012). Lysosomes are acidic membrane bound organelles enriched with hydrolytic enzymes, which are responsible for degradation of macromolecules delivered to them *via* autophagy, endocytosis or phagocytosis (Eskelinen, 2006). Lysosomal membrane has a crucial role in protecting other cellular constituents from the degradative potential of lysosomal hydrolases, whereas lysosomal membrane proteins are involved in maintaining an acidified lysosomal lumen, transport of free aminoacids, fatty acids, carbohydrates and other nutrients derived from lysosomal digestion into the cytosol (Eskelinen*,* 2006, Wirawan *et al.,* 2012). About 50% of the proteins in the lysosomal membrane are estimated to be Lysosome Associated Membrane protein 1 (LAMP1) and LAMP2. These proteins share about 37% amino acid sequence homology and share common functions *in vivo* (Eskelinen*,* 2006). Mice deficient in both LAMP1 and LAMP2 have been demonstrated to have an embryonic lethal phenotype, whereas mice deficient for either LAMP1 or LAMP2 were reported to be viable and fertile, with LAMP2 single deficiency exhibiting more serious consequences. Increased accumulation of autophagic vacuoles had been described in both LAMP2 single knockout and LAMP1/LAMP2 double knockout mice (Eskelinen, 2006). In addition, LAMP1/LAMP2 double knockout mice embryonic fibroblasts were reported to demonstrate altered lysosomal appearance, perturbed cholesterol metabolism and unaffected protein degradation rate (Eskelinen, 2006).

1.2.4. Selective autophagy

In contrast to macroautophagy, which is primarily considered a non-selective bulk degradation process of long lived proteins and organelles, more selective forms of autophagy are increasingly becoming apparent (Johansen and Lamark, 2010, Wirawan *et al.,* 2012). Aggrephagy is the process of selective autophagic degradation of protein aggregates or misfolded proteins and the mechanism of autophagy responsible for the selective targeting and degradation of organelles *viz* mitochondria, peroxisomes, endoplasmic reticulum, ribosomes and nuclei are referred as mitophagy, pexophagy, reticulophagy, ribophagy and nucleophagy respectively (Johansen and Lamark, 2010, Puissant *et al.,* 2012, Wirawan *et al.,* 2012).

1.3. Mitophagy

1.3.1. Mitochondrial Quality control

There are three major pathways of mitochondrial quality control. First, mitochondria have two AAA protease complexes on their inner mitochondrial membrane with their catalytic sites exposed on both sides of the membrane to degrade unfolded or misfolded membrane proteins. This process is further assisted by the cytosolic proteasomes, which also participate in degrading unfolded and misfolded mitochondrial membrane proteins. The second pathway involves budding of vesicles from mitochondrial tubules. These buds are sequestered with selected mitochondrial cargos (e.g. oxidised mitochondrial proteins) that are eventually targeted to the lysosomes for degradation. While these two pathways are specific for the degradation of a subset of mitochondrial proteins, the third pathway known as 'mitophagy' involves sequestering of the entire damaged or superfluous mitochondria within double-membranous vesicular structures called autophagosomes, which then fuse with the lysosomes for degradation (Ashrafi and Schwarz, 2013) (Figure 1.13).

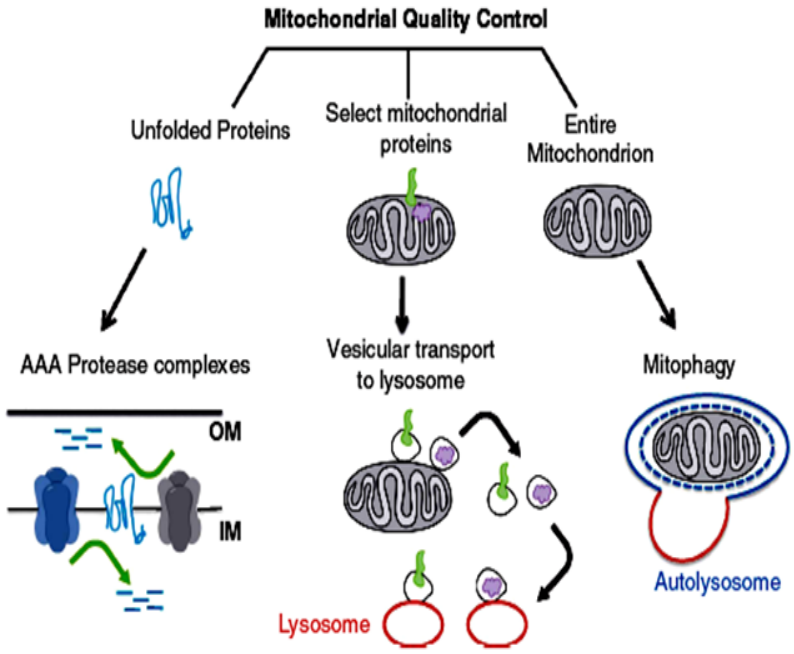

Figure 1.13: Pathways involved in mitochondrial quality control. (Ashrafi and Schwarz, 2013).

In addition to the above stated pathways, it is also imperative for mitochondria to maintain a steady state level of superoxide and hydrogen peroxide production. Under physiological conditions, these molecules act as cell signalling moieties but when the mitochondrial respiratory chain incurs damage, they often turn deleterious by causing serious oxidative

damage to the proteins, lipids and DNA (Bolisetty *et al.,* 2013). Their toxicity is severely enhanced when superoxide and hydrogen peroxide reacts with heme or heme proteins resulting in generation of pro-ferryl forms of heme. Thus, the biosynthesis and degradation of heme is under tight regulation. Heme synthesis is regulated *via* δ-aminolevulinic acid synthase activity and the enzymatic detoxification of heme is carried out by heme oxygenase (HO) isoenzymes (Bolisetty *et al.,* 2013). Heme oxygenases catalyze the conversion of heme into biliverdin IXα, carbon monoxide and Fe^{2+} (Donnelly and Barnes, 2001) (Figure 1.14). There are three different forms of heme oxygenases namely HO-1, HO-2 and HO-3. HO-1 is a major inducible isoform, whereas HO-2 and HO-3 are constitutively expressed isoforms (Lee *et al.,* 2002).

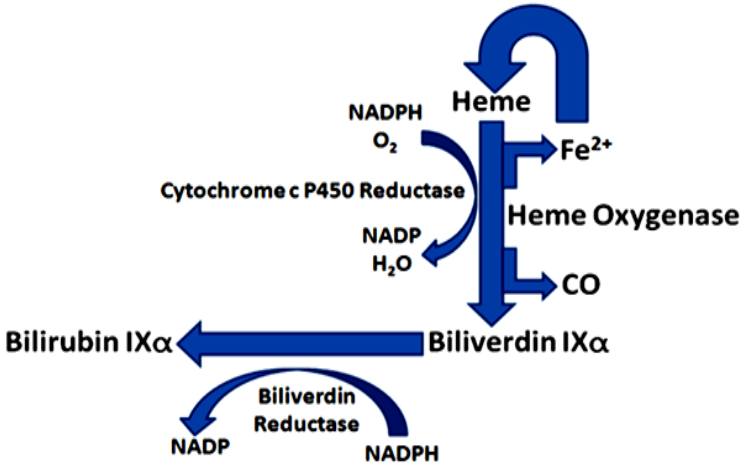

Figure 1.14: HO-1 enzyme activity.

HO-1 is upregulated in response to a variety of stimuli *viz* free heme, oxidative stress, inflammation, heavy metals and UV radiation (Bindu *et al.,* 2011). Apart from being an antioxidative protein, HO-1 also serves as an anti-inflammatory and anti-apoptotic protein (Otterbein, *et al.,* 2003). Increased expression of HO-1 has been reported in neurons resisting oxidative stress induced cell death, cardiovascular diseases, inflammatory diseases, lung injury and other pathological conditions (Bindu *et al.,* 2011). Although mitochondrion is the site for heme synthesis and harbours heme-containing proteins in the electron transport chain, it does not contain HO-1 (Bolisetty *et al.,* 2013). Studies have demonstrated cytoprotective nature of oxidative stress driven translocation of HO-1 to mitochondria and the probable involvement of carbon monoxide in mitochondrial biogenesis, suggesting an intimate link between HO-1 and mitochondrial function (Bolisetty *et al.,* 2013, Slebos *et al.,* 2007). HO-1 has also been shown to regulate autophagy in varied pathological conditions. Interestingly, HO-1 has been implicated to prevent or induce autophagy, under different pathological

conditions. (Yun *et al.,* 2014, Lin *et al.,* 2014, Li *et al.,* 2013, Bolisetty *et al.,* 2010, Kim *et al.,* 2008b).

1.3.2. Mitochondrial fission - a prerequisite for mitophagy

Mitophagy is a catabolic process, in which the core machinery of macroautophagy is harnessed for selective clearance of superfluous mitochondria. Mitochondria are dynamic organelles that undergo continuous fusion and fission within the cell (Ding and Yin, 2012). Each mitochondrion has to be separated from the mitochondrial network to be readily engulfed by the autophagosomes (Ashrafi and Schwarz, 2013) (Figure 1.15 A). *In situ*, mitochondria appear as short round-shaped or elongated organelles with a major axis of ~ 5 µm, whereas autophagosomes are globular organelles with a diameter of ~ 1 µm. In order to avoid sterical hindrance, mitochondrial fission is imperative for the occurrence of mitophagy. Hence, mitochondrial fission always precedes mitophagy (Gomes and Scorrano, 2013). It has also been shown that the fusion event often leads to fission of two subsets of daughter mitochondria with increased or decreased mitochondrial membrane potentials, where the daughter mitochondria with higher membrane potential proceeds to fusion and the depolarized mitochondria are removed by mitophagy. The dynamin-like GTPase, dynamin-related protein (Drp1) and mitochondrial fission 1 (Fis1) protein actively participate in the process of mitochondrial fission (Ashrafi and Schwarz, 2013, Ding and Yin, 2012, Gomes and Scorrano, 2013) (Figure 1.15 B).

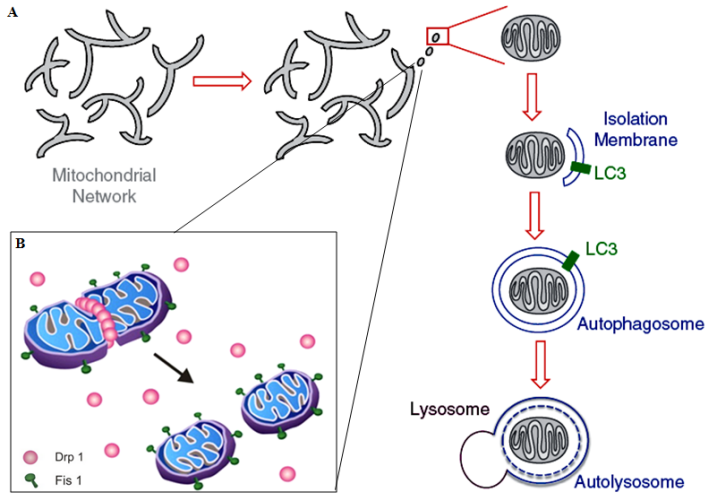

Figure 1.15: Mitochondrial fission and mitophagy. (A) Fragmentation of mitochondria (fission) from the mitochondrial network for ensuing mitophagy. (B) Molecular players *viz* DRP1 and Fis1 involved in mitochondrial fission.
(Ashrafi and Schwarz, 2013 and http://ajpendo.physiology.org/content/ajpendo/303/1/E31/F1.large.jpg).

1.3.3. Mitophagy - Pathways

The fragmented and damaged mitochondria are targeted to the autophagosomes *via* several pathways such as Bcl-2/E1B-19kDa interacting protein 3 (Bnip3), Bnip3-like (Bnip3L) or the PTEN-induced putative kinase 1 (Pink1) - Parkin pathway (Figure 1.16).

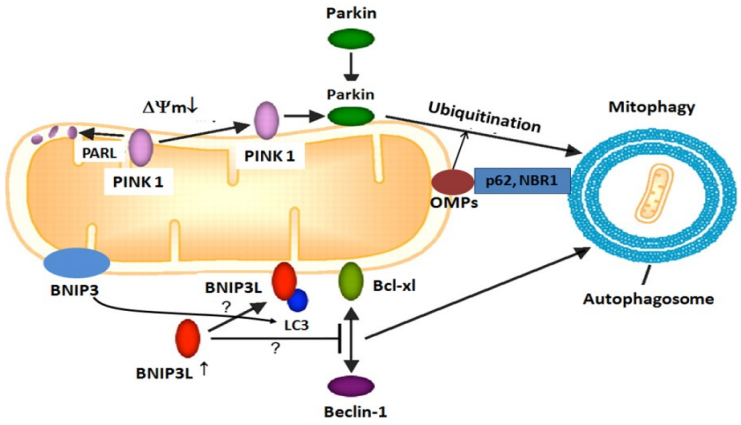

Figure 1.16: Mitophagy pathways. (Adapted from Tait and Green, 2012).

Mitophagy *via* the mitochondrial autophagic receptors: Bnip3 and Bnip3L/NIX are the Bcl-2 homology 3 (BH3) domain containing homologous proteins with 53 - 56 % of aminoacid sequence identity. These proteins get inserted into the outer membrane of the mitochondria through its C-terminal transmembrane domains, while their N-termini remain exposed to the cytosol. The N-terminus of Bnip3 harbours WXXL-like motif, which is important for its direct binding to Atg8 family of proteins *viz* LC3, GABARAP. A similar motif has also been reported in Bnip3L (Ding and Yin, 2012, Hanna *et al.,* 2012) (Figure 1.16 and 1.17).

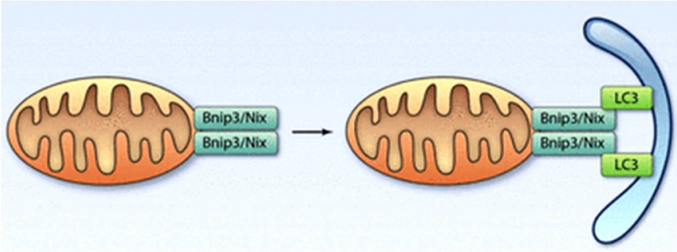

Figure 1.17: Mitophagy *via* Bnip3/Bnip3L. (Kubli and Gustafsson, 2012).

The expression of Bnip3 and Bnip3L are not ubiquitous but are induced under certain conditions. Under hypoxia, the expression of Bnip3 has been demonstrated to be upregulated in a hypoxia-inducible factor-1 (HIF-1) dependent manner, thereby driving mitophagy as an adaptive metabolic response to prevent ROS generation. Bnip3L has been shown to be highly expressed during erythroid differenetiation, where it plays a pivotal role in eliminating mitochondria from mature reticulocytes (Ding and Yin, 2012).

Mitophagy *via* Pink1 - Parkin pathway: Pink1 is a mitochondrial serine/threonine kinase, which is usually quite low in healthy cells due to its rapid cleavage and degradation by Presenilins-associated rhomboid-like protein (PARL) present in the inner mitochondrial membrane. When ΔΨm dissipates, Pink1 gets stabilized on the outer mitochondrial membrane, where it forms a complex with the translocase of the outer membrane and recruits the E3 ubiquitin ligase, Parkin from the cytosol. Following its mitochondrial translocation, Parkin ubiquitinates a subset of outer mitochondrial membrane proteins, which are then recognized by the ubiquitin binding autophagic adaptor proteins like sequestosome-1(SQSTM1)/p62 or neighbor of BRCA1 gene 1 (NBR1) (Ding and Yin, 2012; Johansen and Lamark, 2011). Ubiquitination is the process of tagging a substrate with a single evolutionarily conserved 76 aminoacids protein called ubiquitin or with poly ubiquitins. (Shaid *et al.,* 2013). Thus these cargo adaptor molecules binding ubiquitinated mitochondria, also bind Atg8 family proteins *viz* LC3 or GABARAP through its LC3- interacting region (LIR) by which they facilitate the delivery of the damaged mitochondria to the autophagosomes (Ding and Yin, 2012; Johansen and Lamark, 2011) (Figure 1.18 A and B). Recent report by Fu *et al.,* 2013 also shows Glycoprotein 78 (Gp78) E3 ubiquitin ligase to mediate mitophagy in a Parkin independent manner.

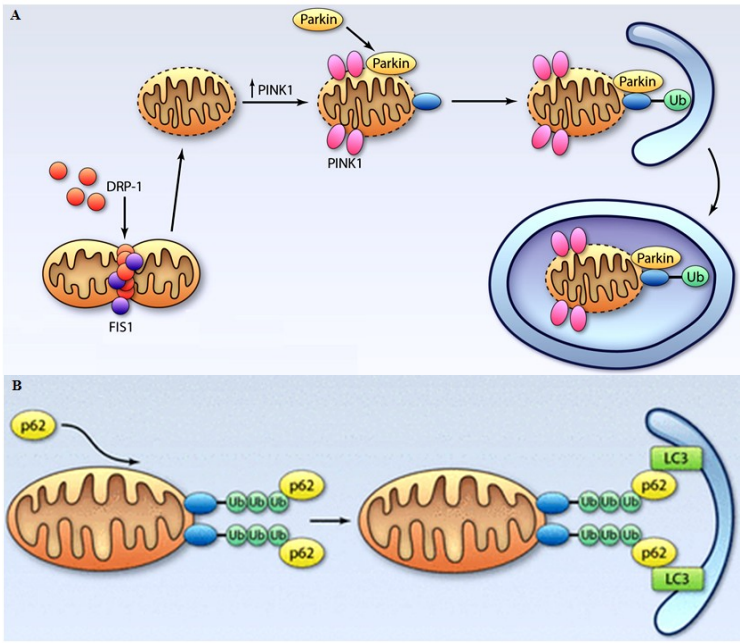

Figure 1.18: Mitophagy *via* Pink1-parkin & p62 pathway. (A) Recruitment of Parkin upon stabilization of Pink1 on the outer mitochondrial membrane, leading to the ubiquitination of outer membrane proteins and targeting to the autophagosomes. (B) p62 mediated targeting of the ubiquitinated mitochondria to the autophagosomes *via* binding to LC3. (Kubli and Gustafsson, 2012).

Domain structure of p62 and NBR1: The human p62 protein is 440 aminoacids long with N-terminal protein-protein interacting Phox and Bem1 (PB1) domain followed by ZZ- type zinc finger domain, LC3-interacting region (LIR), Keap1 interacting region (KIR) and a C-terminal Ub-associated domain (UBA). p62 homopolymerizes *via* the PB1 domain and also interacts with other proteins including NBR1 through this domain. NBR1 protein with 966 aminoacids has a similar domain organization like that of p62 in addition to few other domains like the coiled coil (CC) domain required for dimerization and an evolutionary conserved four tryptophan (FW) domain (Johansen and Lamark, 2011) (Figure 1.19). Both proteins have a UBA domain through which they bind ubiquitinated substrates. Depending on which of the seven lysine (K) residues ubiquitin monomer is linked, the chains are called K6, K11, K27, K29, K33, K48 or K63 ubiquitin chains. Lysine 48 (K48) linked ubiquitin chains are canonical signals for targeting substrates for proteasomal degradation, whereas lysine 63 (K63) linked ubiquitin chains (hereafter referred as ubiquitin.K63) target substrates for degradation *via* autophagy (Shaid *et al.,* 2013).

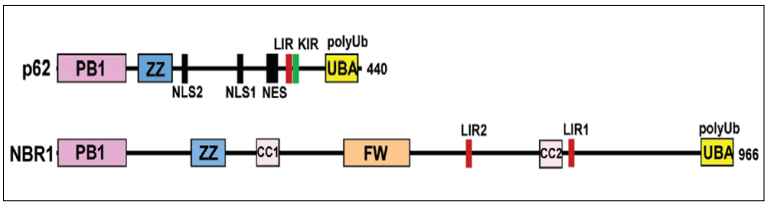

Figure 1.19: Domain structure of p62 and NBR1. (Johansen and Lamark, 2011).

p62 exhibits a very strong binding affinity towards ubiquitin.K63, whereas NBR1 binds both lysine 48 (K48)- and K63-linked diUb. Through their LIR, these proteins bind to the autophagosomes thereby targeting the ubiquitinated substrates to the autophagosomes (Johansen and Lamark, 2011).

1.4 Macroautophagy in murine model of AD-induced pulmonary fibrosis

AD gets accumulated in the acidic milieu of the lysosomes to levels higher than the extracellular concentration (Baritussio *et al.*, 2001, Stadler *et al.,* 2008) due to the low retrograde diffusion of the protonated (AD^+) molecule. This cationic drug uptake is usually mediated by Vacuolar (V)-ATPase, which also results in ensuing vacuolization. The presence of autophagic signal is considered to be a generalized response to the cationic drugs that induce vacuolization (Marceau *et al.,* 2012). AD induces large vacuoles in the cytoplasm of human macrophages (Stadler *et al.,* 2008, Morissette *et al.,* 2009) and evolves towards

persistent macroautophagy (Morissette *et al.,* 2009). Further, AD also causes the increased accumulation of multilamellar bodies (Somani *et al.,* 1987).

Corroborating this, recent publications from our laboratory demonstrate increased number and size of lamellar bodies in AECII (Mahavadi *et al.,* 2014) and AD-induced vacuolization in MLE12 cells, that have been positively labeled for LC3B following AD treatment. In line with this, AD increases the conversion of LC3BI to LC3BII in MLE12 cells, AECII and in mice (Figure 1.20 A, B and C). Immunohistochemical analysis of day 7 of AD- and day 28 of Veh- treated mice serial lung sections for LC3B and proSP-C also revealed localization of increased LC3B to the AECII of day 7 of AD-treated mice against the day 28 of Veh treated controls (Figure 1.20 D). Further, immunogold labelling analysis of the lung tissue of AD and Veh treated mice for LC3B revealed an intense labelling of LC3B on the limiting membrane and interior of the lamellar bodies of AECII under AD treatment (Figure 1.20 E). In addition, a connection between the lamellar bodies and autophagosomes *via* membranes present within the AECII of AD treated mice has also been demonstrated using electron tomography. Supporting this, an efficient fusion of autophagosomes with lysosomes were evident in AD treated MLE12 cells (Figure 1.20 F) (Mahavadi *et al.,* 2015).

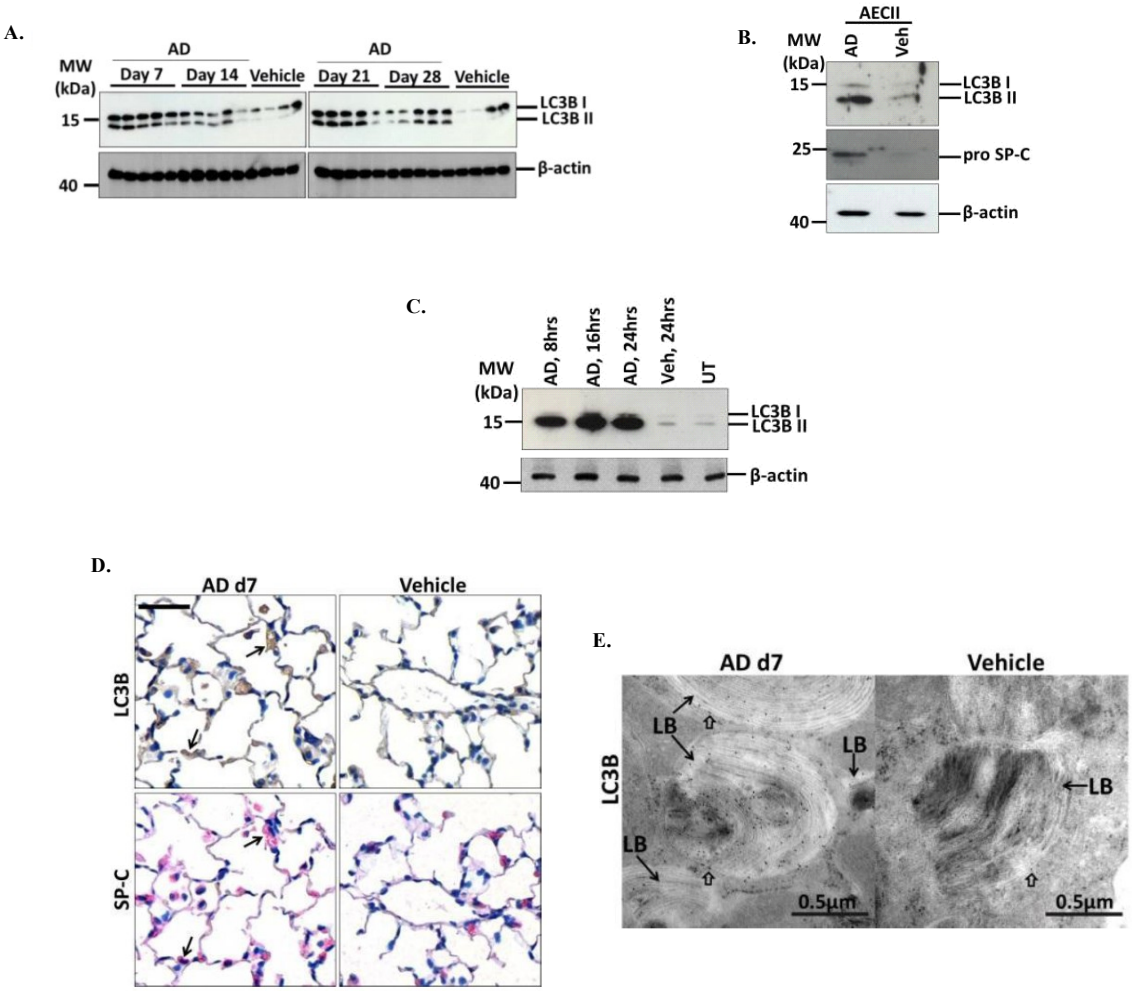

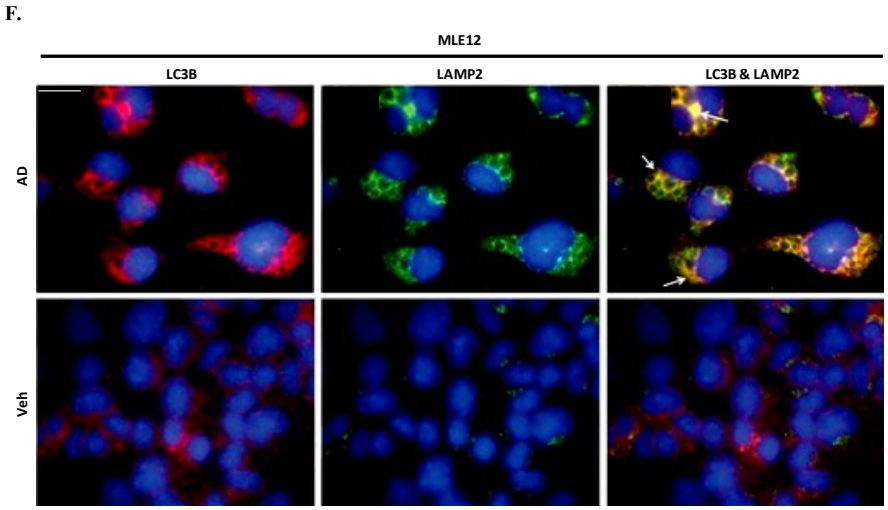

Figure 1.20: AD-induced macroautophagy in MLE12 cells. (A, B, C) Western blot analysis displaying increased LC3B expression in 8-, 16- and 24- hours of AD treated MLE12 cells, 24 hours of AD treated AECII and in day 7, 14, 21 and 28 of AD treated mice lung homogenates respectively. (D) Immunohistochemical analysis of serial lung sections of AD (day 7) treated mice showing increased expression of LC3B in AECII (proSP-C) (E) Immunogold labeling analysis images demonstrating intense LC3B binding to the limiting membrane and interior of the lamellar bodies (LB) in the AECII of AD (day 7) treated mice lung sections. (F) Immunofluorescence analysis of 8 hours of AD treated MLE12 cells showing co-localization (indicated by arrows of LC3B (red) with LAMP2 (green). Nuclei are stained with DAPI (blue). (Mahavadi *et al.,* 2015).

2. Aim of the study

It is well known that AD, a potential anti-arrhythmic drug, causes severe pulmonary toxicity (including pulmonary fibrosis) in patients receiving even low doses. Apoptosis of AECII has been suggested to be a prime factor driving the development of the pulmonary fibrosis. Recent work from our laboratory revealed altered surfactant homeostasis, increased accumulation of lamellar bodies and elevated lysosomal stress in AECII alongside with AECII apoptosis in the murine model of AD-induced pulmonary fibrosis. Further, AD also induced the formation of LC3 positive vacuoles and increased LC3B lipidation (autophagy marker) in AECII, thus raising the possibility of an involvement of macroautophagy in AD-induced pulmonary fibrosis. Dysfunctional mitochondria and enhanced oxidative stress have also been reported in AD-induced pulmonary toxicity. Hence, in the present study, we aimed to investigate the following:

- To decipher the role of macroautophagy in AD-induced AECII apoptosis: is it a pro- or an anti-survival mechanism?
- To determine autophagy flux under AD treatment.
- To investigate if AD promotes mitochondrial autophagy (mitophagy) in the murine model of AD-induced pulmonary fibrosis.
- To find out the possible pathway(s) by which the damaged mitochondria are targeted to the autophagic machinery for degradation in AD treated AECII.
- To discern the probable role of mitophagy and oxidative stress in AECII upon AD treatment.
- To assess the antioxidative response and its role in AD treated AECII.

3. Materials and Methods

3.1. Materials

3.1.1. Equipment

Name	Company
Cell Culture Hood HERAsafe	Hereaus, Germany
Cell Culture Incubator, Hera Cell, 150i	Thermo Scientific, Germany
Centrifuge, Universal 30RF	Hettich, Germany
Centrifuge, Mikro 200R	Hettich, Germany
Dounce homogenizer	B.Braun, Germany
Dry block thermostat	Ditabis, Germany
Dynal MPC-L (Magnetic Particle concentrator)	Dynal, Norway
EMXmicro ESR Spectrometer	Bruker, Germany
Fluoroscence microscopy	Leica, Germany
Freezer +4°C	Bosch, Germany
Freezer -20 °C	Bosch, Germany
Freezer -80°C	Bosch, Germany
Gel imager	INTAS, Germany
Light microscope	Leica, Germany
Magnetic Stirrer	Heidolph, Germany
NanoZoomer Digital Pathology (NDP) version 2.5.85	Hamamatsu Photonics, Germany
Precellys homogenizer	Peqlab, Germany
Spin down	VWR, Germany
Trans-Blot SD Semi-Dry Transfer Cell	Bio-Rad, Germany
Vortex machine	VWR, Germany
Water Bath	Julabo, Germany

Others	
Cell culture plate - 6 well	Greiner Bio-one, Austria
Cell Scraper	Sarstedt, Germany
Cell strainer 70 µM, 40 µM and 10 µM Nylon	BD falcons
Chamber slide - 8 Well	BD falcon, Germany
Falcon - 15 ml	Greiner Bio-one, Austria
Falcon - 50 ml	Corning, USA
Filter 0.22 µm - syringe-driven	Sarstedt, Germany
Filter tips: 10 µl, 100 µl and 1000 µl	Eppendorf, Germany
Gel blotting paper	GE Healthcare, UK
Glass bottles: 250, 500, 1000 ml	Roth, Germany
Glass Slides, Automat Star	Langenbrinck, Germany
Glass slides, SuperFrost Plus	Langenbrinck, Germany
Immobilon - PVDF transfer membrane	Millipore, Germany
Mini-PROTEAN® Tetra Handcast Systems (SDS-Electrophoresis chamber)	Bio-Rad, Germany
Pipette	Eppendorf, Germany
Pipette boy	Eppendorf, Germany
Pipette tips	Biozym, Germany
Steritop filter unit 150 ml, 45 mm	Millipore, USA
Syringe 20G	BD microlance, Germany
Syringes	Braun, Germany
Tissue Culture Dish, 100 x 20 mm	Sarstedt, Germany
Whatmann gel blotting paper	GE Healthcare, Germany
Softwares	
Image J 1.49a software	National Institute of Health, USA

Leica Application Suite Advanced Fluorescence (LAS AF) software, version 4.3	Leica, Germany
NDP.view2 software	Hamamatsu Photonics, Germany

3.1.2. Reagents

Name	**Company**
2-Mercaptoethanol	Sigma-Aldrich, Germany
Acrylamide solution, Rotiphorese gel 30	Carl Roth, Germany
Amiodarone	Sigma-Aldrich, Germany
Ammonium Chloride	Sigma-Aldrich, Germany
Ammonium persulphate	Sigma-Aldrich, Germany
Ammonium sulphate	Merck, Germany
AP-fast red kit	Zytomed, Germany
Bafilomycin A1	Invivogen, USA
BEGM singlequots	Lonza, Germany
Beta-mercaptoethanol	Sigma-Aldrich, Germany
Bicinchoninic acid (BCA) protein assay	Life technologies, Germany
Bovine serum albumin (BSA)	Sigma-Aldrich, Germany
Bromophenol blue	Merck, Germany
Bronchial Epithelial Cell Growth Medium (BEGM)	Lonza, Germany
CathepsinD siRNA (mouse)	Santa Cruz, Biotechnology, Germany
Chloroquine	Sigma-Aldrich, Germany
CMH	Noxygen, Germany
DAB-kit	Zytomed, Germany
dharmaFECT	Thermoscientific, Germany

Dispase	Corning, USA
DMEM-F12	Life technologies, Germany
DMSO	Carl Roth, Germany
DNAse	Fermentas, Germany
Dulbecco's PBS	GE Healthcare, Austria
Dyna beads M-280 Tosyl activated	Life technologies, Germany
Dynabeads Biotin Binder	Life technologies, Germany
EDTA	SERVA, Germany
Ethanol absolut	Fluka, Germany
Fetal calf serum (FCS)	Roth, Germany
Foetal Bovine Serum	Sigma-Aldrich, Germany
Glycerol	Sigma-Aldrich, Germany
Glycine	Carl Roth, Germany
HCL 32%	Carl Roth, Germany
Heme oxygenase 1 siRNA (mouse)	Santa Cruz, Biotechnology, Germany
HEPES	Carl Roth, Germany
Hydrobeta estradiol (ß-estradiol)	Sigma Aldrich, Germany
Hydroxycortisone	Lonza Walkersville, USA
Immobilon western Chemiluminescent HRP substrate	Millipore, Germany
Isoflurane	Baxter, Germany
ITS (100X)	PAN biotech, Germany
Keratinocyte growth factor	Peprotech, Germany
LC3B siRNA (mouse)	Santa Cruz, Biotechnology, Germany
L-Glutamine	Gibco, Germany

Matrigel Basement membrane matrix	BD biosciences, USA
Mdivi-1	Sigma-Aldrich, Germany
Methanol	Carl Roth, Germany
Na_2EDTA	Sigma-Aldrich, Germany
N-acetyl-L-Cysteine (NAC)	Sigma-Aldrich, Germany
Non-targetting siRNA	GE Healthcare, Germany
Pageruler protein ladder	Thermoscientific, Germany
Paraformaldehyde	Carl Roth, Germany
Pen-strep	Life technologies, Germany
Phenylmethylsulfonyl fluoride (PMSF)	Sigma-Aldrich, Germany
Potassium bicarbonate	Sigma-Aldrich, Germany
pSOD	Sigma-Aldrich, Germany
Rotiphorese	Carl Roth, Germany
Saccharose/ Sucrose	Carl Roth, Germany
Skim Milk powder	Sigma-Aldrich, Germany
SnPP	Frontier scientific, USA
Sodium azide	Merck, Germany
Sodium Chloride	Sigma-Aldrich, Germany
Sodium deoxycholate	Merck, Germany
Sodium dodecyl sulphate	Merck, Germany
TEMED	Sigma-Aldrich, Germany
Tris	Carl Roth, Germany
Triton-X100	Sigma-Aldrich, Germany
Trypsin	PAA, Austria
Turbofect	Thermoscientific, Germany
VECTASHIELD mounting medium with DAPI	Vector laboratories, USA

3.1.2.1. Preparation of solutions

AD and Veh stock solution

About 5 mg (0.005 g) of AD was weighed and dissolved in 5 ml of filtered cell culture grade distilled water in a sterile falcon. The falcon was then warmed at 65^{o}C for 10 minutes in an incubator until AD was completely dissolved. The volume was made upto 50 ml with sterile complete DMEM/F12 medium. Similar procedure was followed for preparing Veh solution.

Autophagy inhibitors

Bafilomycin A1 was prepared by dissolving in filter sterilized dimethylsulfoxide (DMSO) and a working concentration of 100 nM was used for experiments. Chloroquine was dissolved in cell culture grade aqua dest and a working concentration of 10 or 30 µg/ml was used.

Others

Mdivi-1 and tin protoporphyrin (SnPP) were dissolved in filter sterilized DMSO and a working concentrations of 20 µM and 25 µM was used respectively. N-acetyl-L-Cysteine (NAC) was dissolved in filtered cell culture grade distilled water and a working concentration of 2mM was used.

3.2. Methods

3.2.1. Mammalian cell culture

3.2.1.1. Culturing of MLE12 cells

MLE12 cells obtained from ATCC, Manassas, USA were grown in 10 cm^2 tissue culture plates in Dulbecco's modified eagle medium, (DMEM)/F12 (supplemented with the following components) at 37°C in 95% air, 5% CO_2.

Components	Concentration/Volume
Hydrocortisone (100 µM)	10 nM
Hydrobetaestradiol (100 µM)	10 nM
ITS -	5%
Insulin	0.005 mg/ml
Transferrin	0.01 mg/ml
Selenite	30 nM
HEPES	10 mM
L-Glutamine	5 ml
Foetal Calf Serum (FCS)	2%
Penstrep	1%

After the cells reach 80-90 % confluency, the cells were passaged. For passaging, cells were washed twice with 1X PBS and incubated with 3 ml of trypsin at 37°C for 2-3 minutes, after which the cells were dispensed from tissue culture plate and suspended into 10 ml of complete DMEM/F12 medium to nullify the activity of trypsin. The cell suspension was centrifuged at 5000xg for 5 minutes. The supernatant was removed and cells were diluted in complete DMEM/F12 medium and plated (1:10) to a new culture dish.

3.2.1.2. Small interfering RNA (siRNA) transfection

For siRNA transfection, 2.5 $x10^5$ MLE12 cells were plated in each well of a 6 well plate and incubated overnight at 37°C and 5% CO_2. Once the cells reached 70 - 80% confluency the next day, the transfection procedure was followed according to the manufacturer's protocol for 48 hours with cathepsin D siRNA (CatDsi) or LC3B siRNA or Heme oxygenase-1 (HO-1) siRNA obtained from Santa Cruz Biotechnology, Germany or with siRNA for non-targeting sequence from Fischer scientific, Germany using dharmaFect. In brief, 20 µM stock

siRNA solution was prepared by resuspending siRNA in 165 µl of RNAse free water, from which 2 µM working siRNA solution was freshly made for each transfection. Then the siRNA and dharmaFect were separately suspended in serum and antibody free medium and incubated at room temperature (RT) for 5 minutes. After which, they both were gently mixed and incubated together for 20 minutes. This was resuspended in serum containing medium, which were added dropwise to MLE12 cells and incubated for 48 hours. The following day, solutions were removed from MLE12 cells and replaced with complete DMEM/F12 medium and treated with AD (10 µg/ml) or Veh for 8 hours.

3.2.1.3. Recombinant plasmid transfection

$3x10^4$ MLE12 cells/well were plated in an eight well chamber slide and incubated for 24 hours at 37°C and 5% CO_2 for adherence. 0.5 µg of endotoxin free recombinant plasmid, green fluorescent protein (GFP) tagged LC3B was dispensed in 50 µl of serum free MLE12 cell culture medium, to which 2 µl of TurboFect was added and mixed gently and incubated at RT for 20 minutes. Meanwhile, the cells were washed twice with 1X PBS and replaced with fresh complete MLE12 culture medium. To this, the incubated mixture was added drop wise and incubated overnight at 37°C and 5% CO_2. The following day, AD (10 µg/ml) and Veh treatment was carried out for 8 hours, after which immunofluorescence protocol was performed as described in 3.3.4.

3.2.1.4. Isolation of murine AECII

AECII were isolated from the lungs of C57BL/6 mice (with prior authorization obtained for animal work from Regierungspräsidium Giessen, GI 20/10-Nr.A53/2012). Intraperitoneal injection of a mixture of rompon, ketamine and heparin (in the ratio 2:2:1) was used to anesthetize the mice. To exsanguinate the animal, the abdominal cavity was opened and the renal artery was severed. Following this, the lungs were perfused with 10 ml of saline to clear off the blood and then filled with dispase until the small lobe is inflated. 0.5 ml of 1% low-melting agarose in DMEM medium was then injected into lung through the trachea and left for 5 minutes to let the agarose solidify. The lungs were then isolated and incubated in 5 ml of warm dispase for 45 minutes at 37°C. Following incubation, lungs were finely chopped in 7 - 8 ml of medium II under the hood and incubated at RT for 10 minutes with gentle shaking. A homogenized cell suspension was subsequently prepared from this incubated lung samples by gently flushing it through a 10 ml pipette. The resulting suspension was filtered

through 70 µm, 40 µm and 10 µm nitex filters and the filtrate was then centrifuged at 950 rpm at 4°C for 10 minutes.

Medium I	
Components	**Concentration/Volume**
DMEM	500 ml
HEPES	1.25 M
1% Penstrep	1%

Medium II	
Components	**Concentration/Volume**
Medium I	50 ml
DNAse	0.04mg/ml

Medium III	
Components	**Concentration/Volume**
Medium I	50 ml
FCS	10%

Erythrocyte (ER) - lysis buffer (pH 7.4)	
Components	**Concentration/Volume**
dH_20	1000 ml
NH_4Cl	8,29g
$KHCO_3$	1g
Na_2EDTA	0.037 g

The pellet obtained was resuspended in 5 ml of lysis buffer and incubated at RT for 8 minutes on a shaker. The suspension was again filtered through 70 µm nitex filter and equal volume of 1X PBS was added and re-centrifuged at 950 rpm at 4°C for 10 minutes. The resulting pellet was then suspended in 1 ml of medium III. The cell number was then counted using haemocytometer and the total number of cells in the suspension was calculated using the following formula -

Total number of cells = Average number of cells in four quadrants x 4 x 2.5 x total volume of cell suspension (in µl).

1 ml of medium III was then added for every 10 million cells. Following this, 0.9 µl of CD 45, 0.675 µl of CD16/32 and 0.4 µl of CD 31 antibodies / million cells were added and

incubated at 37°C for 30 minutes in a water bath with intermittent shaking. Meanwhile, the biotinylated beads were prepared in 15 ml falcon tubes according to the following calculation-

A = (X million cells x 0.45) + (X million cells x 0.2)
B = A/3 (ml medium), C = B x 50 (µl beads)

The 'C' volume of beads was taken and washed thrice with 1ml of 1X PBS using a magnetic seperator and resuspended in volume 'C' of 1X PBS. Following incubation, equal volume of medium I was added to the cell suspension and centrifuged at 950 rpm at 4°C for 10 minutes. The resulting pellet was suspended in medium I in volume equal to 'B'. The suspension was then added to the beads with no more than 10 ml per 15 ml falcon and left on the shaker for 20 minutes at RT. Falcons were then left undisturbed on a magnetic seperator for 15 minutes. The cell suspension was carefully collected and centrifuged at 950 rpm at 4°C for 10 minutes. Cell pellet was resuspended in Medium I and purity of the cells was analyzed for proSP-C staining.

3.2.1.5. Culturing of murine AECII

For culturing murine AECII on a 6 well plate, each well of the plate was coated with 500 µl of Matrigel, a basement membrane matrix. After coating all the wells, the plate was incubated at 37°C for 1 hour without CO_2. The matrigel was then equilibrated with sterile AECII culture medium with the following components -

Components	Concentration/Volume
BEGM	500 ml
FBS	5%
BPE	2ml
Insulin	5 mg/ml
Gentamycin	5ml
Retinoic acid	0.1 µg/ml
Transferrin	10 mg/ml
Triiodothyronine	0. 5 ml
Epinephrine	0.5 mg/ml
hEGF	0.5 µg/ml
KGF (Freshly added)	1 µl/ml

The coated plate with the sterile AECII culture medium was incubated at 37°C for 45 minutes to 1 hour with CO_2. Each coated well was seeded with half million to 1 million cells and allowed to adhere overnight at 37°C and 5% CO_2. The following day, adhered AECII were treated with AD (10 µg/ml) or Veh for 24 hours. To harvest the AECII from the matrigel, about 1 ml of dispase was added and left at 37°C for 15 - 20 minutes. The dissolved matrigel along with the cells were collected in a falcon and washed twice or thrice with 1X PBS and centrifuged at 5000 rpm at 4°C for 5 minutes and the resultant pellet was shock frozen in liquid nitrogen and stored at -80°C until the cell lysates were prepared.

3.2.1.6. Preparation of cell lysates and protein quantification

The AD or Veh treated MLE12 cells and AECII were lysed using the lysis buffer, to which phenylmethylsulfonyl fluoride (PMSF) was added in the ratio of 100:1.

Lysis buffer	
Components	**Concentration/Volume**
Tris	50 mM
NaCl	50 mM
EDTA	5 mM
Triton X-100	1%
Sodium deoxycholate	0.5%

The lysates were shock frozen using liquid nitrogen and incubated on ice for 15 to 20 minutes and this step was repeated for three times with the final incubation on ice for 1 hours. The lysates were then centrifuged at 12,000 rpm for 10 minutes at 4°C. The supernatants were collected and protein concentrations were analyzed using bicinchoninic acid (BCA) - protein assay kit (Life technologies, Germany) according to the manufacturer's instructions using standard decreasing concentrations of bovine serum albumin (BSA). Samples for western blotting were then prepared from these supernatants and the remaining samples were stored at -80°C until further use.

3.2.2. Sample preparation for western blot

The samples for the western blot analysis were prepared by reducing the protein samples obtained from tissues or cells using 10% β-mercaptoethanol containing 4X loading buffer and

boiling it for 10 minutes at 98°C and incubating on ice for 5 minutes. Samples were then briefly centrifuged and loaded onto Sodium dodecyl sulphate (SDS) containing polyacrylamide gel and electrophoresis were performed at 40 milliamperes (mA) per gel using 1X electrophoresis buffer.

4X Loading buffer	
Components	**Concentration/Volume**
SDS	5 g
0.625M Tris-Hcl pH6.8	25 ml
Glycerol	40 ml
Bromophenol blue	0.0005 g
d.H_2O	100 ml

1X Electrophoresis buffer	
Components	**Concentration/Volume**
SDS	10 g
Tris	30 g
Glycine	144 g
d.H_2O	1000 ml

3.2.2.1. SDS polyacrylamide gel

The stacking and resolving gel were prepared as per the below tabulated formulation.

Separating gel (10 ml)			
Components	**8%**	**10%**	**15%**
d. H_2O	3.87 ml	3.2 ml	1.53 ml
1.125M Tris, pH8.8	3.33 ml	3.33 ml	3.33 ml
Acrylamide/Bisacrylamide (30%/8%)	2.66 ml	3.33 ml	5.0 mll
10% SDS	100 µl	100 µl	100 µl
TEMED	10 µl	10 µl	10 µl
10% APS	50 µl	50 µl	50 µl

Stacking gel (10 ml)	
Components	**Concentration/Volume**
d. H_2O	6.57 ml
0.625M Tris, pH6.8	2 ml
Acrylamide/Bisacrylamide (30%/8%)	1.33 ml
10% SDS	100 µl
TEMED	10 µl
10% APS	100 µl

3.2.2.2. Western blotting

The SDS-polyacrylamide gel separated proteins were then transferred onto the methanol activated PVDF membrane (Amersham) using the semi-dry technique in transfer buffer for 1 hour 30 minutes at 70 mA per gel.

Transfer buffer	
Components	**Concentration/Volume**
Tris	4.85 g
Glycine	22.51 g
Methanol	400 ml
d. H_2O	Make up to 2000 ml

After the transfer, the PVDF membrane was blocked using 5% non-fat dry milk in TBST for 1.5 hours at RT.

10X TBST(pH 7.6) buffer	
Components	**Concentration/Volume**
Tris	48.6 g
NaCl	116 g
Tween 20	20 ml
d. H_2O	2000 ml

After blocking, the membrane was incubated in a solution of the respective primary antibody dissolved in blocking buffer as listed in the appendix for overnight at 4°C. The following day,

the membrane was washed three times with 1X TBST buffer for 10 minutes each time. The membrane was then incubated with the respective HRP-conjugated secondary antibody for 1 hour at RT. The membrane was again washed three times with 1X TBST buffer for 10 minutes each time. Then bands on the membrane were visualized using immobilon western chemiluminescent HRP substrate as per manufacturer's instructions for detecting the protein expression.

3.2.3. Immunohistochemistry

Immunohistochemistry was performed on the slides containing the paraffin-embedded, formalin-fixed lung sections from AD (day 7, 14, 21 and 28) and Veh (Day 28) treated mice. To deparaffinise, the slides were first warmed at 60°C for 1 to 2 hours and then placed in xylol for 10 minutes. Following this, to dehydrate, the slides was placed in descending ethanol concentration gradient (99.6%>96% >80%>70%>50%) for 3 minutes each. The slides were then washed with 1X fresh PBS for few minutes. Antigen retrieval was performed by boiling the slides at 100°C for 20 minutes in citrate buffer (pH6.0), after which the slides were allowed to return to room temperature. This step was repeated for two more times. Then the slides were washed three times with 1X PBS for 5 minutes and blocked by incubating it with the blocking solution (from AP-fast red or DAB Kit) in a wet chamber for 5 - 10 minutes. The primary antibody prepared in 3% BSA were then added to the lung sections and incubated in the wet chamber either at RT for 1 hour or at -4°C for overnight. Following this, slides were washed four times with 1X PBS for 5 minutes and incubated with biotinylated secondary antibody in a wet chamber at RT for 10 minutes. After washing with 1X PBS for three times, the lung sections was incubated with enzyme conjugate. After observing the colour development, slides were washed following nuclear staining with hämalaun for 45 seconds to a minute. Following this, slides were mounted using glycerol mounting medium. After drying, the sections were scanned in digital slide scanner using NanoZoomer Digital Pathology (NDP) version 2.5.85 and were analyzed using NDP.view2 software.

3.2.4. Immunofluorescence

$3x10^4$ MLE12 cells were plated in each well of a 8 well chamber slides and left overnight for adhering at 37°C with 5% CO_2. The following day, the adhered MLE12 cells were treated with AD (10µg/ml) or Veh containing medium for 8 hours. The cells were then washed with 1X PBS and fixed using 4% Paraformaldehyde for 30 minutes. After washing with 1X PBS,

permeabilization was performed with 0.5% Triton X-100. Permeabilized cells were then washed and blocked with 3%BSA in PBS for 1 hour at RT. Following this, the cells were incubated with primary antibody overnight at 4°C. The next day, the cells were washed and treated with fluorophore conjugated secondary antibody for 1 hour at RT in dark. The cells were finally washed with 1X PBS and mounted using VECTASHIELD mounting medium with DAPI. The immunofluorescence slides were then analyzed using Leica Application Suite Advanced Fluorescence (LAS AF) software, version 4.3, Germany. Similar procedure was followed for co-immunofluorescence analysis employing a GFP-transfected plasmid, with the transfection being performed 24 hours prior to commencement of the immunofluorescence procedure. For immunofluorescence analysis of AECII, same protocol was followed except that 24 hours of AD (10 µg/ml) or Veh treatment was carried out.

3.2.5. Immunoprecipitation

2 mg of Dyna beads M-280 Tosyl activated per tissue culture dish (10 cm) was taken and washed twice with 1 ml of PBS (1X) by placing on the magnetic stand. After washing, the beads were resuspended in 58 µl of PBS and 1 µg of antibody (LC3B (ab48394) or p62 (P0067) or rabbit immunoglobulin G (IgG) (AB-105-C)/ mg of beads were added.

Buffer A	
Components	**Concentration/Volume**
Ammonium sulphate	3 M
PBS	-

To this, buffer A equal to (2/3 volume of PBS + Antibody) was added and incubated overnight at RT. The next day, eight hours of AD (10 µg/ml) or vehicle treated MLE12 cells were lysed using 400 µl of non-denaturing co-IP lysis buffer. The lysates were kept on ice for 1 hour and centrifuged at 15000 rpm for 15 minutes and the supernatant was saved. Total amount of protein present in the supernatant of respective lysates were determined using BCA - protein assay. Meanwhile, the beads obtained from the overnight incubation were thrice washed thoroughly with 1 ml of PBS (1X). Equal concentration of proteins were then added to IgG or Antibody of interest (LC3B or p62) coupled beads (while storing about 20 µl of supernatant as input samples) and incubated at 4°C overnight. The following day, the sample tubes were placed on the magnetic stand and allowed to stand for five minutes and the supernatant was removed. The beads were then washed three times with PBS and resuspended in 20 µl of PBS

and transferred to a fresh eppendorf tube. Protein loading buffer was added to the beads and boiled at 96°C for 10 minutes and the samples were then analyzed using western blotting.

Co-IP lysis buffer	
Components	**Concentration/Volume**
Tris	50mM
NaCl	300 mM
EDTA	5 mM
TritonX-100	1%
Sodium azide	0.02%
PMSF	1%

3.2.6. Mitochondrial-lysosomal fractionation

The protocol for isolating mitochondrial-lysosomal fraction was adapted from Muquit *et al.,* 2006. AD (10 µg/ml) or Veh treated MLE12 cells were trypsinized and washed thrice with PBS and the resulting pellet was shock frozen in liquid nitrogen and used for isolating mitochondrial-lysosomal fraction. All the subsequent steps were performed at 4°C. MLE12 cells were resuspended in 300 µl of buffer I.

Buffer I	
Components	**Concentration/Volume**
Sucrose	250 mM
HEPES	20 mM
EDTA	3 mM
PMSF	1%

The cells were then disrupted using a dounce homogenizer (20 passes), followed by 15 passes with a 20G syringe. The cells were spun down at 830g for 10 minutes and the supernatant S1 was retained, whereas the pellet was again resuspended in 300 µl of buffer I and dounce homogenized again (20 passes) and the cells were spun down at 830g for 10 minutes. The supernatant S2 was retained and combined with S1 supernatant and spun down at 16,800g for 10 minutes. The supernatant (cytoplasmic fraction) was retained and the pellet was resuspended in 500 µl of buffer I and spun at 16,800g for 10 minutes. This step was repeated three times and all the supernatant were then carefully removed and the pellet (mitochondrial-lysosomal fraction) was resuspended in 50 - 100 µl of buffer I. The protein concentrations for

all the fractions were then determined using BCA protein assay and the samples were analyzed using western blotting.

3.2.7. Electron spin resonance (ESR)

For measuring ROS production, duplicate samples of AD (10 µg/ml) or Veh treated MLE12 cells (10^6) of five independent treatments were taken and incubated with 1-hydroxy-3-methoxycarbonyl-2,2,5,5tetramethylpyrrolidine (CMH) (500 µM) spin probe for 30 minutes at 37°C or with superoxide dismutase conjugated to polyethylene glycol (pSOD) (15 U/ml) for 90 minutes at 37°C, followed by addition of CMH spin probe and additional incubation for 30 minutes at 37°C. The samples were then shock frozen and stored in liquid nitrogen. ESR measurements for the frozen samples were performed using EMXmicro ESR Spectrometer with a g-factor of 2.0063, centre field of 3366.8 G, microwave power of 2.000 mW, sweep time of 10 seconds and sweep number of 6. (n = duplicate set of 5 independent treatments).

3.2.8. Statistical analysis

All data are represented as mean ± standard error mean (SEM). The statistical significance was calculated by using Mann-Whitney U test in Graphpad Prism 5 software. Significance is indicated *$p < 0.5$, **$p < 0.01$, ***$p < 0.001$.

3.3. Animal tissues

3.3.1. Preparation of lung homogenates

With regard to *in vivo* studies, lung tissue homogenates were used, which had been obtained during previously conducted animal experiments (Regierungspräsidium Giessen; GI 20/10 Nr. 109/2011). In these experiments, mice were transbronchially treated with AD (0.8 mg/kg bodyweight) or Veh and lungs were harvested after 7, 14, 21, and 28 days (AD) or 28 days (Veh). A small piece of mice lungs (about 50 mg) of AD (Day 7, 14, 21 and 28) and Veh (Day 28) was taken in micro packaging vials containing 1.4 mm and 2.8 mm zirconium oxide beads and protein extraction buffer with protease inhibitor. Tissues were then homogenized at high speed in Precellys (2 cycles of 20 sec at the speed of 5500 rpm) according to manufacturer's instructions. Samples were then centrifuged for 10 min at 13000 rpm at 4°C to pellet the debris. Supernatants were transferred to new tubes and re-centrifuged and the resultant supernatant was stored at -80°C until future use. n = 5 mice per group.

4. Results

4.1. AD mediated macroautophagy in AECII: A pro-apoptotic anti-survival mechanism

4.1.1. AD-induced AECII apoptosis is not induced by cathepsin D

Considering that AD significantly increases the expression of cathepsin D in AECII (Figures 1.9B, C and E) and cathepsin D mediates apoptosis of AECII in the mouse model of Hermansky - Pudlak syndrome (HPS) associated lung fibrosis (Mahavadi *et al.,* 2010), it was reasonable to speculate that AD-induced AECII apoptosis might be primed by cathepsin D. To analyze this, MLE12 cells were transfected with cathepsin D specific siRNA (CatDsi) and non-targeting siRNA (NTsi) for 48 hours and subsequently treated with AD or Veh for 8 hours. A significant knockdown of cathepsin D was observed under both AD and Veh treatment (Figures 4.1A and B). Although a slight reduction in cleaved caspase 3 levels was noted under AD treated cathepsin D knockdown condition (Figure 4.1A), it was found to be insignificant (Figure 4.1B). A modest increase in cleaved caspase 3 levels observed during Veh (NTsi) treatment might have resulted from the stress of transfection, which was abrogated upon cathepsin D knockdown (Figures 4.1A and B). This clearly indicates that cathepsin D mediates transfection-stress induced apoptosis but not AD-induced AECII apoptosis. Further, cathepsin D knockdown did not alter the accumulation of proSP-C nor did it influence the lipidation of LC3B following AD treatment (Figures 4.1A, D and E).

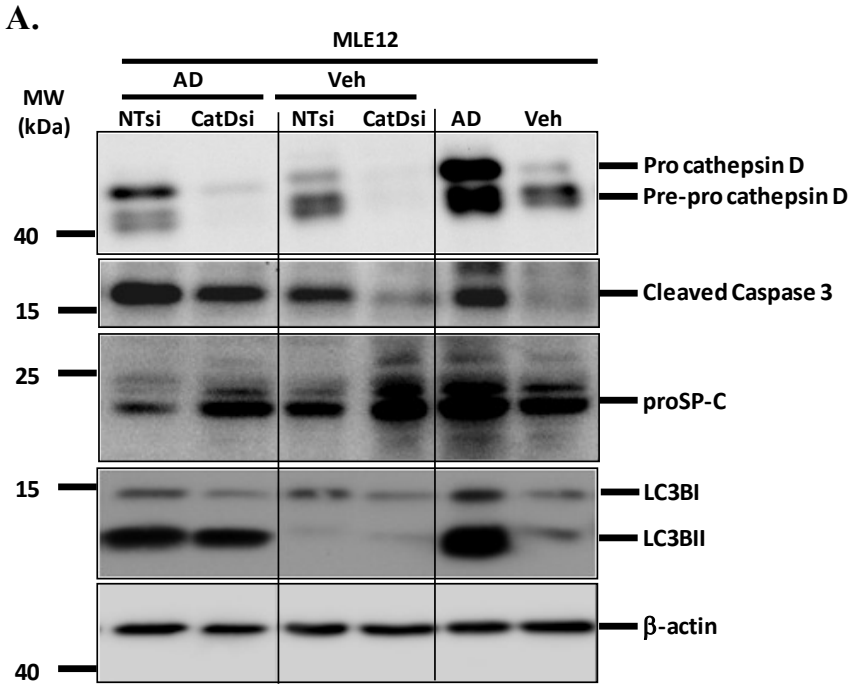

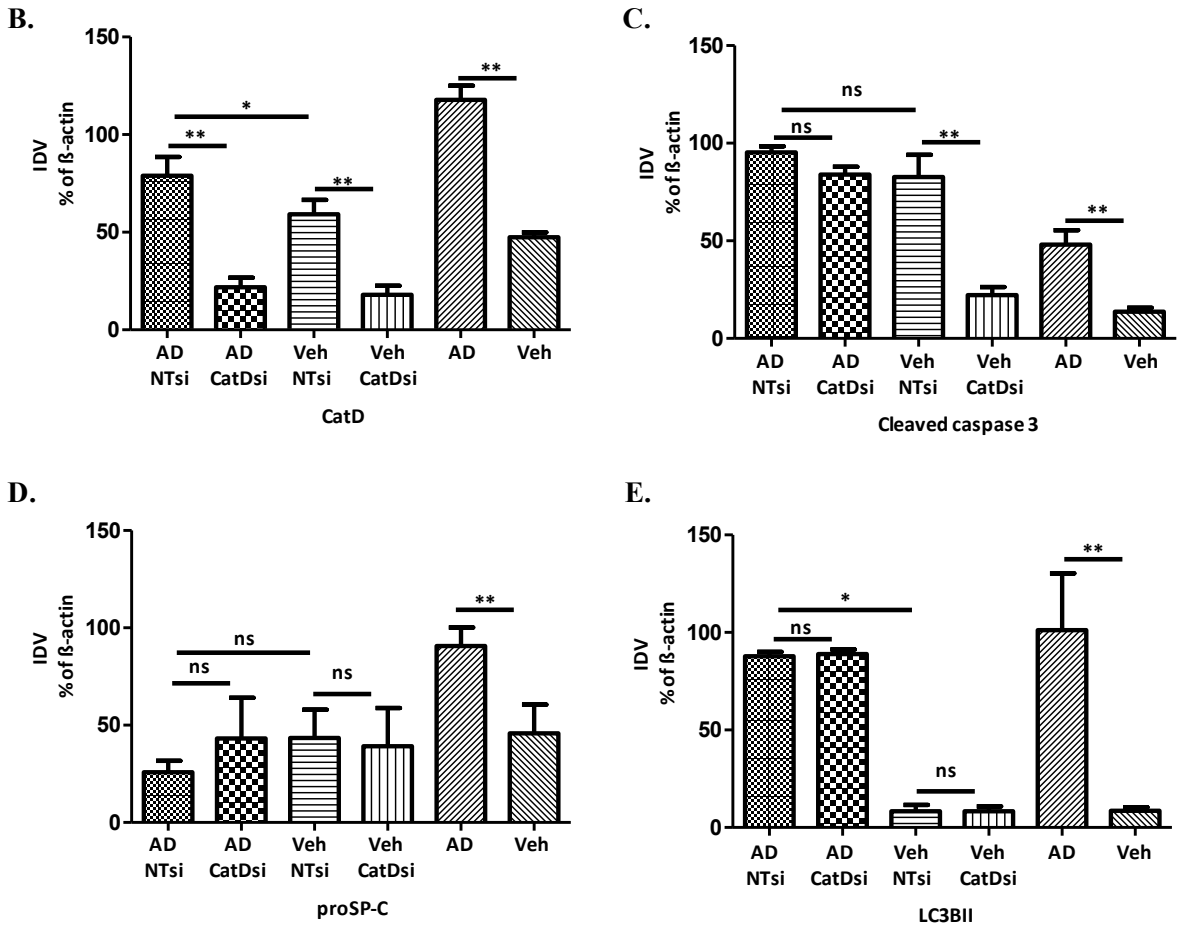

Figure 4.1: AD-induced alveolar epithelial cell apoptosis is not mediated by Cathepsin D.
(A) Representative western blot images for cathepsin D, cleaved caspase 3, proSP-C, LC3 and β-actin (loading control) from 8 hours of AD or Veh treated MLE12 cells transfected with non-targeting siRNA (NTsi) or cathepsin D siRNA (CatDsi). n = 3 independent experiments. (B, C, D and E) Densitometry analysis of triple target proteins' blots namely cathepsin D, cleaved caspase 3, proSP-C, LC3 and β-actin (loading control) and target protein*100/β-actin ratio was calculated and represented as bar graphs. **p < 0.01, *p < 0.05, ns - no significance.

4.1.2. LC3B mediates AECII apoptosis upon AD treatment

Since autophagy is suggested be a key player in determining the life and death of cells and organisms (Wirawan *et al.,* 2012), we further investigated the role of macroautophagy in AD-induced AECII apoptosis. To examine this, a knockdown analysis similar to the previously explained cathepsin D knockdown was performed in MLE12 cells with LC3B-siRNA (LC3si) versus the non-targeting siRNA (NTsi). Under AD or Veh treatment, the knockdown of LC3B was evident in MLE12 cells (Figures 4.2A and B). Although no change was noted in the level of autophagy substrate p62 in the AD or Veh treated LC3B knocked down MLE12 cells (Figures 4.2A and C), a significant decrease in the cleaved caspase 3 level was observed under both conditions (Figures 4.2A and D). This implies a pivotal role of LC3B (autophagy) in regulating apoptosis of alveolar epithelial cells upon AD treatment. In

addition, siRNA against LC3B also attenuates transfection induced apoptosis. AD-induced proSP-C accumulation was also abated upon knockdown of LC3B (Figures 4.2A and D).

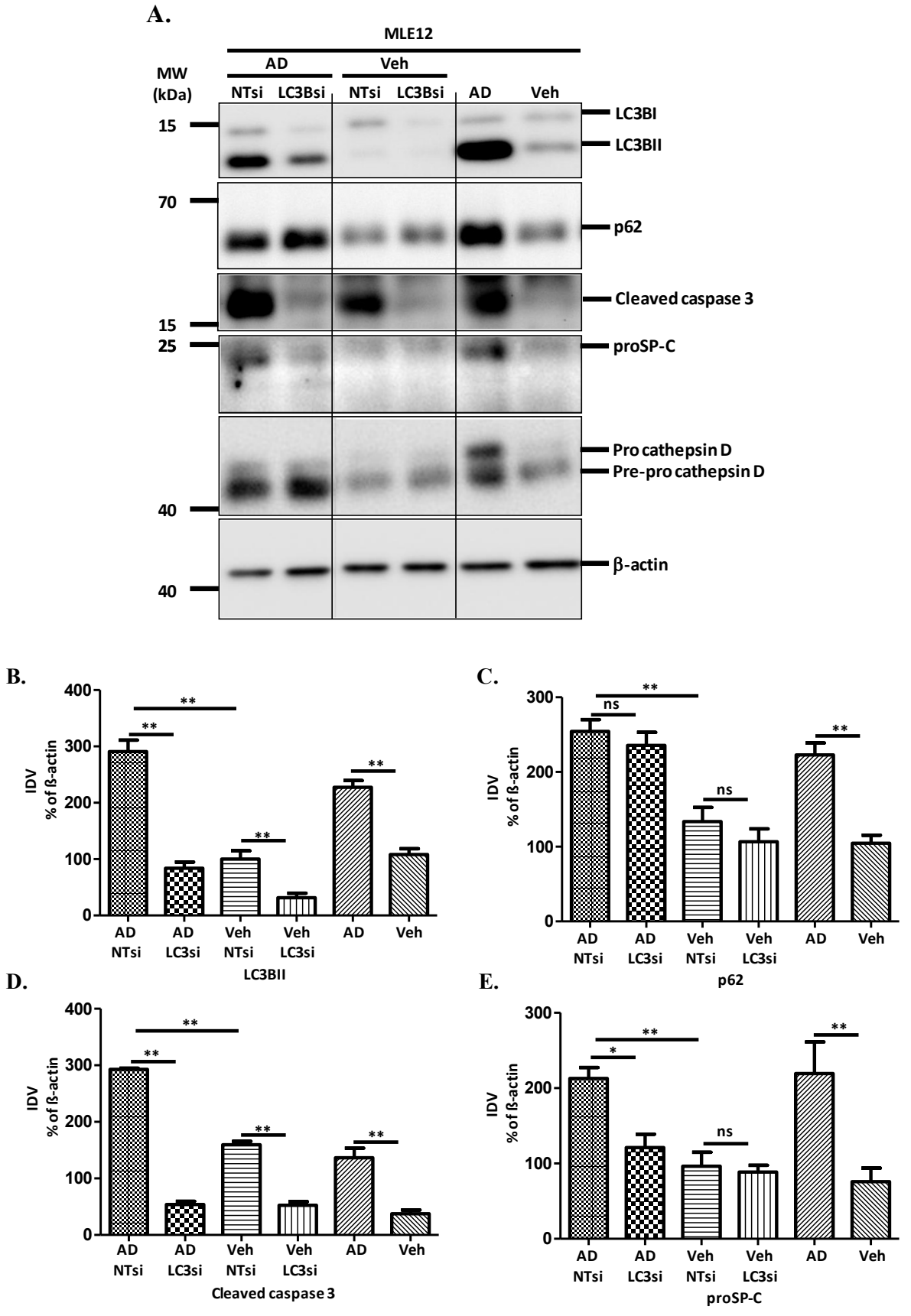

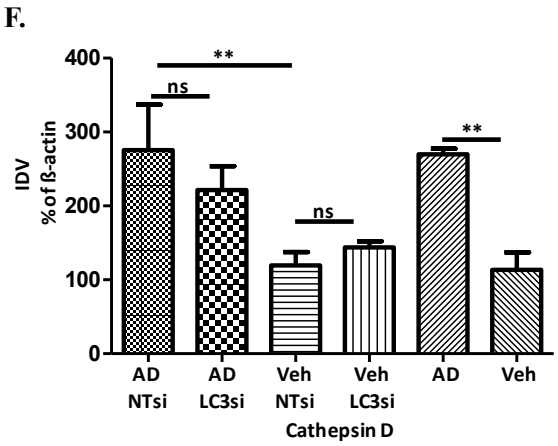

Figure 4.2: LC3B mediate AECII apoptosis in AD treated MLE12 cells.
(A) Representative western blot images for LC3B, cleaved caspase 3, proSP-C, cathepsin D and β-actin (loading control) from 8 hours of AD or Veh treated MLE12 cells transfected with non-targeting siRNA (NTsi) or LC3B siRNA (LC3si). n = 3 independent experiments. (B, C, D and E) Densitometry analysis of triple target proteins' blots namely LC3B, cleaved caspase 3, proSP-C, cathepsin D and β-actin (loading control)) and target protein*100/β-actin ratio was calculated and represented as bar graphs. **p < 0.01, *p < 0.05, ns - no significance.

Upon LC3B knockdown, cathepsin D levels remained unaltered in AD treated MLE12 cells reaffirming that AD-induced AECII apoptosis is dependent on LC3B and not cathepsin D. Therefore, this analysis shows a pivotal role of macroautophagy, particularly of LC3B in mediating AECII cell death and proSP-C accumulation following AD treatment.

4.2. Autophagy flux under AD treatment

4.2.1. AD induces lysosomal biogenesis in murine alveolar epithelial cells

In line with the increased expression of cathepsin D observed upon AD treatment, the expression of lysosomal-associated membrane protein 1 (LAMP1) and LAMP2 were also noted to be prominently upregulated in the lung homogenates of AD treated mice (day 7 - 28) (Figures 4.3A, B and C). Immunofluorescence analysis of LAMP1 and LAMP2 revealed an intensive staining for LAMP1 and LAMP2 in 8 hours of AD treated cells in contrast to the fine punctate staining observed among the Veh treated controls (Figure 4.3D).

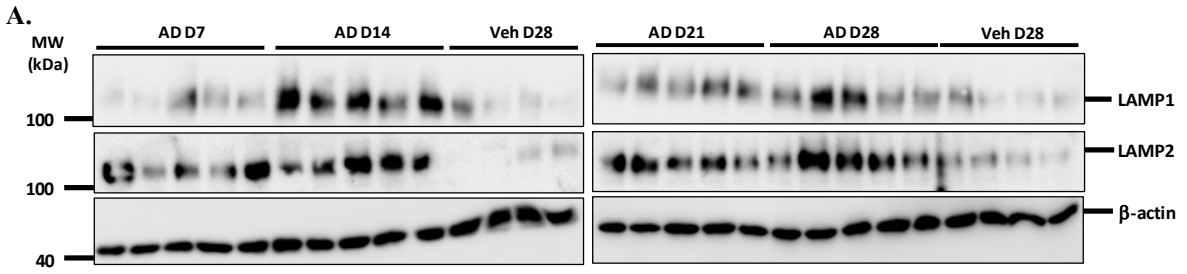

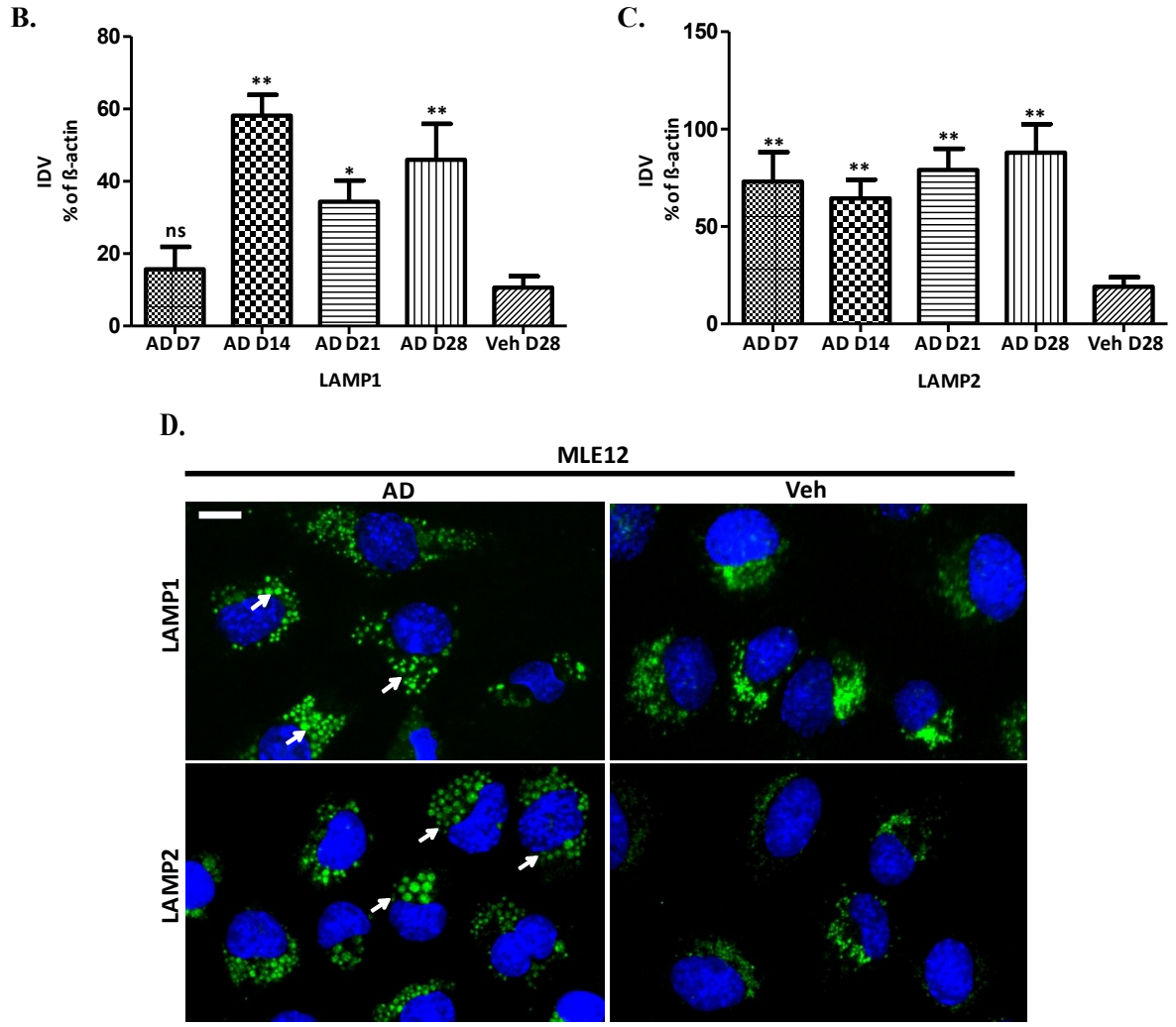

Figure 4.3: Increased lysosomal biogenesis in mice AECs under AD treatment.
(A) Western blot analysis of lung homogenates of (left) AD treated mice (day 7, 14) and Veh treated mice (day 28) and (right) AD treated mice (day 21, 28) and Veh treated mice (day 28) for LAMP1, LAMP2 and β-actin (loading control). n = 5 mice per group. (B, C) Densitometry analysis of the target proteins' blots and target protein*100/β-actin ratio was calculated and represented as a bar graph. **p < 0.01, *p < 0.05, ns - no significance. (D) Immunofluorescence analysis of 8 hours of AD or Veh treated MLE12 cells for LAMP1 and LAMP2 (green). Nuclei are stained with DAPI (blue). Arrows indicate increased swollen LAMP1 and LAMP2 staining in the perinuclear regions of AD treated MLE12 cells versus the Veh. n = 3 independent experiements. Scale bar = 10 µm.

It is hence obvious, AD does not only increase the production of lysosomal enzymes *viz* cathepsin D, but also induces the lysosomal biogenesis *per se*.

4.2.2. Increase in autophagy flux under AD treatment

Since AD-induced fusion of autophagosomes with lysosomes was evident in MLE12 cells, the autophagy flux under AD treatment was then analysed using the vacuolar ATPase (V-ATPase) inhibitor, Bafilomycin A1 (Baf A1). MLE12 cells were pre-treated with Baf A1 (100 nM) for 1 hour, prior to the treatment with 8 hours of AD or Veh. The vacuolar

cytopathology induced by AD in the MLE12 cells was found to be completely abrogated upon bafilomycin A1 pre-treatment (Figure 4.4A). A similar result was also obtained upon co-treating MLE12 cells with Baf A1 and AD (Figure 4.4B). This is in accordance with the observation of Morissette *et al.,* 2009, who demonstrated that bafilomycin A1 inhibits vacuolization and the cellular uptake of AD. Thus, another autophagy inhibitor, Chloroquine (CQ) (10 µg/ml and 30 µg/ml), was used to analyze flux in MLE12 cells under AD treatment. A significant increase in LCBII level was evident in CQ pre-treated MLE12 cells, followed by AD treatment, than AD treated MLE12 cells alone (Figure 4.4C). From this result, it is apparent that AD increases autophagy flux in MLE12 cells.

A.

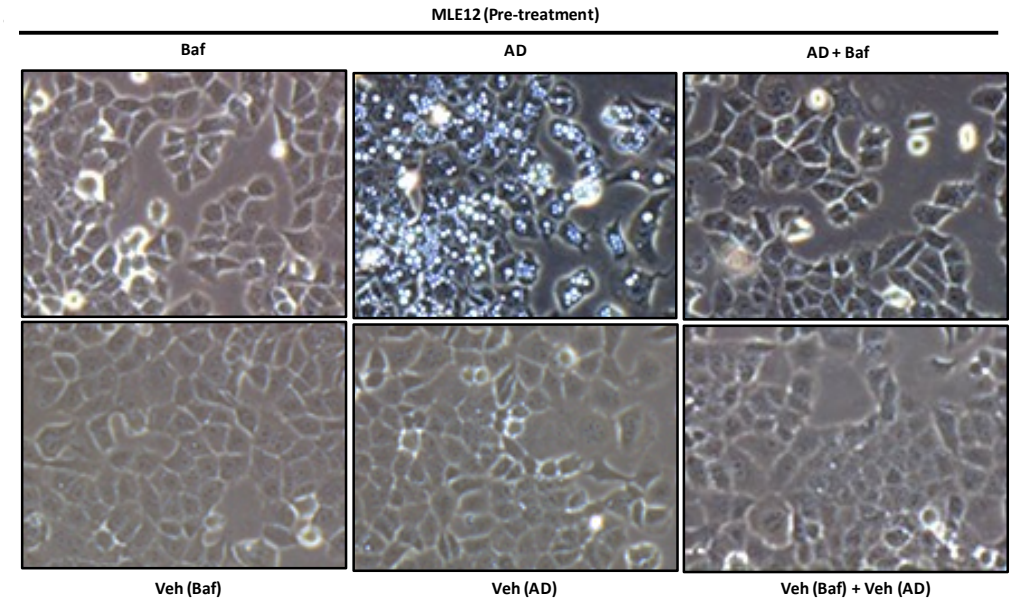

B.

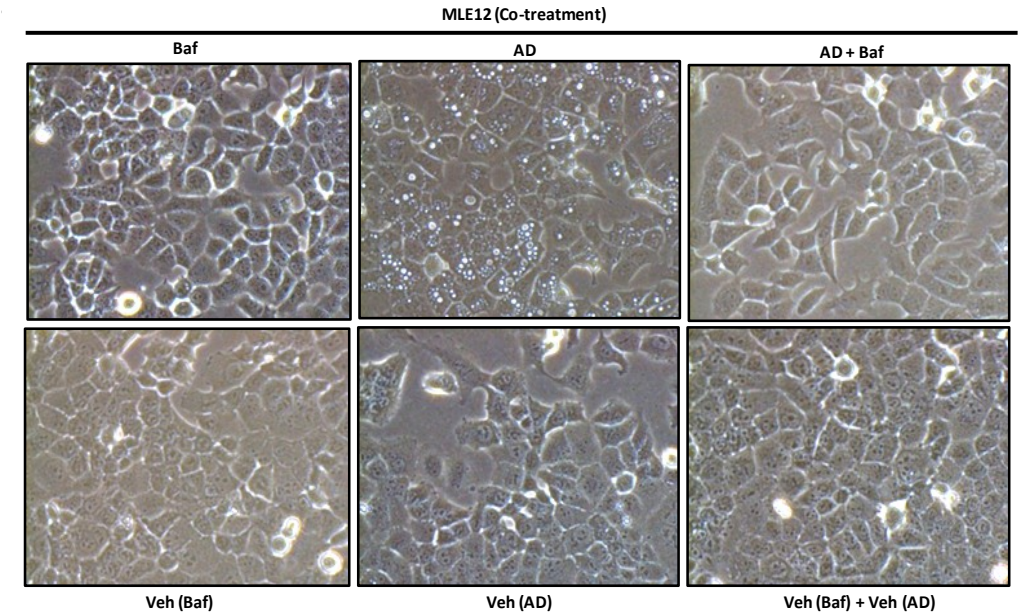

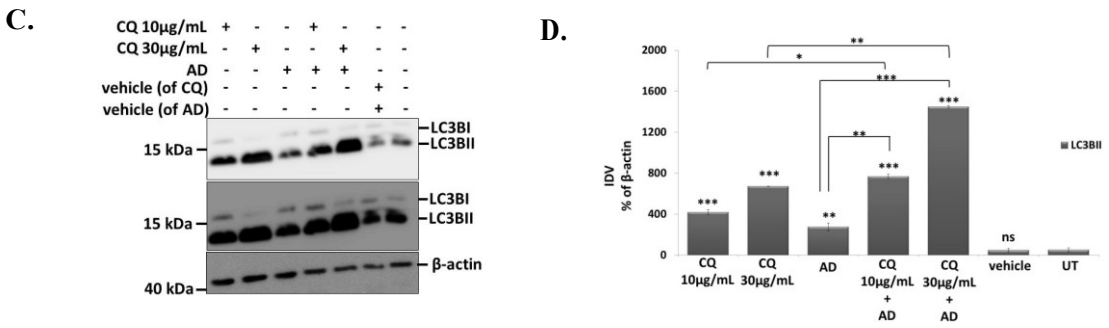

Figure 4.4: AD increases autophagy flux in MLE12 cells.
(A, B) Phase-contrast images of MLE12 cells pre-treated or co-treated with Baf A1, prior to 8 hours of AD or Veh treatment. (C) Representative western blot images for LC3B and β-actin (loading control) from lysates obtained from 4 hours of CQ pre-treated MLE12 cells, followed by 8 hours of AD or Veh treatment. n = 3 independent experiments. Densitometry analysis of the target proteins' blots and target protein*100/β-actin ratio was calculated and represented as a bar graph. . ***p < 0.001,**p < 0.01, *p < 0.05, ns - no significance.

4.3. Mitophagy in murine model of AD-induced pulmonary fibrosis

4.3.1. AD escalates ROS production in mice AECs

In order to determine if AD increases ROS production (superoxide and peroxynitrite radicals), MLE12 cells were treated with AD (10 µg/ml) or Veh for 8 hours and incubated with the CMH spin probe. To determine the amount of superoxide radicals ($O_2^{\cdot-}$) in particular, a pre-incubation step with pSOD was performed prior to incubation with the CMH spin probe and later the ESR were measured for the stored shock frozen samples. The ESR spectra were obtained as represented (Figures 4.5A, B, C and D) for CMH+AD, CMH+Veh, CMH+pSOD+AD and CMH+pSOD+Veh treated samples respectively.

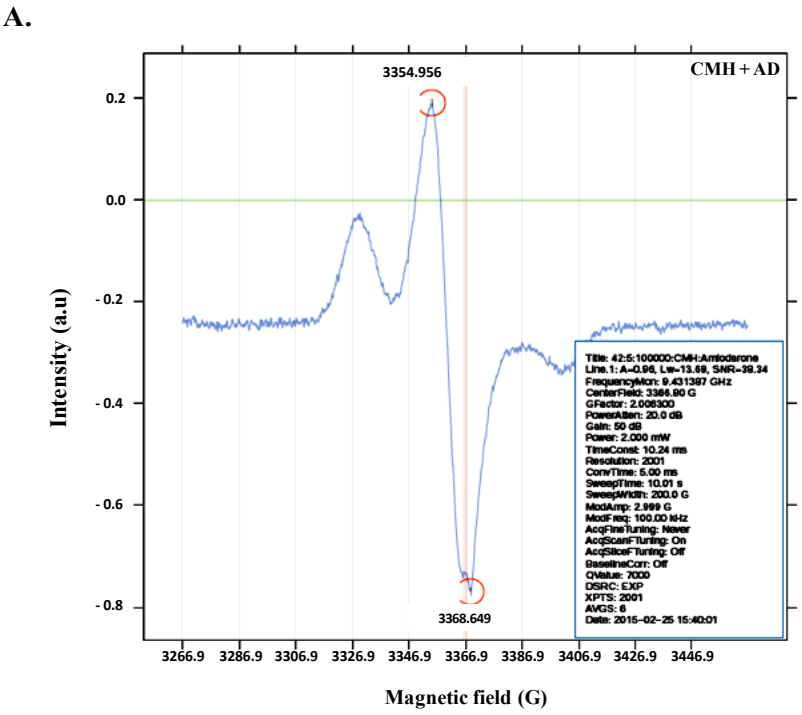

B.

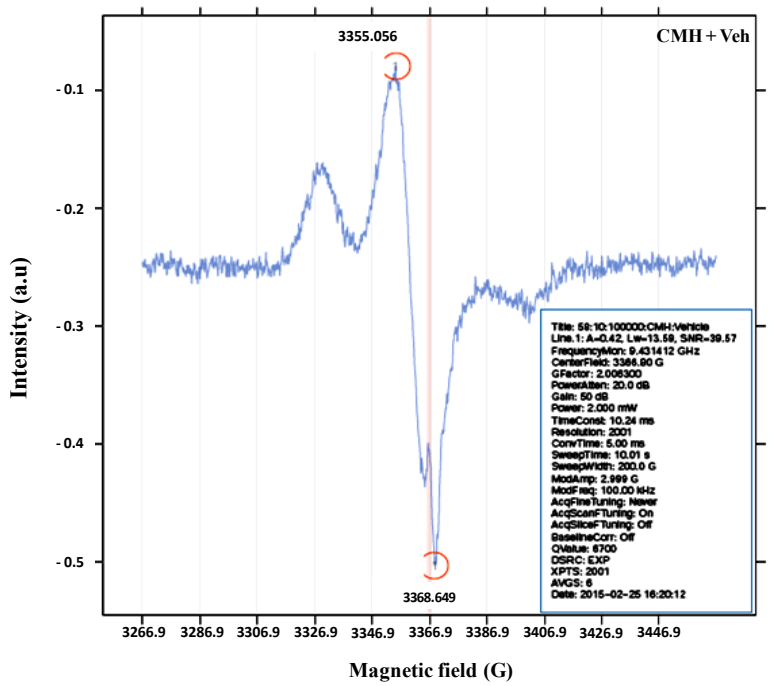
3355.056
CMH + Veh
3368.649
Intensity (a.u)
Magnetic field (G)
- 0.1
- 0.2
- 0.3
- 0.4
- 0.5
3266.9
3286.9
3306.9
3326.9
3346.9
3366.9
3386.9
3406.9
3426.9
3446.9

C.

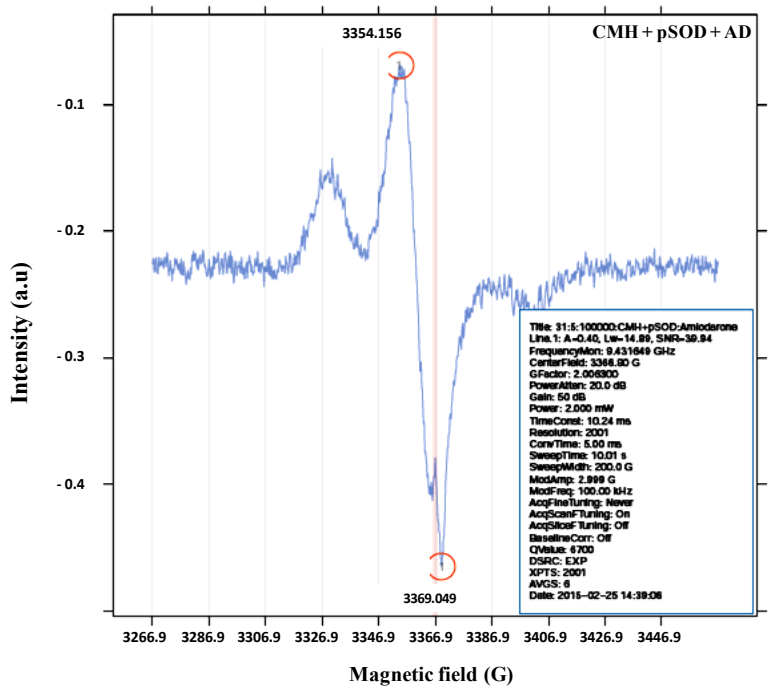
3354.156
CMH + pSOD + AD
3369.049
Intensity (a.u)
Magnetic field (G)
- 0.1
- 0.2
- 0.3
- 0.4
3266.9
3286.9
3306.9
3326.9
3346.9
3366.9
3386.9
3406.9
3426.9
3446.9

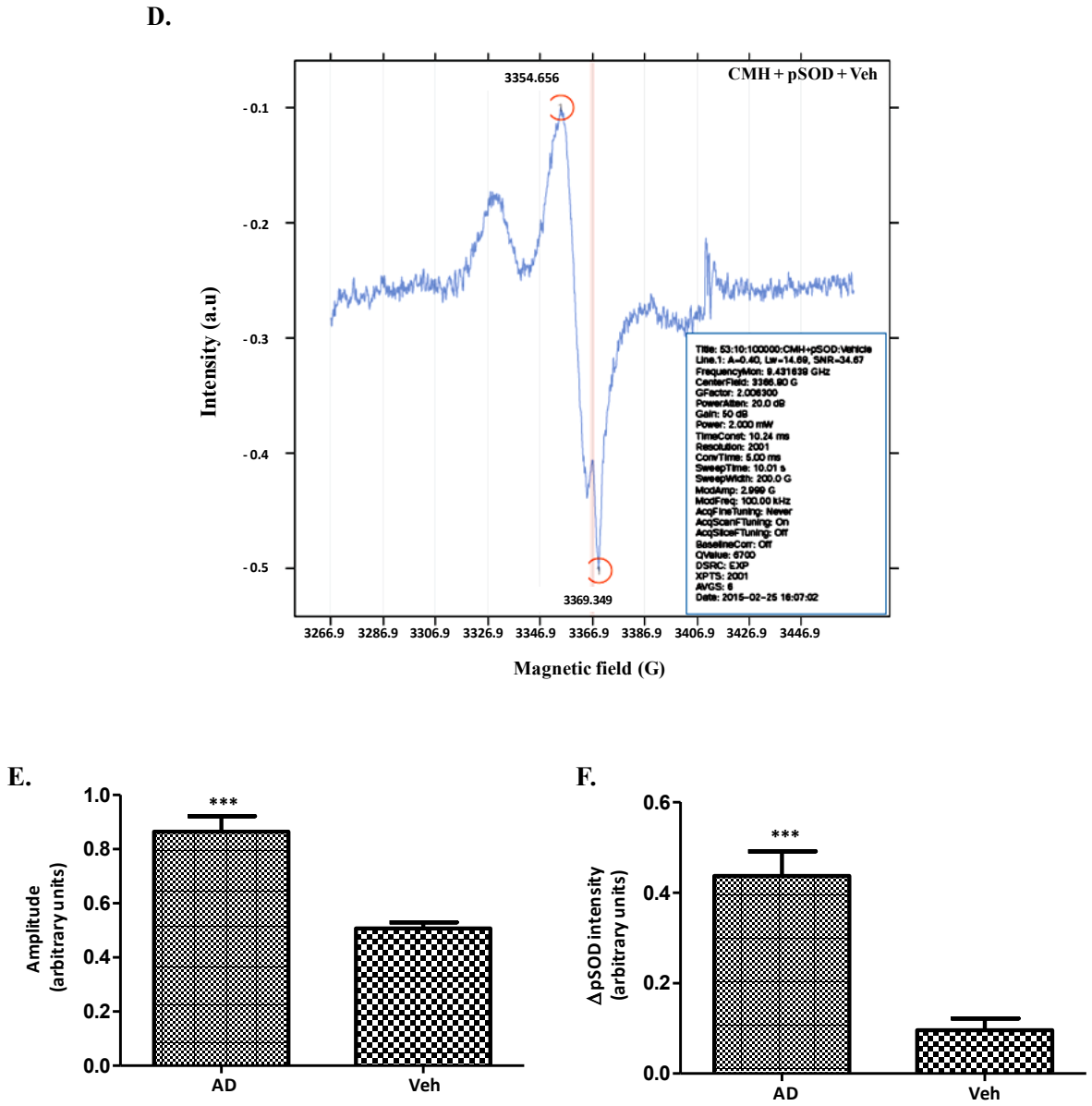

Figure 4.5. Elevated ROS production in AD treated mice alveolar epithelial cell line.
(A, B, C and D). Representative ESR spectra obtained for 8 hours of AD or Veh treated MLE12 cells (105 cells/300 µl) probed with CMH and CMH + pSOD respectively. n = duplicate set of 5 samples per group. The green line represents zero intensity. X-axis: Magnetic field (G), Y-axis: Intensity (a.u). a.u = arbitrary units. (E). Graphical representation of ROS production in CMH probed AD or Veh treated MLE12 cells by calculating the average ESR spectral intensities. ***p < 0.0001. (F). Graphical representation of superoxide radical ($O_2^{\cdot-}$) production in AD or Veh treated MLE12 cells by calculating the difference between the average ESR spectral intensities obtained from CMH and CMH + pSOD probed AD or Veh treated MLE12 cells. ***p < 0.0001.

Upon averaging the spectral intensities obtained from CMH+AD and CMH+Veh treated samples, an increased production of ROS was evident in MLE12 upon AD treatment (Figure 4.5E), and then a remarkable rise in the production of superoxide radicals ($O_2^{\cdot-}$) was also noted in AD treated MLE12 cells (Figure 4.5F). These results thus prove the inherent ability of AD to generate ROS in a murine alveolar epithelial cell line.

4.3.2. AD increases mitochondrial mass in murine AECII

Since significant increase in ROS production was observed in AD treated MLE12 cells and as mitochondria are a major source of ROS production, we further investigated if increased ROS may be attributed to altered mitochondrial homeostasis under conditions of AD treatment. Hence, we first examined the protein expression of the mitochondrial protein, Cytochrome c oxidase subunit IV (COX IV) in the lung homogenates of day 7, 14, 21 and 28 of the AD and day 28 of Veh treated C57/Bl6 mice. A significant upregulation in the expression of COX IV (~ 2 to 2.5-fold) was observed starting day 7 after AD treatment (Figures. 4.6A and B).

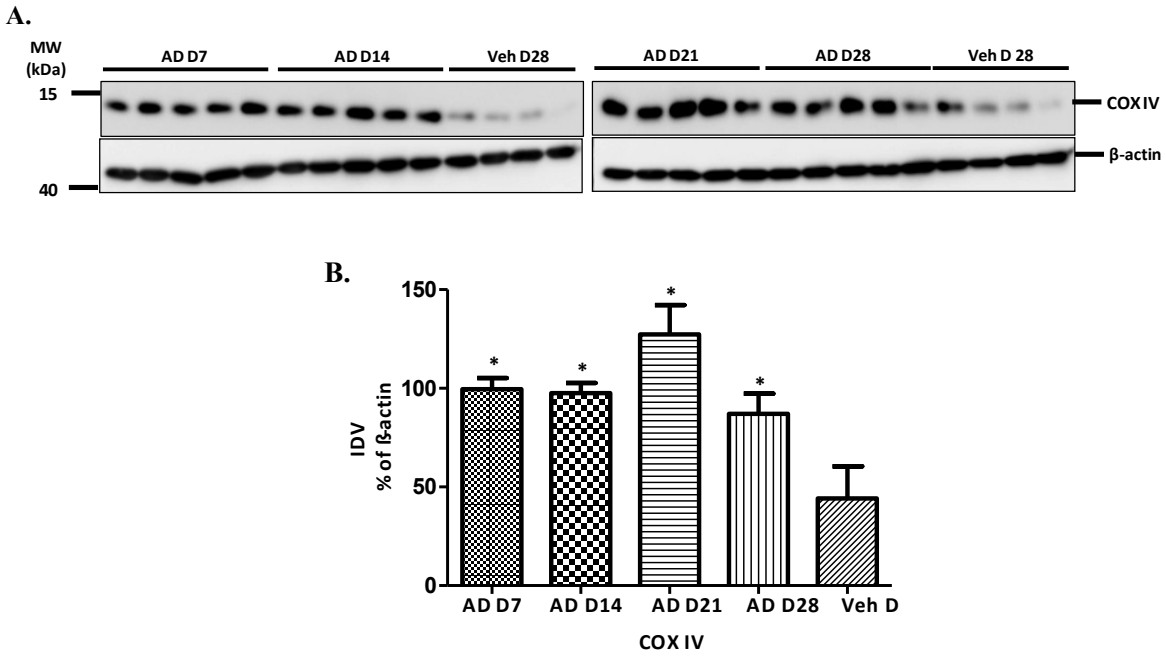

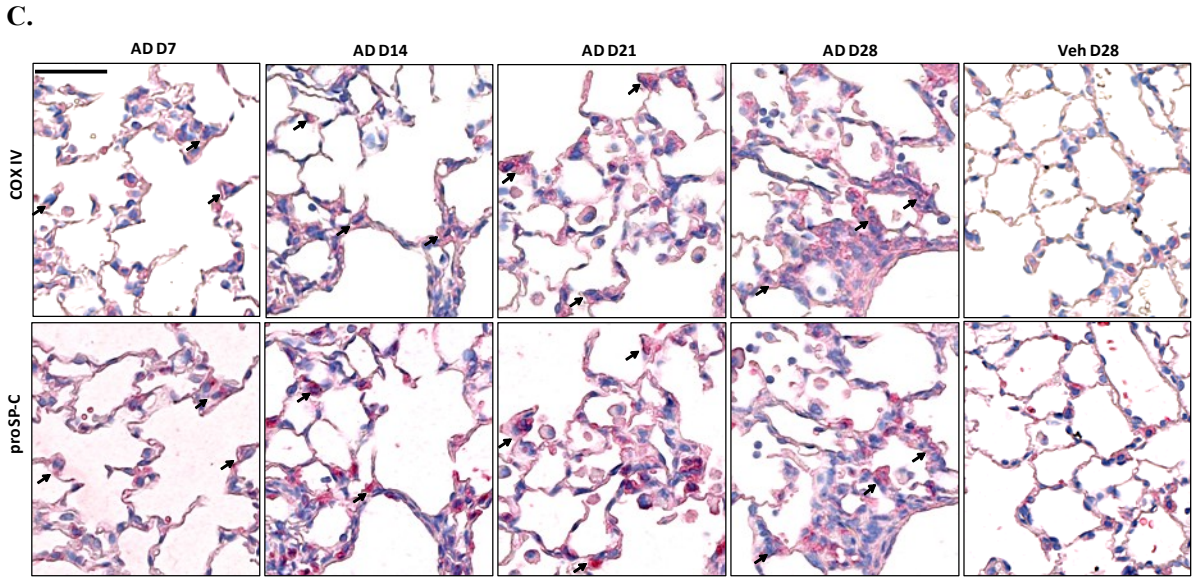

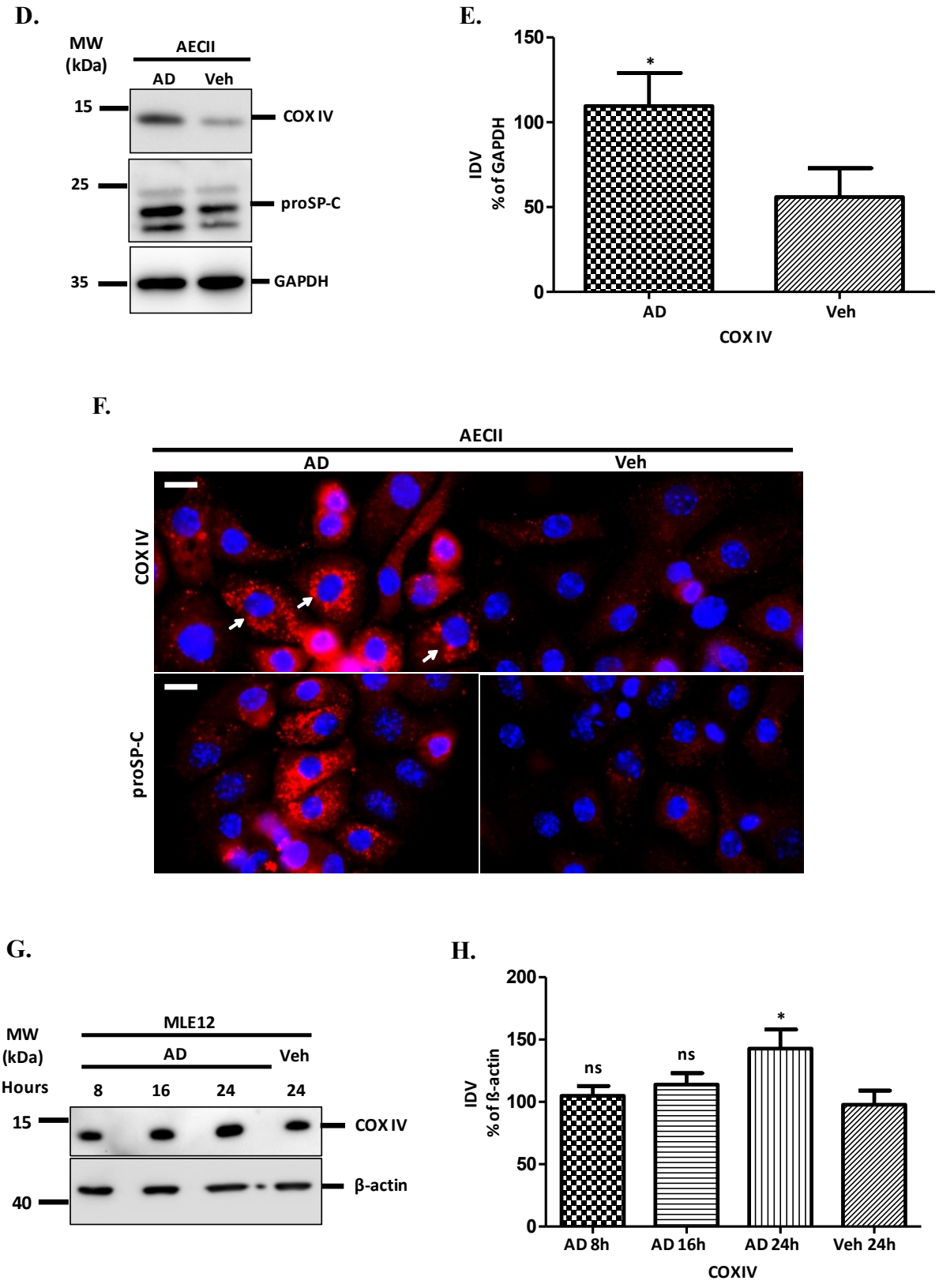
D.
MW (kDa)
AECII
AD
Veh
15
25
35
COX IV
proSP-C
GAPDH
E.
IDV % of GAPDH
150
100
50
0
*
AD
Veh
COX IV
F.
AECII
AD
Veh
COX IV
proSP-C
G.
MW (kDa)
MLE12
AD
Veh
Hours
8
16
24
24
15
40
COX IV
β-actin
H.
IDV % of β-actin
200
150
100
50
0
ns
ns
*
AD 8h
AD 16h
AD 24h
Veh 24h
COXIV

I.

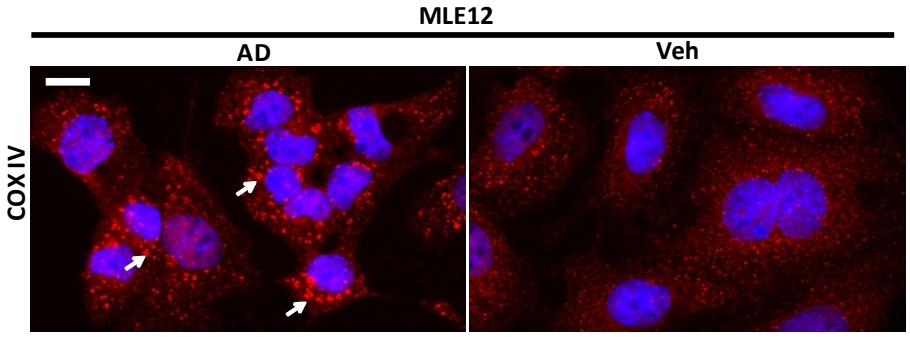

Figure 4.6. Increase in mitochondrial mass in murine alveolar epithelial cells after AD treatment.
(A) Western blot analysis of lung homogenates of (left) AD treated mice (day 7, 14) and Veh treated mice (day 28) and (right) AD treated mice (day 21, 28) and Veh treated mice (day 28) for COX IV and β-actin (loading control). n = 5 mice per group. (B) Densitometry analysis of the COX IV and β-actin blots and COX IV*100/β-actin ratio was calculated and represented as a bar graph. *p < 0.05. (C) Immunohistochemical analysis of serial lung sections of AD (day 7, 14, 21 and 28) and Veh (day 28) treated mice for COX IV and proSP-C. Arrows indicate AECII showing increased COX IV expression from day 7 of AD treatment. n = 5 mice per group. Scale bar = 50 µm. Original magnification: x400. (D) Representative western blot images for COX IV, proSP-C and GAPDH (loading control) from 24 hours of AD or Veh treated C57Bl/6 murine AECII' lysates. n = 3 independent experiments. (E) Densitometry analysis of triplicate blots of COX IV and GAPDH and COX IV*100/GAPDH ratio was calculated and represented as a bar graph. *p < 0.05. (F) Immunofluorescence analysis of 24 hours of AD or Veh treated murine AECII for COX IV (red). Nuclei are stained with DAPI (blue). Arrows indicate cells showing increased COX IV expression under AD treatment. n = 3 independent experiments. Scale bar = 10 µm. (G) Representative western blot images for COX IV and β-actin (loading control) from 8, 16 and 24 hours of AD and 24 hours of Veh treated MLE12 cells' lysates. n = 3 independent experiments. (H) Densitometry analysis of triplicate blots of COX IV and β-actin and COX IV*100/β-actin ratio was calculated and represented as a bar graph. *p < 0.05, ns = no significance. (I) Immunofluorescence analysis of 8 hours of AD or Veh treated MLE12 cells for COX IV (red). Nuclei are stained with DAPI (blue). Arrows indicate increased COX IV expression in the perinuclear region and on the margins of vacuoles under AD treatment. n = 3 independent experiments. Scale bar = 10 µm.

Immunohistochemical analysis for COX IV and proSP-C (AECII marker) performed on serial lung sections revealed an increased localization of COX IV to AECII in AD treated (day 7, 14, 21 and 28) mice compared to the Veh treated (day 28) control mice (Figure 4.6C). In order to find if COX IV upregulation is substantial in the alveolar epithelium, AECII from C57/Bl6 mice were isolated and treated with 10 µg/ml of AD or Veh for 24 hours and analysed for the expression of COX IV. In line with the AD treated lung homogenates, COX IV expression was significantly increased (~ 2-fold) in AD treated AECII *in vitro* (Figures 4.6D and E). Similarly, immunoblot analysis of MLE12 cells treated with same concentration of AD for 24 hours also demonstrated a prominent increase (~ 1.5-fold) in COX IV expression (Figures 4.7G and H). Under AD treatment, the immunofluorescence analysis of murine AECII and MLE12 cells showed marked increase in COX IV expression compared to the Veh (Figures 4.6F). In particular, in AD treated MLE12 cells, COX IV were partly observed to be localised in the perinuclear region, especially on the margins of the giant vacuolar structures induced by AD

(Figure 4.6I). Altogether, the data point towards increased mitochondrial biogenesis in AECII following AD treatment.

4.3.3. AD induces differential expression of mitophagy proteins in murine AECII

It has been reported that AD induces autophagy (Mahavadi et al., 2015) and we now show that AD treated alveolar epithelial cells display excessive ROS production and mitochondrial biogenesis. We hence asked if AD promotes mitochondrial autophagy/mitophagy. Therefore, the expression level of different mitophagy proteins Bnip3L, Bnip3, p62, NBR1, ATG12-ATG5 and ATG7 was investigated. Western blot analysis of the AD (day 7, 14, 21 and 28) and Veh (day 28) treated lung homogenates revealed no significant difference in the expression of mitophagy receptor proteins BNIP3L (homodimer and monomer) and BNIP3 (Figures 4.7A, B, C and D). In concordance, there was unaltered Bnip3L (homodimer and monomer) and Bnip3 protein expression in the AD or Veh treated isolated murine AECII (Figures 4.8A, B, C and D) and MLE12 cells (Figures 4.9 A, B, C and D).

The expression of autophagy adaptor proteins p62 and NBR1 was then evaluated in AD treated mice lung homogenates. Apart from acting as substrates for autophagy, both of these proteins also serve as cargo receptors for ubiquitinated substrates. As reported previously (Mahavadi *et al.,* 2015), a significantly increased expression of p62 (~ 1.5 to 2-fold) was observed from day 14 of AD treatment in the lung homogenates of C57Bl/6 mice (Figures 4.7A and B). Immunohistochemical analysis for p62 and proSP-C (AECII marker) on the serial mice lung sections revealed increased localization of p62 to AECII in the lung sections of AD treated (day 7, 14, 21 and 28) mice compared to the Veh treated (day 28) control mice (Figure 4.7I). In complete agreement, western blot analysis of 24 hours of AD treated murine AECII also demonstrated a significant rise (~ 2-fold) in the expression of p62 (Figures 4.8A and E). Likewise, AD (8, 18 and 24 hours) treated MLE12 cells also exhibited an increase (~ 2 to 2.5-fold) in p62 expression versus the Veh (Figures 4.9A and E). In addition, the expression of NBR1 protein was found to be significantly increased (~ 2 to 2.5-fold) in the lung homogenates of AD (day 14, 21 and 28) treated mice (Figures. 4.7A and F). However, the expression of NBR1 remained unaltered in AD and Veh treated murine AECII (Figures 4.8A and F) and MLE12 cells *in vitro* (Figures 4.9A and F). The increase in NBR1 protein levels in AD treated mice lung homogenates but not in AD treated murine AECII and MLE12 cells *in vitro* could be attributed to the diverse cell population present within the lung.

In addition, the expression of conventional macroautophagy proteins, ATG12-ATG5 and ATG7 was also analyzed, as deficiency of these proteins has been proven to induce mitochondrial defects and hinder the clearance of damaged mitochondria (Wu *et al.,* 2009, Liu *et al.,* 2012). Immunoblot analysis of the AD treated mice lung homogenates, murine AECII and MLE12 treated with AD *in vitro* displayed proficient increase in the expression of ATG12-ATG5 (~ 1.5-fold) in comparison to the Veh treated controls (Figures 4.7A and G, 4.8A and G, 4.9A and G). Similar to AD-induced ATG12-ATG5 expression, immunoblot analysis of AD (day 7, 21 and 28) treated mice lung homogenates exhibited significant upregulation (~ 2-fold) of ATG7 expression versus the Veh (Figures 4.7A and H). Immunohistochemical analysis for ATG7 and proSP-C (AECII marker) on the serial lung sections revealed an increased staining of ATG7 in AECII in lung sections of AD treated (day 7, 14, 21 and 28) mice compared to the Veh treated (day 28) control mice (Figure 4.7J). In line with this, *in vitro* AD treated murine AECII (Figure 4.8A and H) and AD treated MLE12 cells (Figures 4.9A and H) also showed a significant increase (~ 2 and ~ 1.5-fold respectively) in the ATG7 expression after 24 hours.

Thus, these results collectively imply unaltered expression of the mitophagy receptor proteins Bnip3L & Bnip3 and the cargo receptor protein NBR1, but an increased synthesis of autophagy adaptor protein p62 and other mitophagy proteins such as ATG12-ATG5 and ATG7 in murine AECII following AD treatment *in vivo* and *in vitro*.

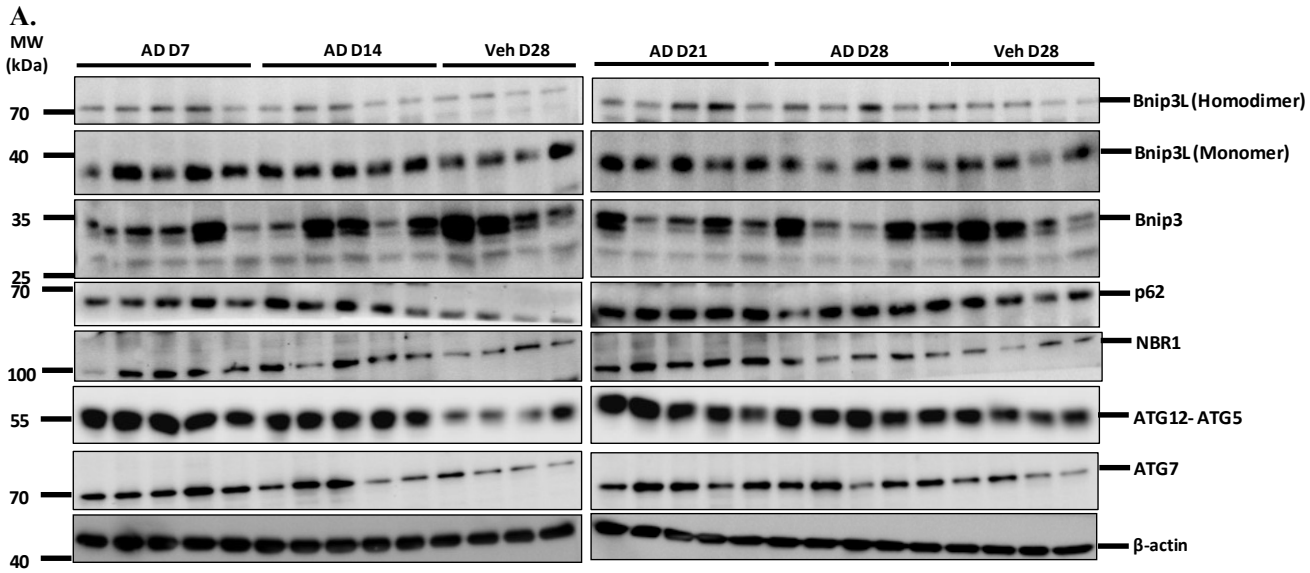

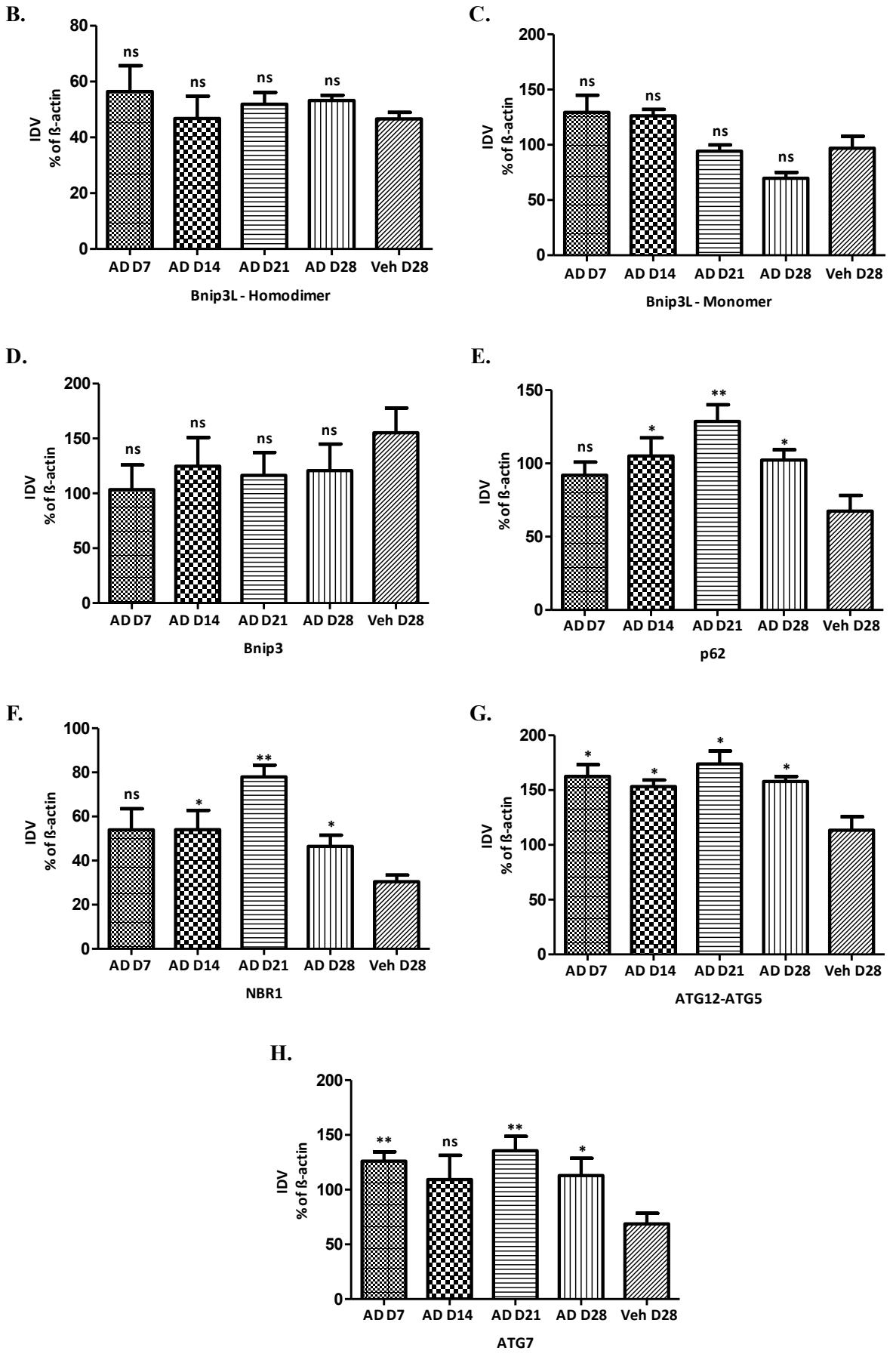
B.
IDV
% of ß-actin
ns
AD D7
AD D14
AD D21
AD D28
Veh D28
Bnip3L - Homodimer
C.
Bnip3L - Monomer
D.
Bnip3
E.
p62
F.
NBR1
G.
ATG12-ATG5
H.
ATG7

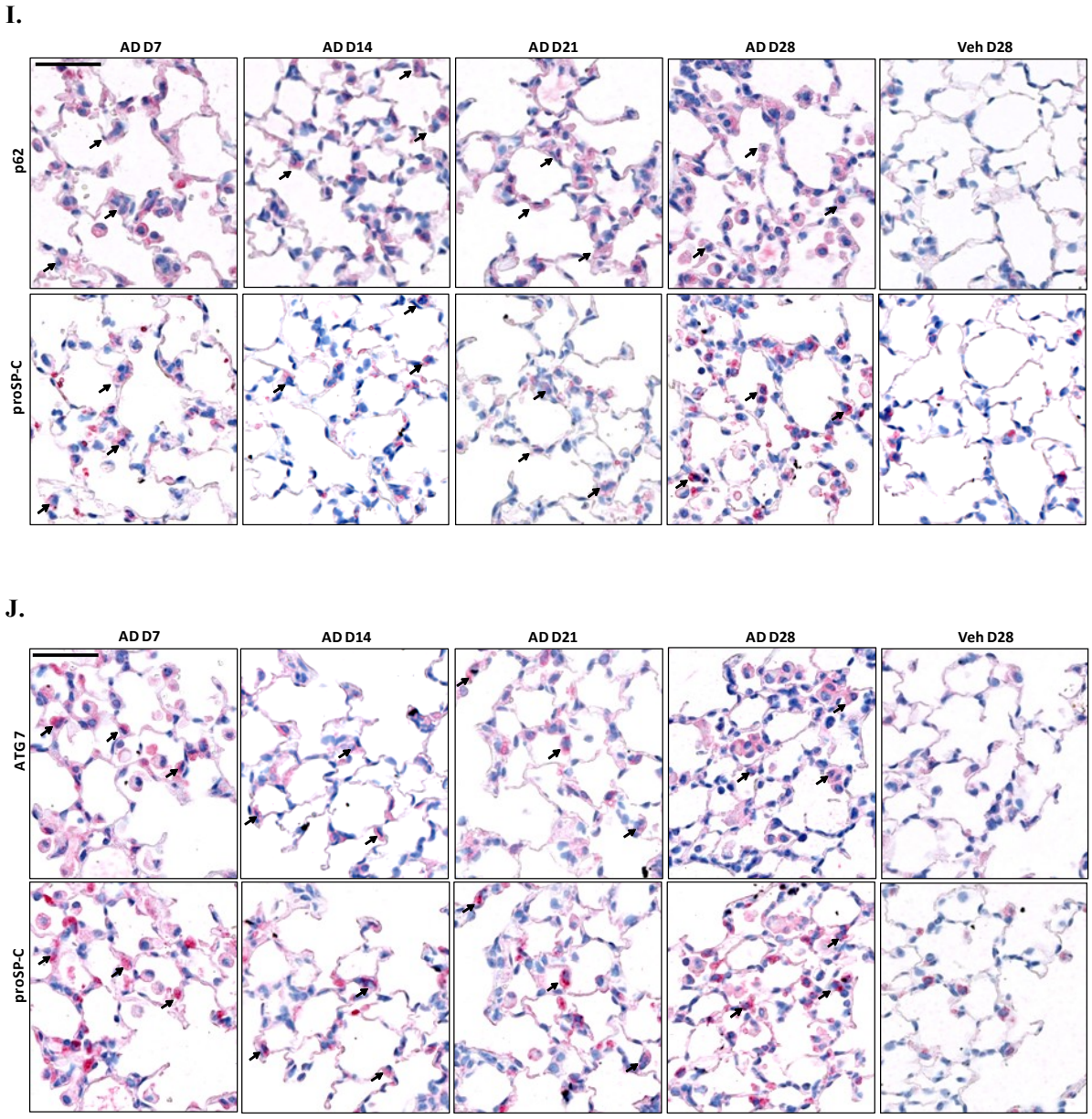

Figure 4.7. Differential expression of mitophagy proteins in AD treated mice lung tissues.
(A) Western blot analysis of lung homogenates of (left) AD treated mice (day 7, 14) and Veh treated mice (day 28) and (right) AD treated mice (day 21, 28) and Veh treated mice (day 28) for Bnip3L (homodimer and monomer), Bnip3, p62, NBR1, ATG12-ATG5, ATG7 and β-actin (loading control). n = 5 mice per group. (B, C, D, E, F, G, H) Densitometry analysis of the target proteins' blots namely Bnip3L (homodimer and monomer), Bnip3, p62, NBR1, ATG12-ATG5, ATG7 and β-actin (loading control) and target protein*100/β-actin ratio was calculated and represented as bar graphs. **p < 0.01, *p < 0.05, ns - no significance. (I) Immunohistochemical analysis of serial lung sections of AD (day 7, 14, 21 and 28) and Veh (day 28) treated mice for p62 and proSP-C. Arrows indicate AECII showing increased p62 expression from day 7 of AD treatment. n = 5 mice per group. Scale bar = 50 µm. Original magnification: x400 (J) Immunohistochemical analysis of serial lung sections of AD (day 7, 14, 21 and 28) and Veh (day 28) treated mice for ATG7 and proSP-C. Arrows indicate AECII showing increased ATG7 expression from day 7 of AD treatment. n = 5 mice per group. Scale bar = 50 µm. Original magnification: x400.

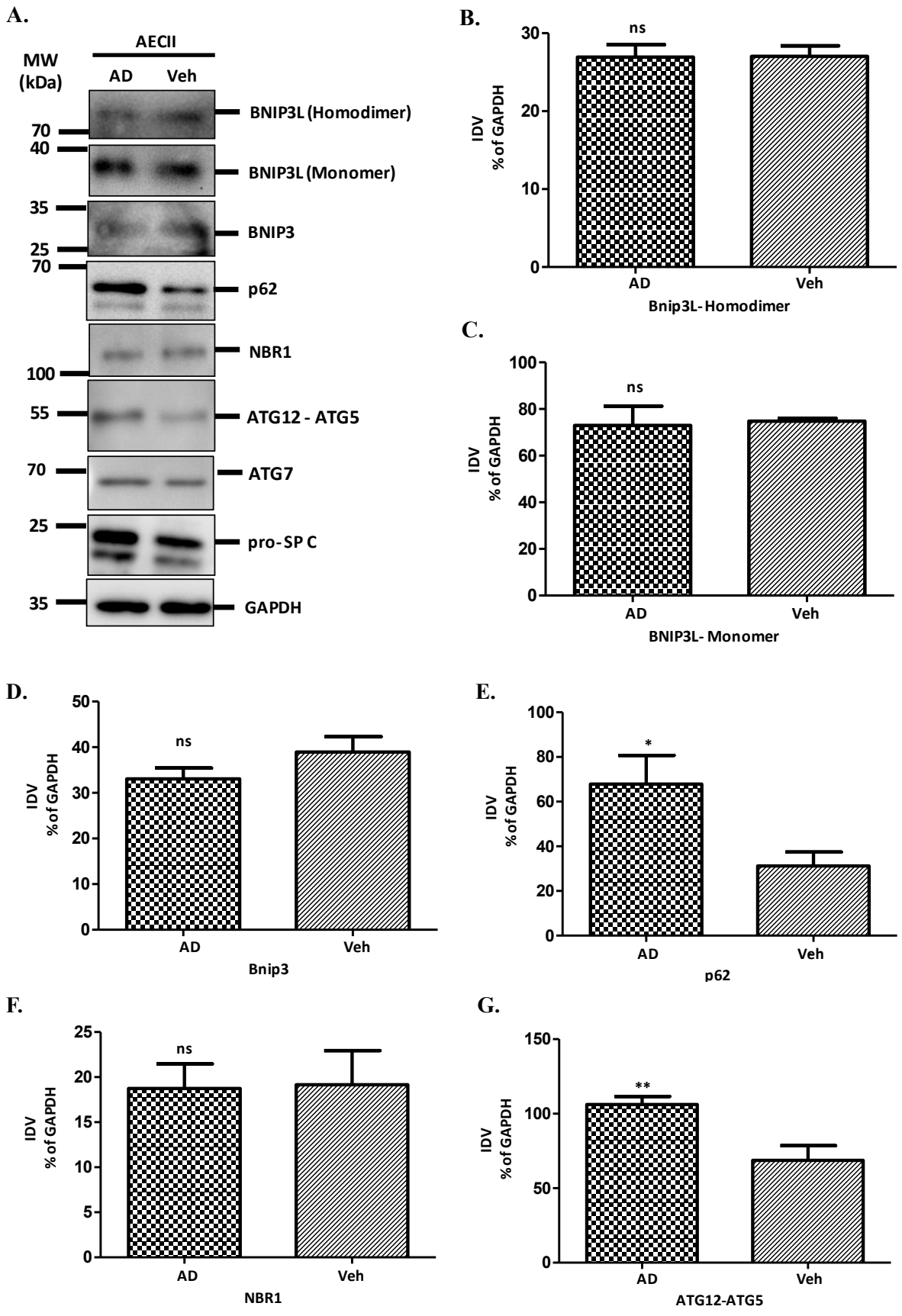
A.
AECII
MW (kDa)
AD
Veh
BNIP3L (Homodimer)
BNIP3L (Monomer)
BNIP3
p62
NBR1
ATG12 - ATG5
ATG7
pro-SP C
GAPDH
70
40
35
25
70
100
55
70
25
35
B.
IDV % of GAPDH
ns
AD
Veh
Bnip3L- Homodimer
C.
IDV % of GAPDH
ns
AD
Veh
BNIP3L- Monomer
D.
IDV % of GAPDH
ns
AD
Veh
Bnip3
E.
IDV % of GAPDH
*
AD
Veh
p62
F.
IDV % of GAPDH
ns
AD
Veh
NBR1
G.
IDV % of GAPDH
**
AD
Veh
ATG12-ATG5

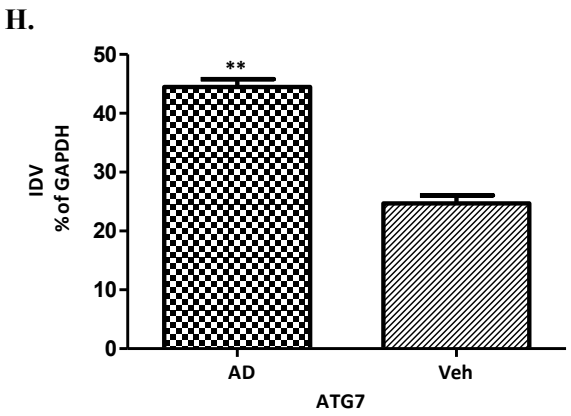

Figure 4.8. Differential expression of mitophagy proteins in AD treated AECII.
(A) Representative western blot images for Bnip3L (homodimer & monomer), Bnip3, p62, NBR1, ATG12-ATG5, ATG7, proSP-C and GAPDH (loading control) from 24 hours of AD or Veh treated AECII isolated from C57Bl/6 mice. n = 3 independent experiments. (B, C, D, E, F, G and H) Densitometry analysis of the triplicate blots of the target proteins *viz* Bnip3L (homodimer & monomer), Bnip3, p62, NBR1, ATG12-ATG5, ATG7 and GAPDH (loading control) and target protein*100/GAPDH ratio was calculated and represented as bar graphs. **p < 0.01,*p < 0.05, ns - no significance.

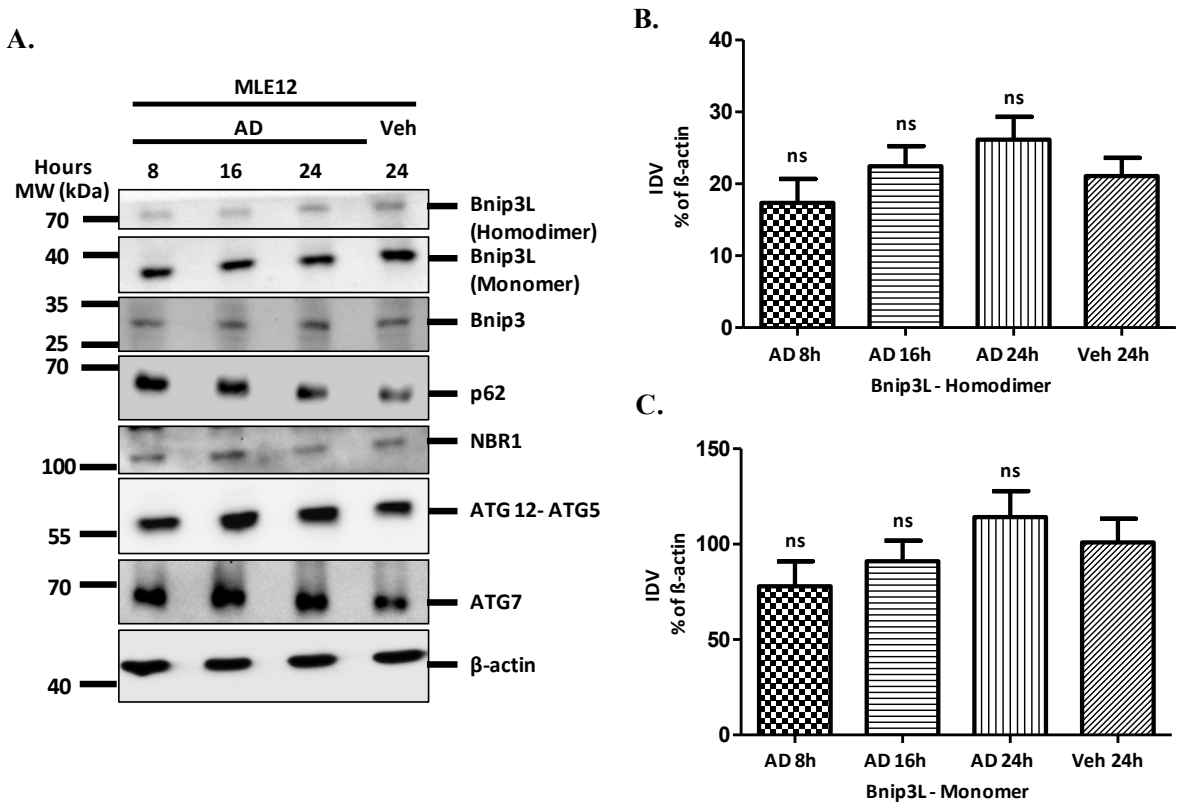

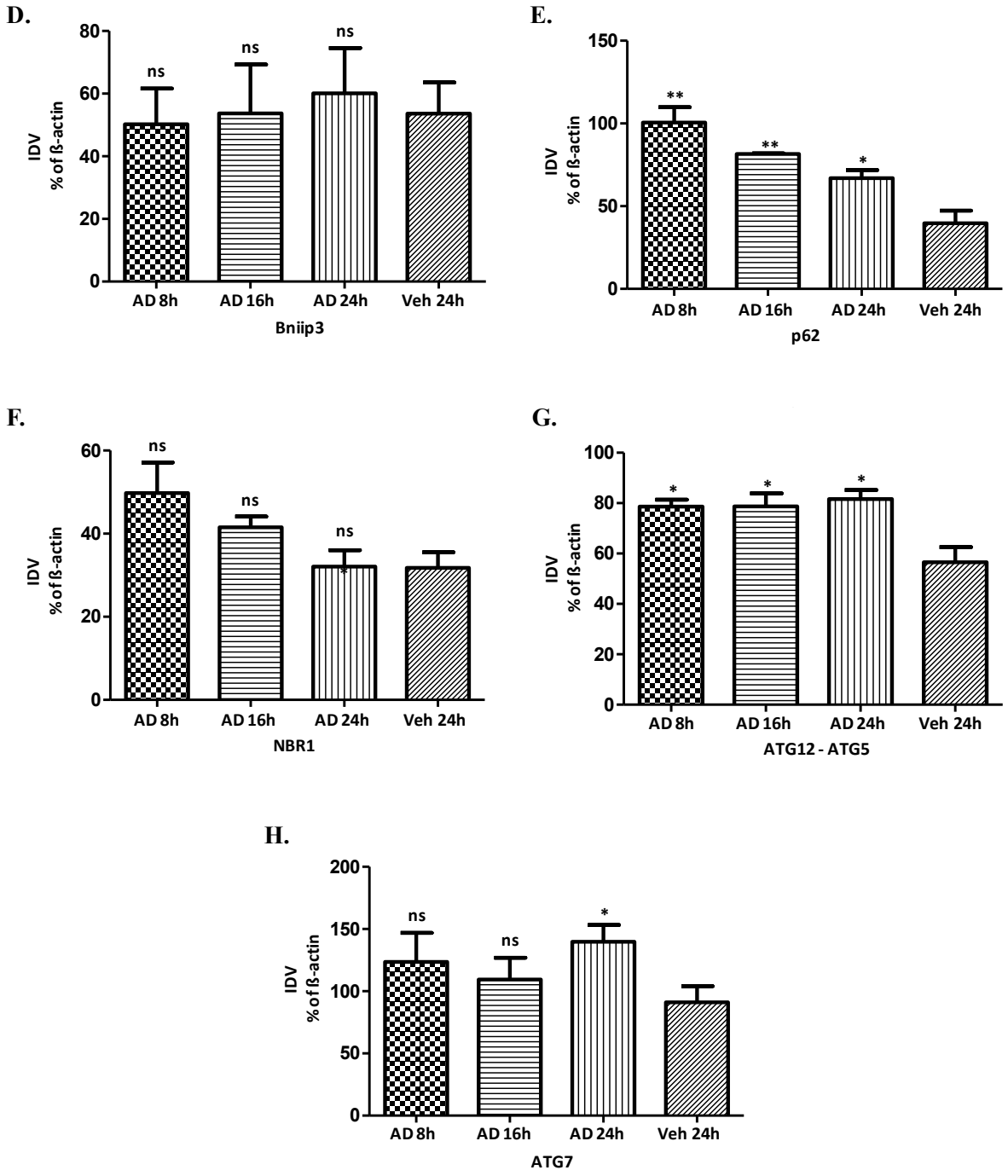

Figure 4.9. Differential expression of mitophagy proteins in AD treated MLE12 cells.
(A) Representative western blot images for Bnip3L (homodimer & monomer), Bnip3, p62, NBR1, ATG12-ATG5, ATG7, proSP-C and β-actin (loading control) from AD (8, 16 and 24 hours) and Veh (24 hours) treated MLE12 cells. n = 3 independent experiments. (B, C, D, E, F, G and H) Densitometry analysis of the triplicate blots of the target proteins *viz* Bnip3L (homodimer & monomer), Bnip3, p62, NBR1, ATG12-ATG5, ATG7 and β-actin (loading control) and target protein*100/β-actin ratio was calculated and represented as bar graphs. **p < 0.01,*p < 0.05, ns - no significance.

4.3.4. AD initiates mitophagy *via* lysine 63-linked ubiquitin chains and p62 in murine AECII

The selective autophagy protein p62 plays a key role in aggregating dysfunctional mitochondria and delivering it for autophagic degradation (Geisler *et al.,* 2010). In an attempt to figure out if AD-induced p62 accumulation promotes mitophagy, immunofluorescence (IF) analysis of p62 was performed in AD versus Veh treated murine AECII (24 hours) and MLE12 cells (8 hours). Since the ubiquitin associated (UBA) domain of p62 exhibits exclusively strong binding affinity towards K63-linked ubiquitin chains (ubiquitin.K63) and the Phox and Bem 1 (PB1) domain of p62 boosts interaction with NBR1 (Johansen and Lamark, 2011; Kirkin *et al.,* 2009), the expression and distribution pattern of NBR1 and ubiquitin.K63 were also analyzed.

A.

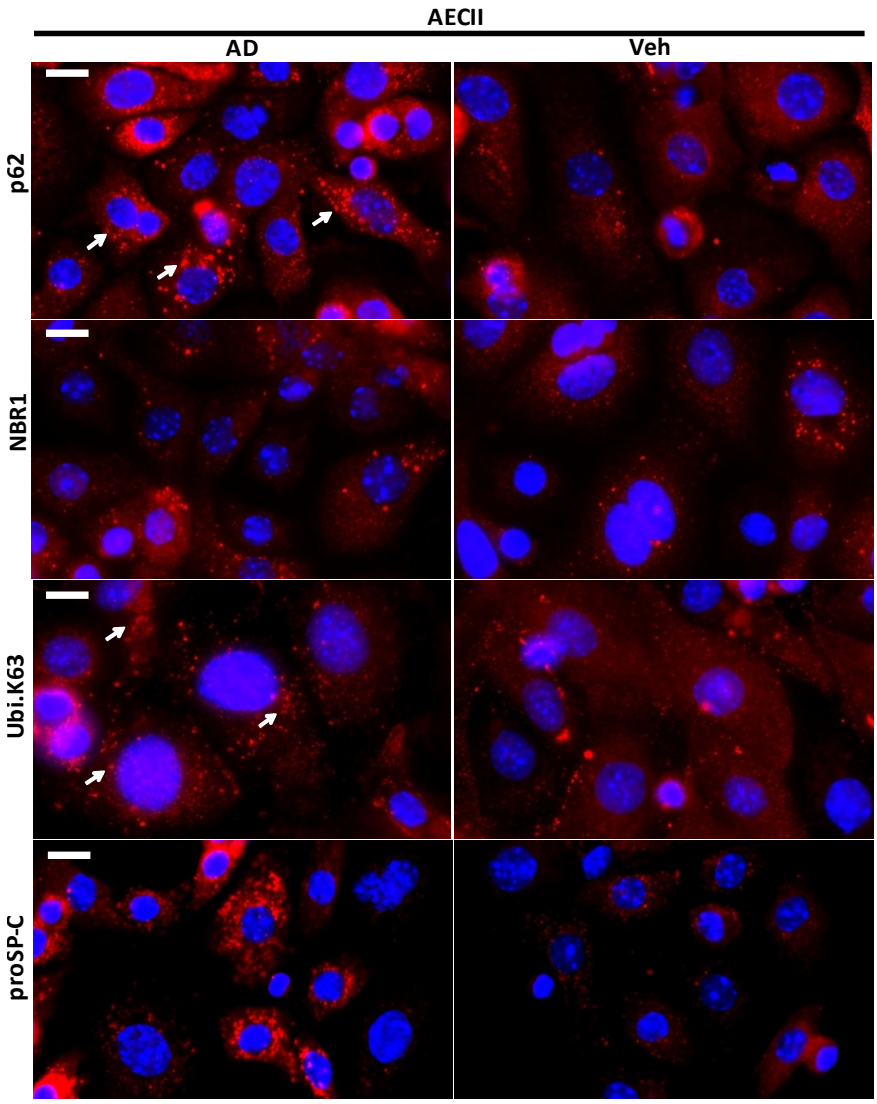

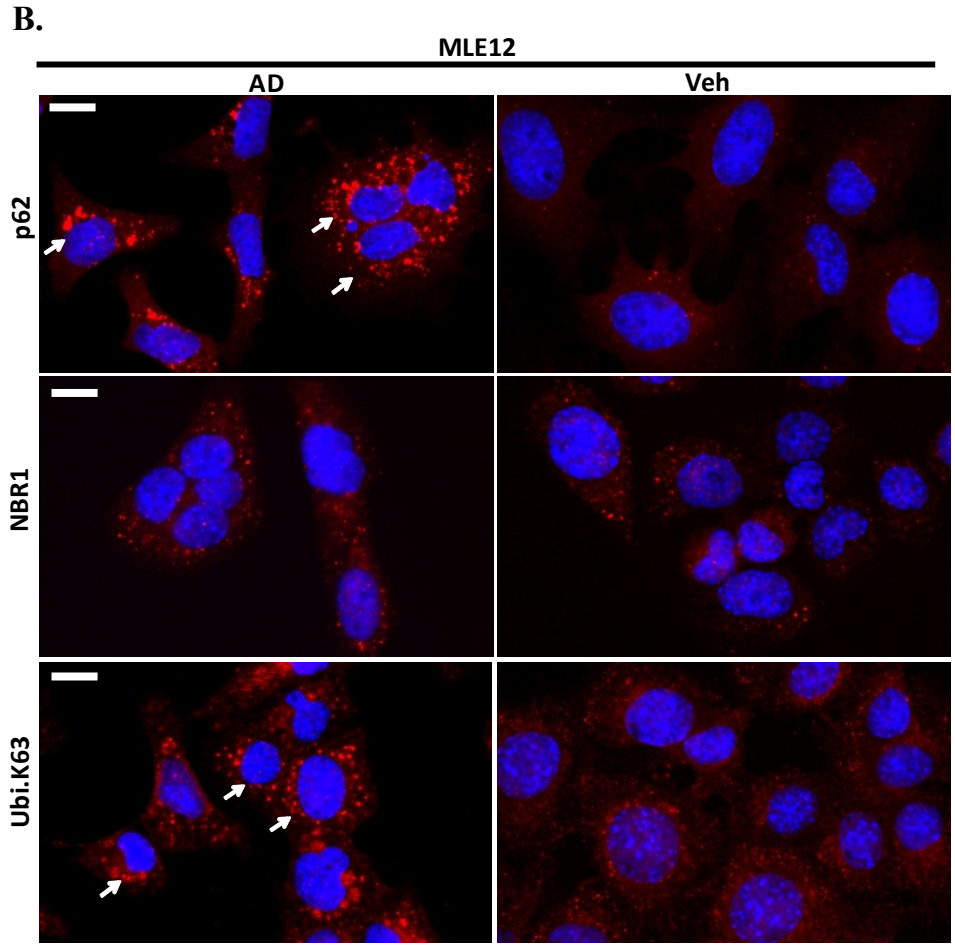

Figure 4.10. Selective autophagy proteins *viz* p62, NBR1 and ubiquitin.K63 in AD treated AECII and MLE12 cells.
(A) Immunofluorescence analysis of 24 hours of AD or Veh treated murine AECII for p62 (red), NBR1 (red) ubiquitin.K63 (red) and proSP-C (red) (AECII marker). Nuclei are stained with DAPI (blue). Arrows indicate cells showing increased expression of respective protein under AD treatment. n = 3 independent experiments. Scale bar = 10 µm. (B) Immunofluorescence analysis of 8 hours of AD or Veh treated MLE12 cells for p62 (red), NBR1 (red) and ubiquitin.K63 (red). Nuclei are stained with DAPI (blue). Arrows indicate cells showing perinuclear clustering of the respective protein under AD treatment. n = 3 independent experiments. Scale bar = 10 µm.

Immunofluorescence analysis of AD treated murine AECII and MLE12 cells *in vitro* revealed strong punctate staining of p62 and ubiquitin.K63 (in spite of the ubiquitin.K63 antibody staining the background in AECII) in comparison to a very faint diffused staining observed among the Veh treated controls (Figure 4.10A). Additionally, MLE12 cells displayed increased perinuclear clustering of p62 and ubiquitin.K63 under AD treatment (Figure 4.10). In accordance with the observation of unaltered expression of NBR1 in the western blot analysis of AD treated AECII and MLE12 cell lysates (Figures 4.8A and 4.9A), no observable differences in expression were visualized between the AD and Veh treated AECII and MLE12 cells as shown in figures 4.10A and B. Both AD and Veh treated cell types mostly displayed a punctate staining for NBR1.

In order to identify if p62, NBR1 or ubiquitin.K63 are targeted to the autophagosomes under AD treatment, MLE12 cells were transfected with GFP-LC3B plasmid overnight, followed by treatment with AD or Veh for 8 hours. Co-immunofluorescence analysis was then performed using antibodies against p62, NBR1 or ubiquitin.K63. AD treatment of the GFP-LC3B transfected MLE12 cells resulted in the characteristic GFP-LC3B puncta and they were found encircling the AD-induced vacuoles in contrast to the diffused staining observed among the Veh treated cells. Co-immunofluorescence analysis displayed increased co-localization of GFP-LC3B with p62 under AD treatment as compared to the vehicle treated cells (Figure 4.11A). In Veh treated cells, co-localization between GFP-LC3 and p62 was observed, albeit at lower levels as p62 is destined to undergo autophagy under normal conditions. In full support, primary AECII treated with AD for 24 hours *in vitro* also exhibited significant co-localization of LC3B and p62 (Figure 4.11B).

A.

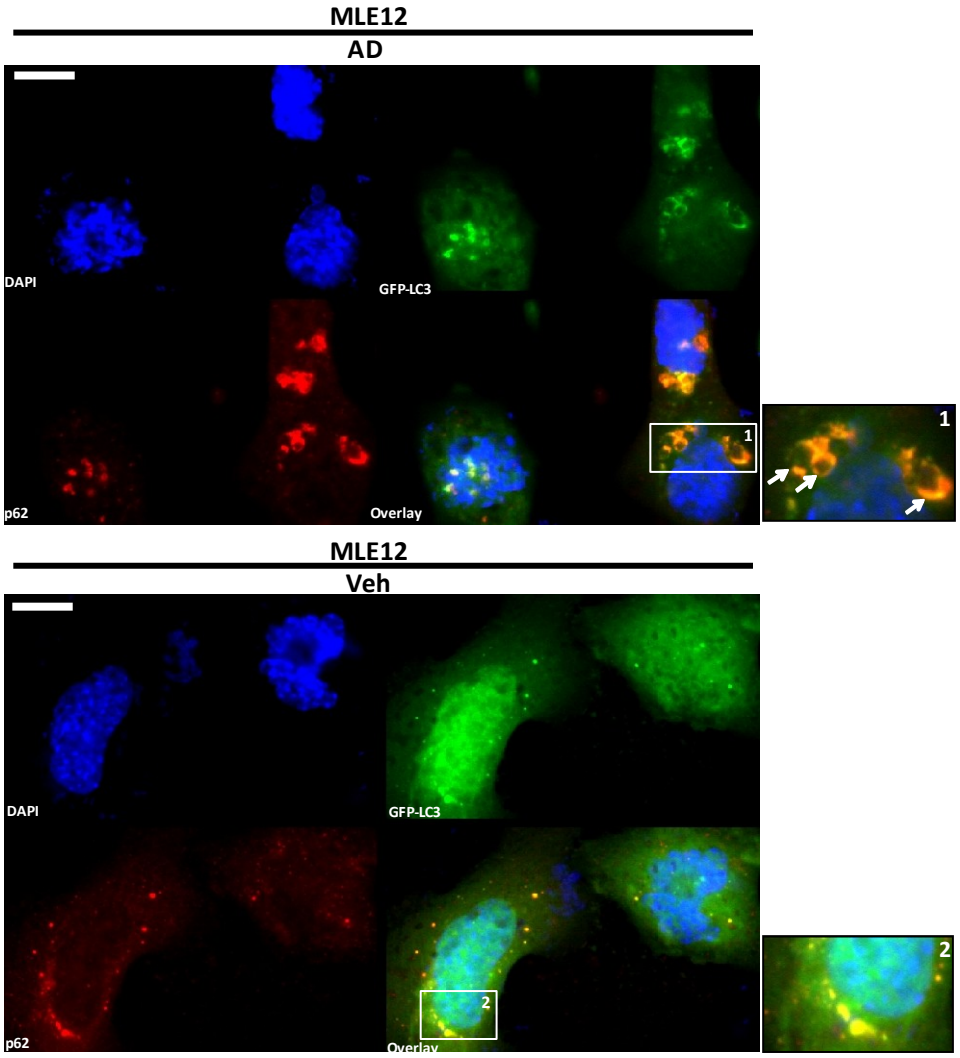

B.

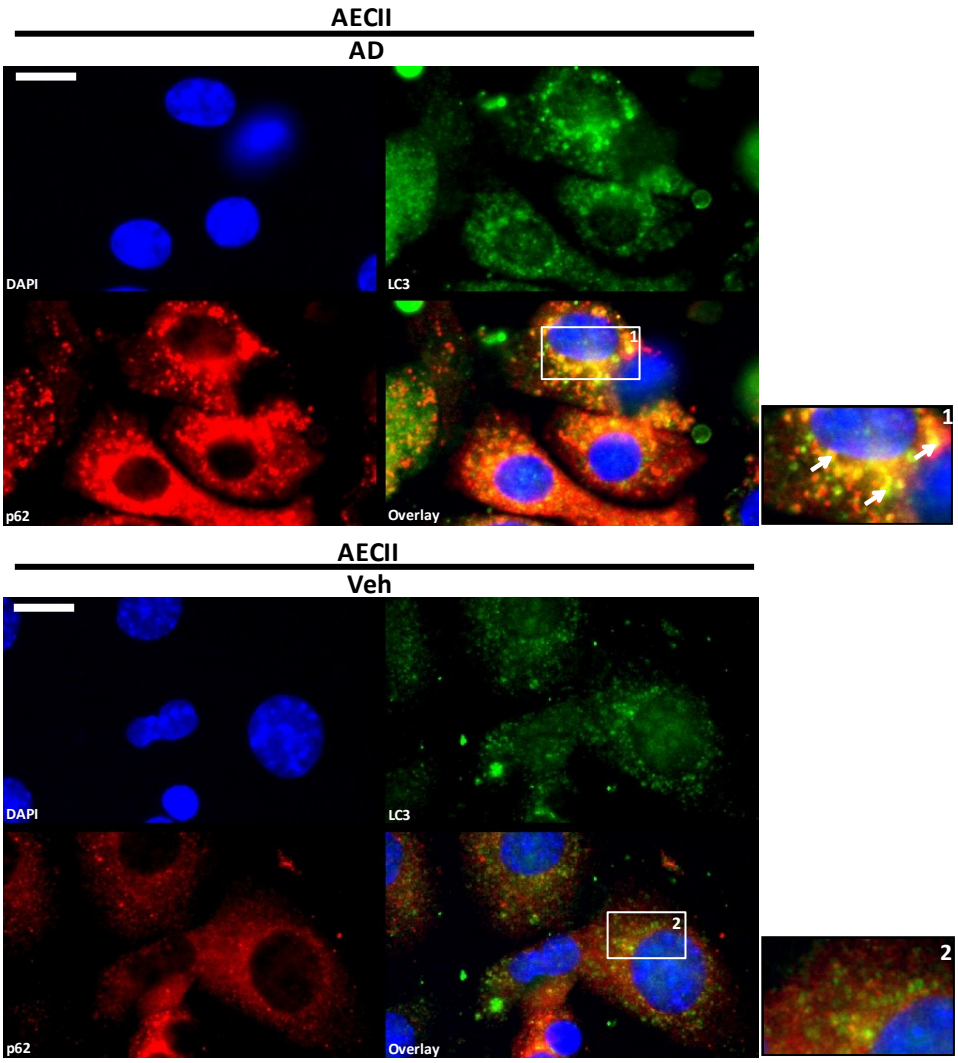
AECII
AD
DAPI
LC3
p62
Overlay
1
1
AECII
Veh
DAPI
LC3
p62
Overlay
2
2

C.

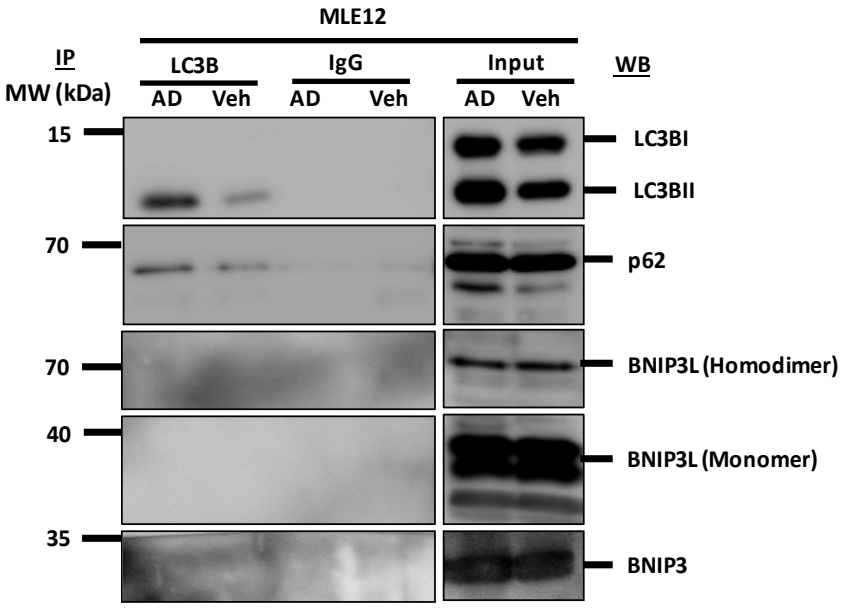
MLE12
IP
MW (kDa)
LC3B
IgG
Input
WB
AD
Veh
AD
Veh
AD
Veh
15
70
70
40
35
LC3BI
LC3BII
p62
BNIP3L (Homodimer)
BNIP3L (Monomer)
BNIP3

D.

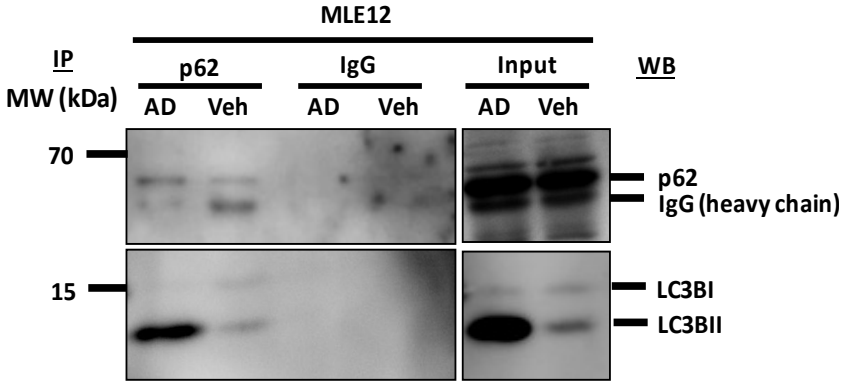
MLE12
IP
MW (kDa)
p62
IgG
Input
WB
AD
Veh
AD
Veh
AD
Veh
70
15
p62
IgG (heavy chain)
LC3BI
LC3BII

E.

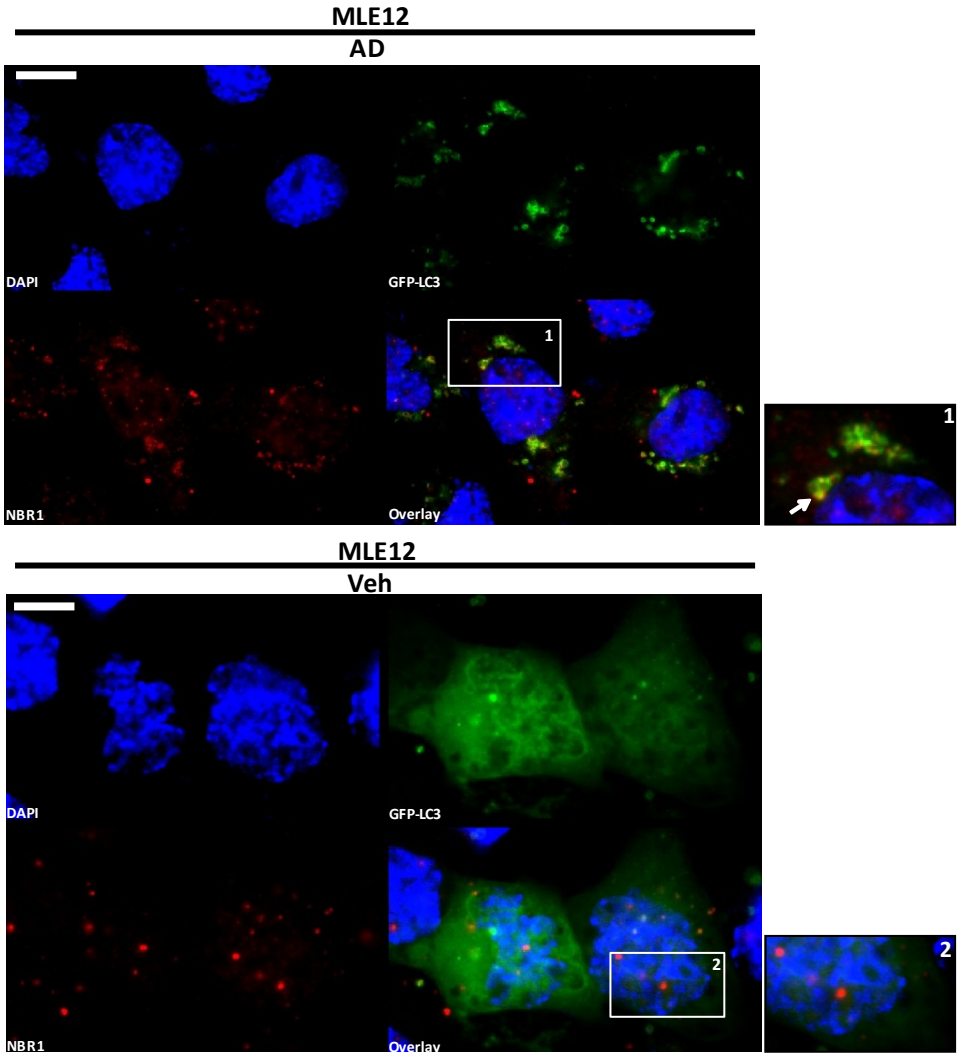
MLE12
AD
DAPI
GFP-LC3
NBR1
Overlay
1
1
MLE12
Veh
DAPI
GFP-LC3
NBR1
Overlay
2
2

F.

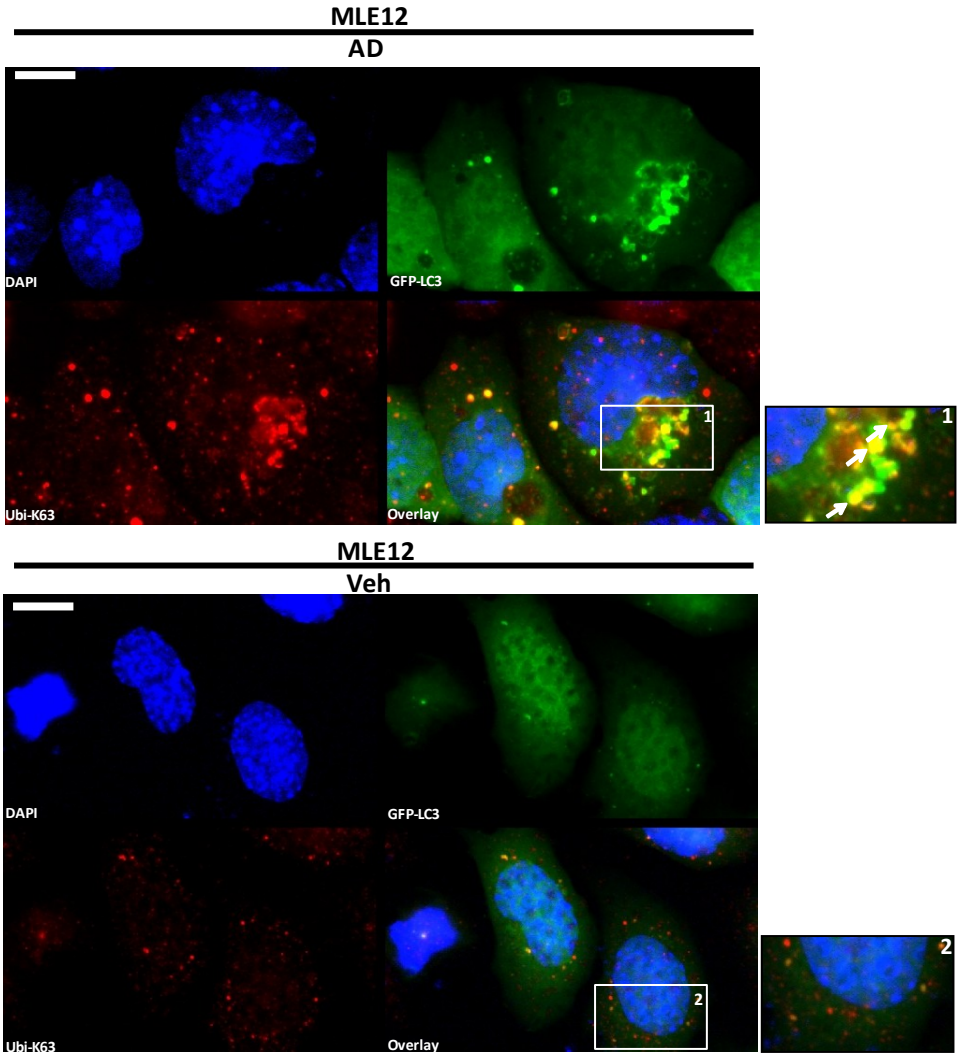

Figure 4.11. Targeting of ubiquitin.K63 and p62 to the autophagosomes in AD treated AECs.
(A) Co-immunofluorescence analysis of 8 hours of AD or Veh treated GFP-LC3B (green) transfected MLE12 cells for p62 (red). Nuclei are stained with DAPI (blue). Arrows indicate the co-localization (yellow) of p62 with GFP-LC3B under AD treatment. n = 3 independent experiments. Scale bar = 10 µm. (B) Co-immunofluorescence analysis of 24 hours of AD or Veh treated murine AECII for LC3B (green) and p62 (red). Nuclei are stained with DAPI (blue). Arrows indicate the co-localization (yellow) of LC3B with p62 under AD treatment. n = 3 independent experiments. Scale bar = 10 µm. (C) Western blot images for LC3B, p62, Bnip3L (homodimer and Monomer) and Bnip3 from 8 hours of AD or Veh treated MLE12 cells' lysates immunoprecipitated with LC3B or Immunoglobulin G (IgG) antibodies. (D) Western blot images for p62 and LC3B from 8 hours of AD or Veh treated MLE12 cells' lysates immunoprecipitated with p62 or Immunoglobulin G (IgG) antibodies. (E) Co-immunofluorescence analysis of 8 hours of AD or Veh treated GFP-LC3B (green) transfected MLE12 cells for NBR1 (red). Nuclei are stained with DAPI (blue). n = 3 technical replicates. Scale bar = 10 µm. (F) Co-immunofluorescence analysis of 8 hours of AD or Veh treated GFP-LC3B (green) transfected MLE12 cells for ubiquitin.K63 (red). Nuclei are stained with DAPI (blue). Arrows indicate the co-localization (yellow) of ubiquitin.K63 with GFP-LC3B (yellow) under AD treatment. n = 3 independent experiments. Scale bar = 10 µm.

In addition, co-immunoprecipitation analysis revealed significant pull down of p62 with LC3B antibody in the AD treated MLE12 cells and *vice versa* (Figure 4.11C and D). Interestingly, co-immunoprecipitation experiments with LC3B antibody did not pull down Bnip3L or Bnip3

upon AD treatment in spite of higher concentration of the respective proteins being present in the input (Figure 4.11C). This re-emphasizes the strong interaction between p62 and LC3B under AD treatment. In case of NBR1, a fraction of NBR1 protein was found to be very weakly co-localizing with GFP-LC3B in the AD treated MLE12 cells (Figure 4.11E), whereas a prominent co-localization was observed between GFP-LC3B and ubiquitin.K63 in MLE12 cells upon AD treatment that was not observed in Veh treated GFP-LC3B transfected MLE12 cells (Figure 4.11F). Therefore, these experiments confirm that AD-induced ubiquitin.K63 and p62 are targeted to autophagosomes.

In our further attempts to analyze if the damaged mitochondria are targeted to autophagosomes under conditions of AD treatment, we performed immunofluorescence analysis for COXIV in GFP-LC3B transfected AD treated MLE12 cells and asked if COXIV co-localizes with GFP-LC3B. Interestingly, we observed a prominent increase in co-localization signals for COX IV with GFP-LC3B compared to that of the Veh treated controls (Figure 4.12A). This to us indicated that AD treatment targets mitochondria to the autophagosomes. This further led to the speculation that AD-induced dysfunctional mitochondria are probably targeted to the autophagosomes *via* p62. In order to test this, we isolated cytoplasmic and mitochondrial-lysosomal (ML) subcellular fractions from 8 hours of AD or Veh treated MLE12 cells using the protocol adapted from Muquit *et al.,* (Muqit *et al.,* 2006) and examined for the presence of p62, LC3B I and II, Bnip3L and Bnip3.

A.

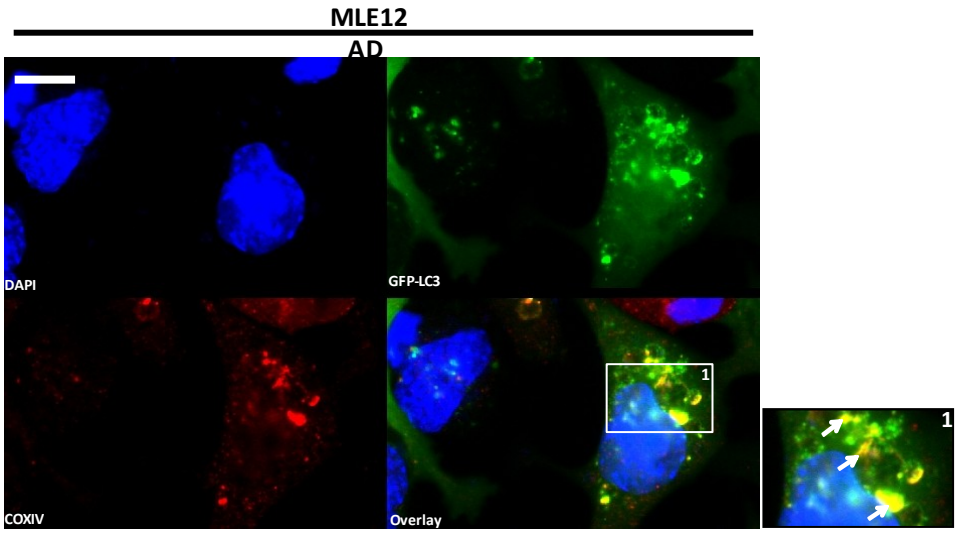

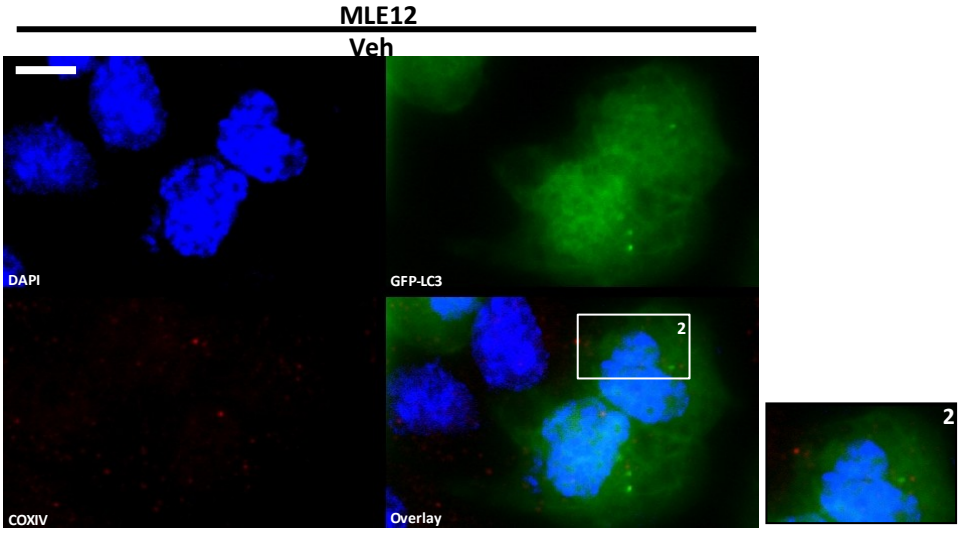

B.

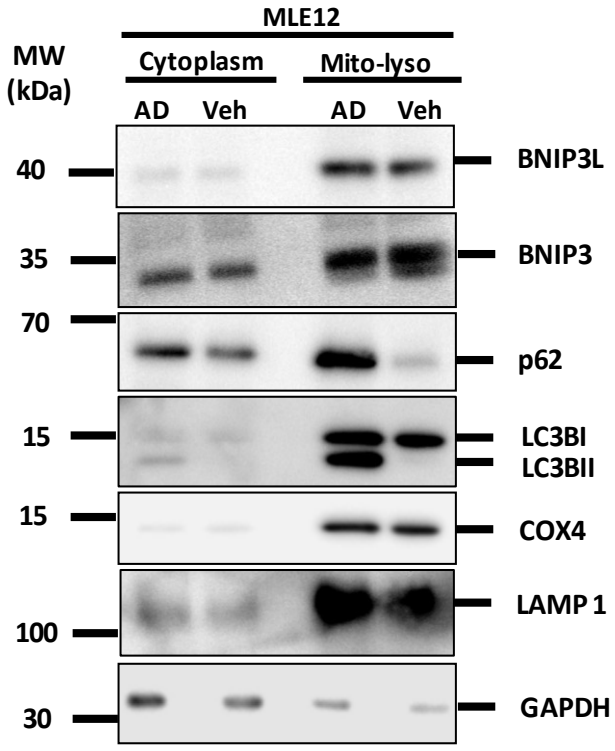

Figure 4.12. Mitochondria are targeted to the autophagosomes via p62 in AD treated MLE12 cells.
(A) Co-immunofluorescence analysis of 8 hours of AD or Veh treated GFP-LC3B (green) transfected MLE12 cells for COX IV (red). Nuclei are stained with DAPI (blue). Arrows indicate the co-localization (yellow) of COX IV with GFP-LC3B under AD treatment. n = 3 independent experiments. Scale bar = 10 µm. (B) Representative western blot images for Bnip3L (Monomer), Bnip3, p62, LC3B, COX IV (Mitochondrial marker), LAMP1 (Lysosomal marker) and GAPDH (cytoplasmic marker) of the cytoplasmic and mitochondrial-lysosomal (Mito-lyso) fractions from 8 hours of AD or Veh treated MLE12 cells. n = 3 technical replicates.

In coherence with our previous results, p62 and LC3BII were found to be significantly increased in the mitochondrial-lysosomal fraction of AD treated MLE12 cells, while Bnip3L and Bnip3 remained (Figure 4.12B). Hence, from these results we concluded that p62 plays a pivotal role in targeting dysfunctional mitochondria to the autophagosomes upon AD treatment.

4.3.5. Mitochondria entrapped autophagosomes are targeted to lysosomes in AD treated murine AECII *in vitro*.

To further verify whether ubiquitin.K63 and p62 tagged mitochondria trapped within the autophagosomes are targeted to the lysosomes, co-immunofluorescence analysis of p62, NBR1, ubiquitin.K63 and COX IV were performed with the lysosomal marker, lysosomal-associated membrane protein 1 (LAMP-1) after 8 hours of AD or Veh treatment of MLE12 cells. This analysis revealed prominent and increased co-localization of p62, ubiquitin.K63 and COX IV with LAMP-1 at many foci in the AD treated MLE12 cells, a finding that was not observed among the Veh treated controls (Figures 4.13A, D and E). Similar to our previous observations very few NBR1 proteins were found to be localized along the margins of LAMP-1 positive staining in the MLE12 cells following AD treatment (Figure 4.13C). Co-localization of p62 and COX IV with another lysosomal marker, cathepsin D was examined in 24 hours of AD, Veh treated murine AECII *in vitro*, to reconfirm their targeting to the lysosomes. Like the MLE12 cells, AD treated primary AECII also exhibited significantly increased co-localization of p62 and COX IV with cathepsin D (Figures 4.13B and F).

A.

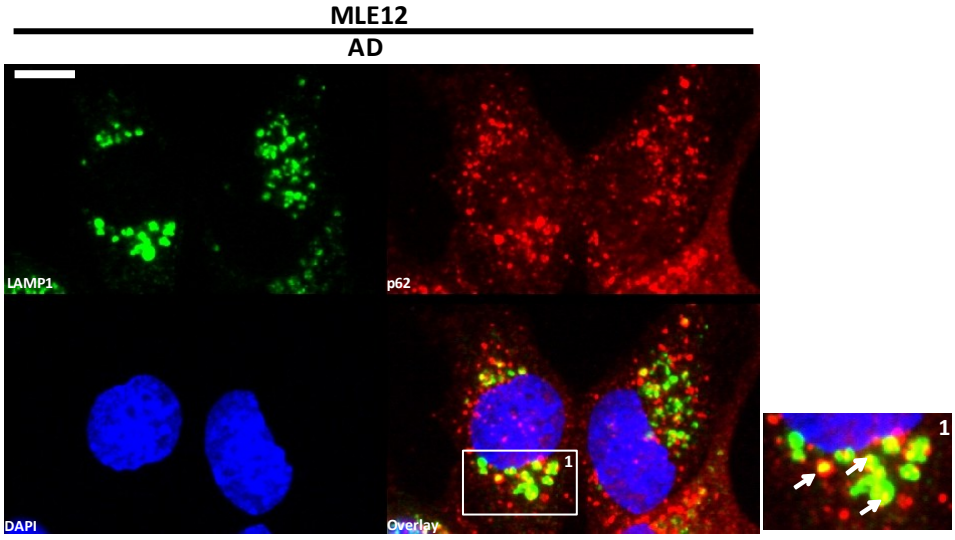

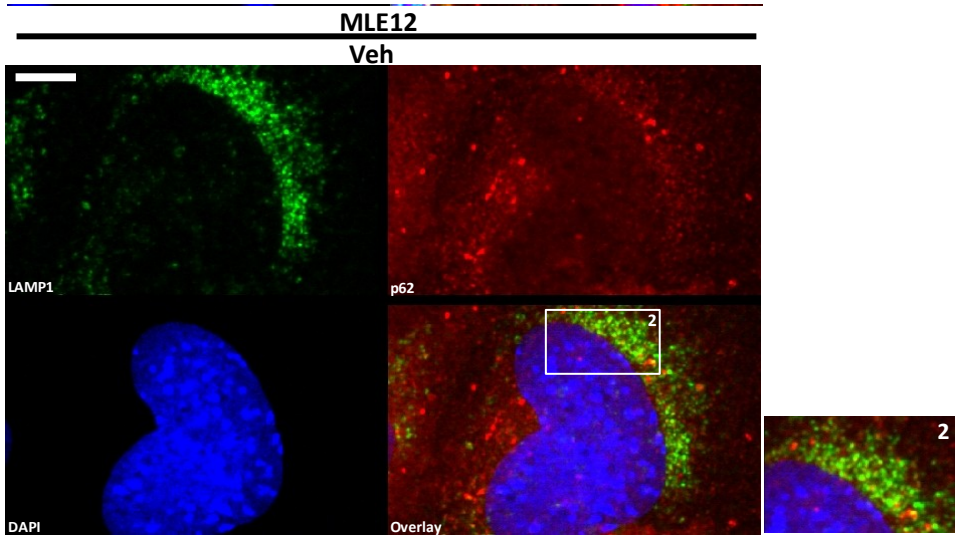
MLE12
Veh
LAMP1
p62
DAPI
Overlay
2
2

B.

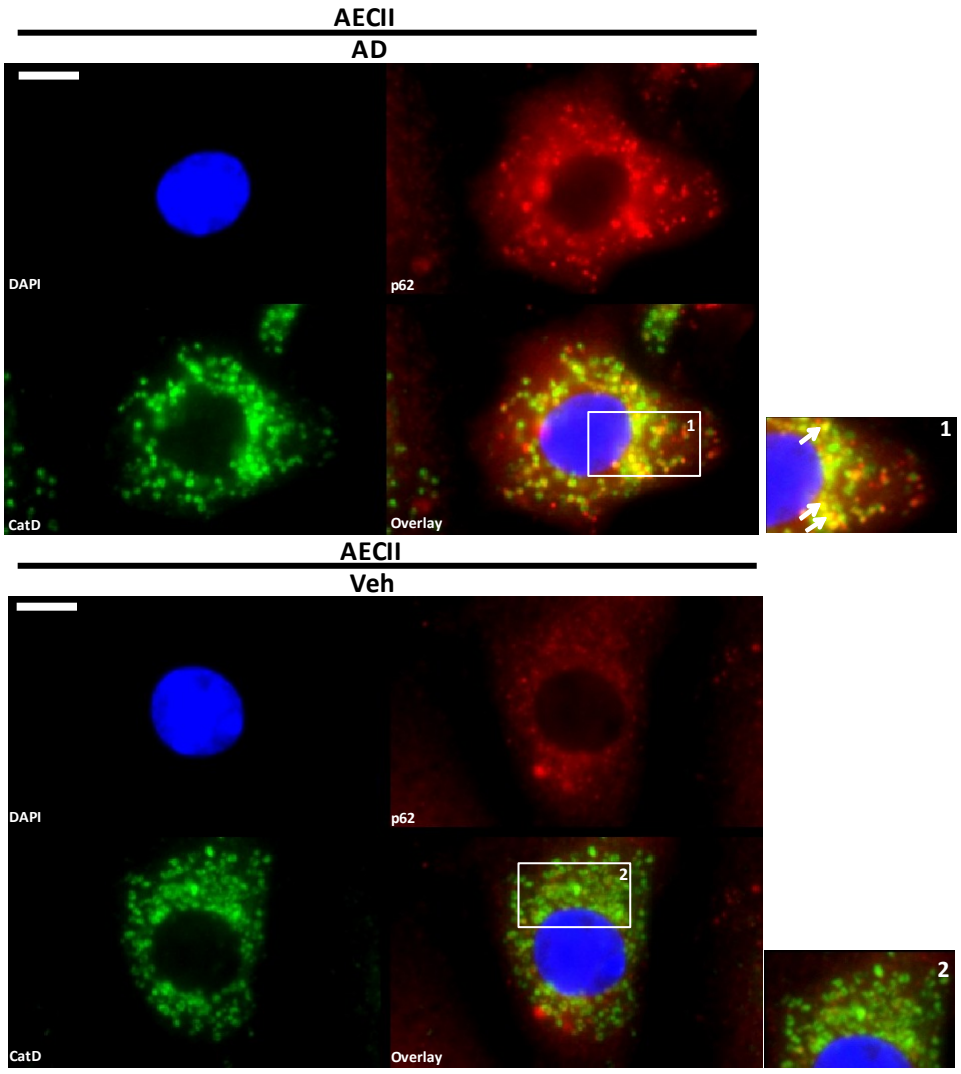
AECII
AD
DAPI
p62
CatD
Overlay
1
1
AECII
Veh
DAPI
p62
CatD
Overlay
2
2

C.

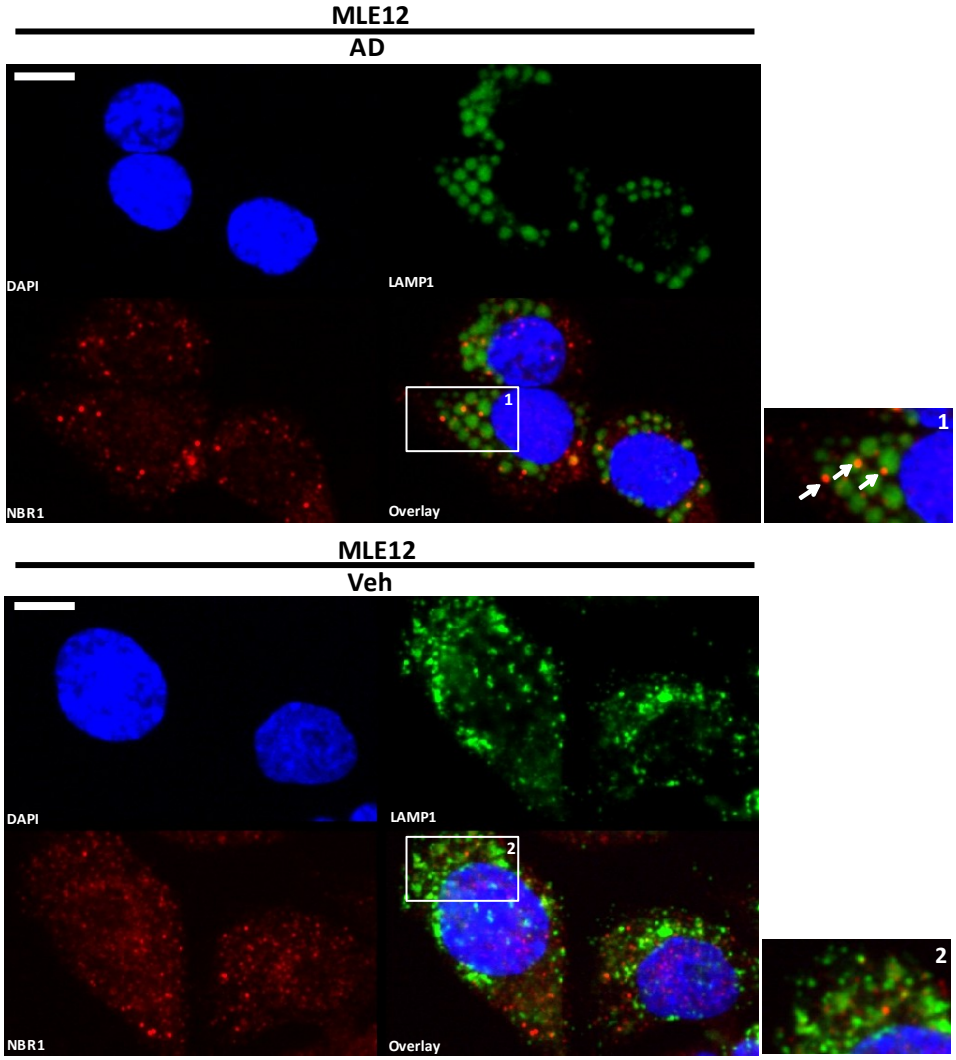
MLE12
AD
DAPI
LAMP1
NBR1
Overlay
1
MLE12
Veh
DAPI
LAMP1
NBR1
Overlay
2

D.

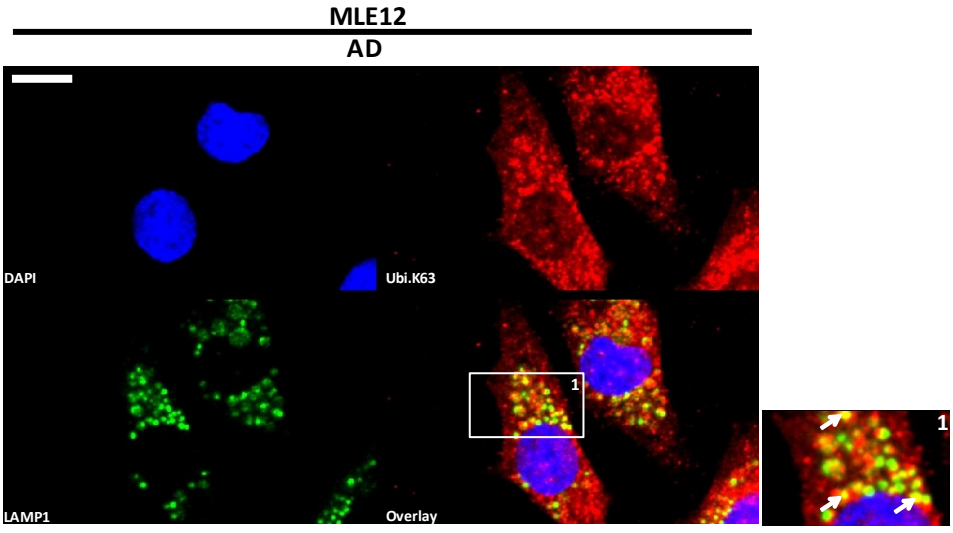
MLE12
AD
DAPI
Ubi.K63
LAMP1
Overlay
1

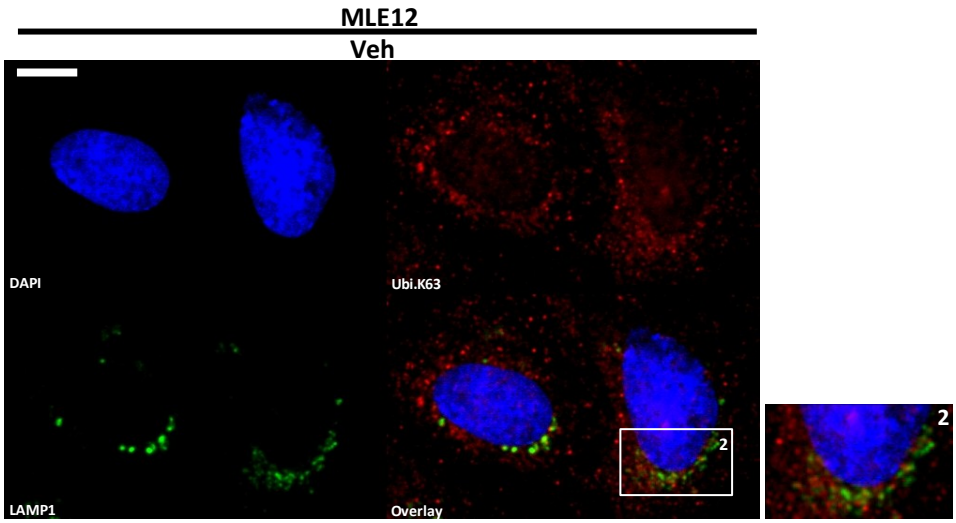
MLE12
Veh
DAPI
Ubi.K63
LAMP1
Overlay
2
2

E.

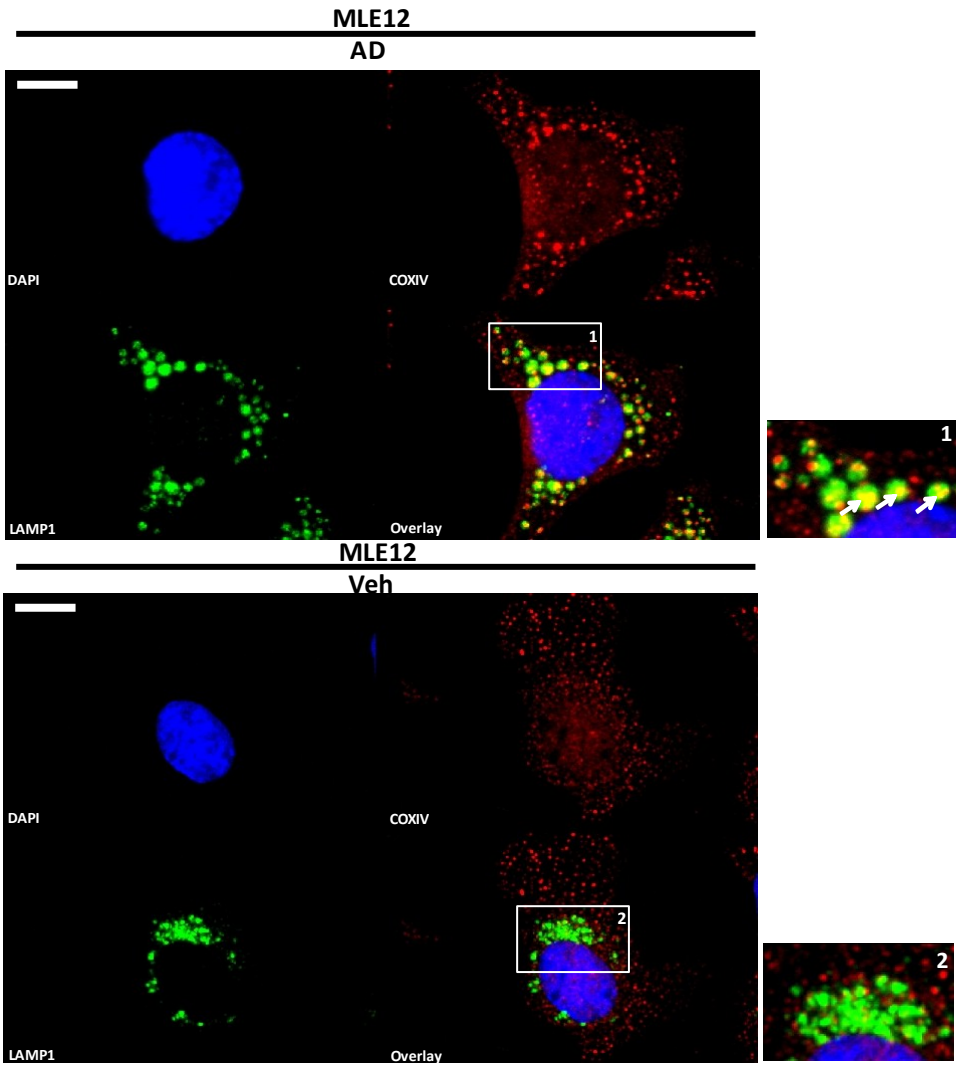
MLE12
AD
DAPI
COXIV
LAMP1
Overlay
1
1
MLE12
Veh
DAPI
COXIV
LAMP1
Overlay
2
2

F.

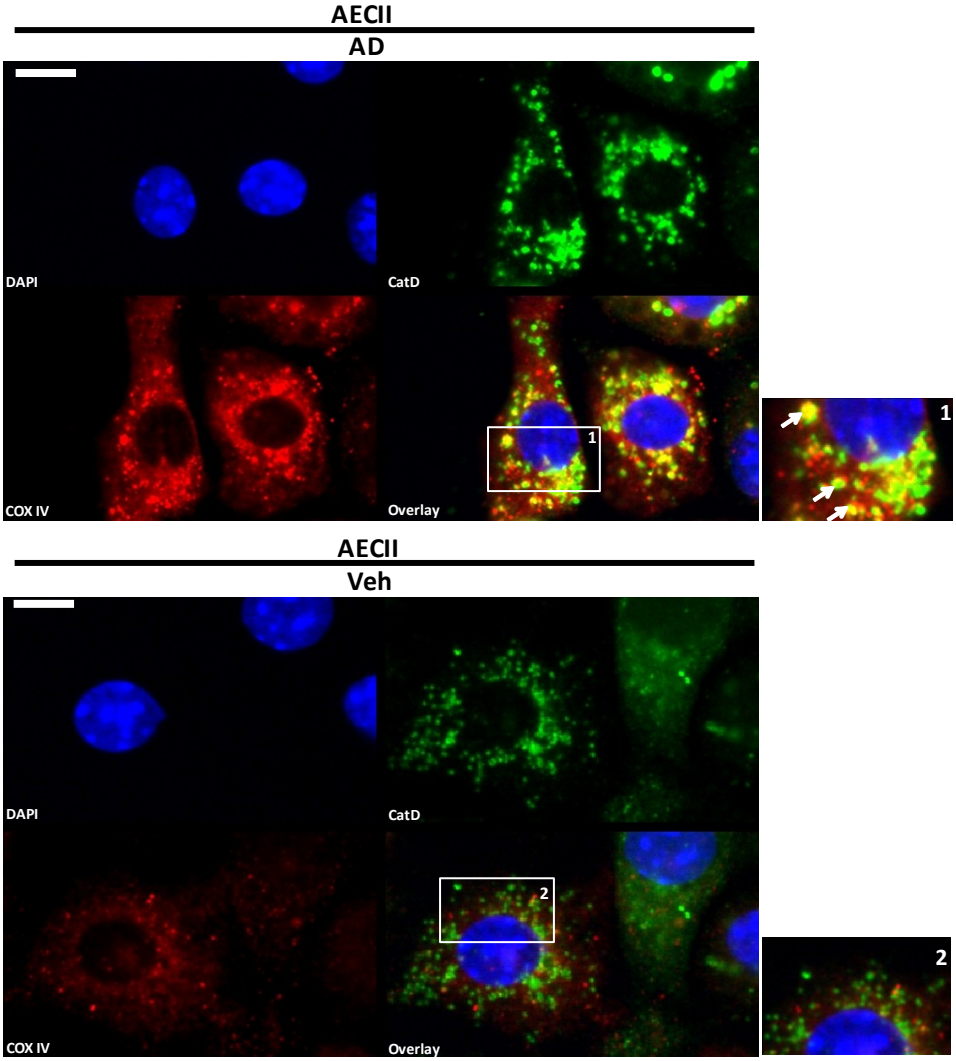

Figure 4.13. Mitochondria entrapped autophagosomes are targeted to lysosomes in AD treated murine AECII *in vitro*.
(A) Co-immunofluorescence analysis of 8 hours of AD or Veh treated MLE12 cells for LAMP-1 (green) and p62 (red). Nuclei are stained with DAPI (blue). Arrows indicate the co-localization (yellow) of p62 with LAMP-1 under AD treatment. n = 3 independent experiments. Scale bar = 10 µm. (B) Co-immunofluorescence analysis of 24 hours of AD or Veh treated murine AECII for cathepsin D (Cat D) (green) and p62 (red). Nuclei are stained with DAPI (blue). Arrows indicate the co-localization (yellow) of Cat D with p62 under AD treatment. n = 3 independent experiments. Scale bar = 10 µm. (C) Co-immunofluorescence analysis of 8 hours of AD or Veh treated MLE12 cells for LAMP-1 (green) and NBR1 (red). Nuclei are stained with DAPI (blue). n = 3 independent experiments. Scale bar = 10 µm. (D) Co-immunofluorescence analysis of 8 hours of AD or Veh treated MLE12 cells for LAMP-1 (green) and ubiquitin.K63 (red). Nuclei are stained with DAPI (blue). Arrows indicate the co-localization (yellow) of ubiquitin.K63 with LAMP-1 under AD treatment. n = 3 independent experiments. Scale bar = 10 µm. (E) Co-immunofluorescence analysis of 8 hours of AD or Veh treated MLE12 cells for LAMP-1 (green) and COX IV (red). Nuclei are stained with DAPI (blue). Arrows indicate the co-localization (yellow) of COX IV with LAMP-1 under AD treatment. n = 3 independent experiments. Scale bar = 10 µm. (D) Co-immunofluorescence analysis of 24 hours of AD or Veh treated murine AECII for cathepsin D (Cat D) (green) and COX IV (red). Nuclei are stained with DAPI (blue). Arrows indicate the co-localization (yellow) of Cat D with COX IV under AD treatment. n = 3 independent experiments. Scale bar = 10 µm.

Therefore, results of these analyses validate our hypothesis that mitochondria that are trapped within the autophagosomes are targeted to lysosomes following AD treatment.

4.3.6. Inhibition of AD-induced mitophagy or oxidative stress alters LC3B lipidation in murine AECII *in vitro*

In order to further decipher the role of mitophagy and oxidative stress in driving AD-induced autophagy, we exploited the use of mdivi-1, a mitochondrial division inhibitor and N-acetyl-L-cysteine (NAC), an antioxidant. Mdivi-1 is a pharmacological inhibitor that prevents mitochondrial fission by inhibiting Drp-1 (Mizumura *et al.,* 2014). Division of the damaged mitochondria from its healthy counterpart is a pre-requisite for initiation of mitophagy (Ding and Yin, 2012), hence prevention of fission prevents mitophagy. Co-treatment of MLE12 cells with AD and mdivi-1 (20 µM) for 4 hours displayed proficient downregulation in the lipidation of LC3B, i.e. less LC3BII synthesis and a prominent decrease in annexin V staining was observed in MLE12 cells under AD + mdivi-1 treatment (Figures 4.15A, B and C). Thus, the prevention of AD driven mitophagy inhibits apoptosis. A significant downregulation in LC3B lipidation was noted in MLE12 cells co-treated with AD and NAC (2 mM) for 4 hours, too. (Figures 4.15 D, and E) Similarly, a drastic reduction in LC3BII were observed in murine AECII co-treated with AD and NAC (2 mM) for 24 hours (Figures 4.15 F and G). It is already known that the LC3B knockdown under AD treatment also prevents apoptosis of AECII (Figures 4.2A and D). Taken together, these observations suggest prevention of either AD driven aberrant mitophagy or oxidative stress drastically reduces LC3B lipidation and apoptosis.

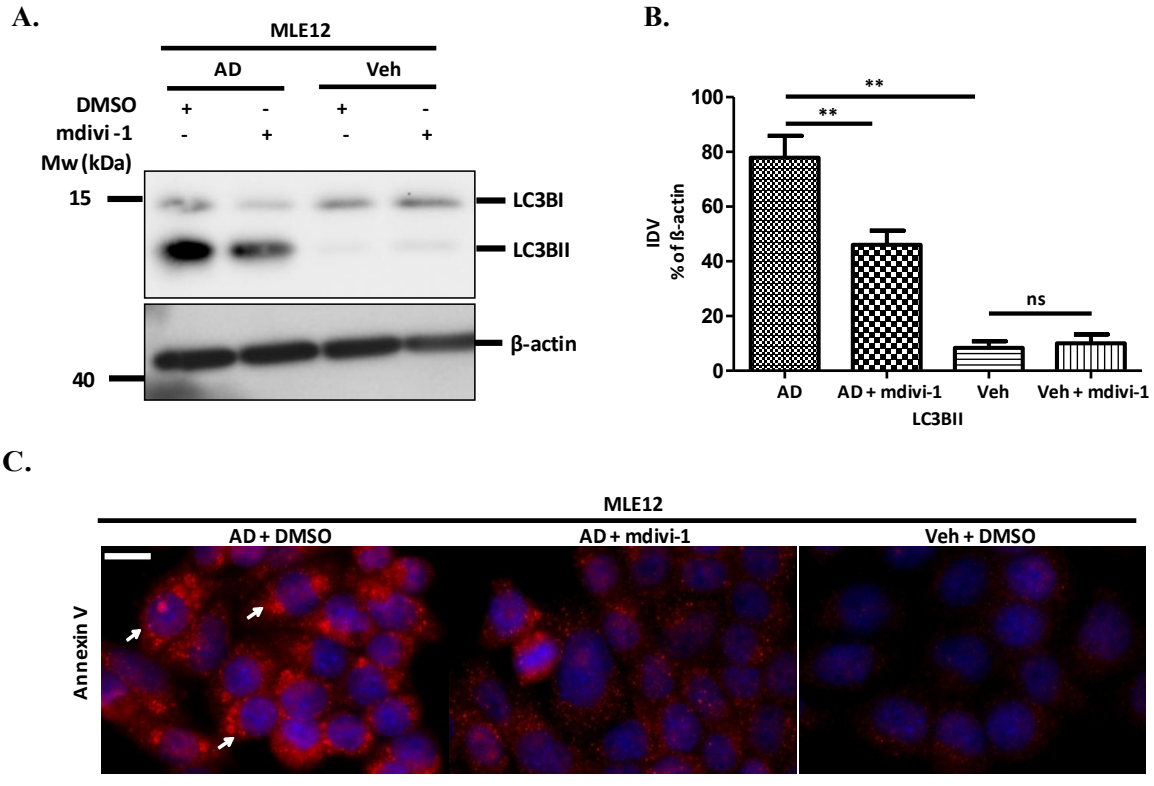

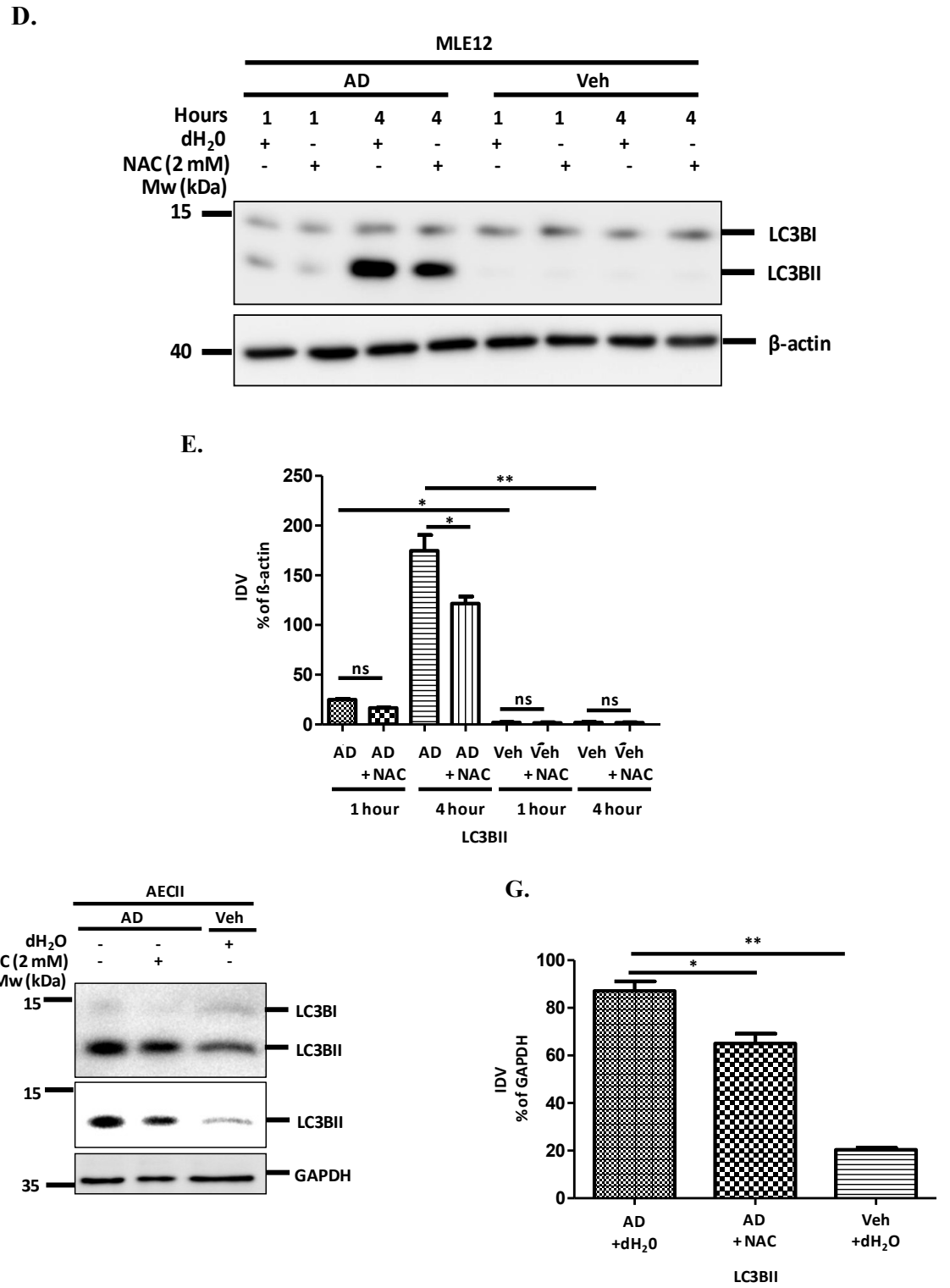

Figure 4.14. Reduced LC3B lipidation in AD treated AECII upon mitophagy or oxidative stress inhibition.

(A) Representative western blot images for LC3B and β-actin (loading control) from 4 hours of mdivi-1 (20 μM) and AD or Veh co-treated MLE12 cells' lysates. n = 3 independent experiments. (B) Densitometry analysis of the triplicate blots of LC3BII and β-actin (loading control) and LC3BII*100/β-actin ratio was calculated and represented as a bar graph. **p < 0.01, ns - no significance. (C) Immunofluorescence analysis of 4 hours of AD + DMSO, AD + mdivi-1or Veh+Veh treated MLE12 cells for Annexin V (red). Nuclei are stained with DAPI (blue). Arrows indicate increased annexin V staining under AD treatment. Scale bar = 10 μm. (D) Representative western blot images for LC3B and β-actin (loading control) from 1 and 4 hours of NAC (2 mM) and AD or Veh co-treated MLE12 cells' lysates. n = 3 independent experiments. (E) Densitometry analysis of

the triplicate blots of LC3BII and β-actin (loading control) and LC3BII*100/β-actin ratio was calculated and represented as a bar graph. **p < 0.01, *p < 0.05, ns - no significance. (F) Representative western blot images for LC3B and GAPDH (loading control) from 24 hours of N-acetyl-L-Cysteine (NAC) (2 mM) and AD or Veh co-treated C57Bl/6 murine AECIIs' lysates. n = 3 technical replicates. (G) Densitometry analysis of the triplicate blots of LC3BII and GAPDH (loading control) and LC3BII*100/GAPDH ratio was calculated and represented as a bar graph. **p < 0.01, *p < 0.05.

4.4. Anti-oxidative response in murine model of AD-induced pulmonary fibrosis

4.4.1. AD induces HO-1 production in response to increased oxidative stress in AD treated murine AECII

It is evident from the current (Figure 4.5) and previous studies (Nicolescu *et al.,* 2008, Bolt *et al.,* 2001) that AD drastically increases oxidative stress. In order to analyze the counteracting anti-oxidative response under AD treatment conditions, the expression of a major antioxidant protein, Heme oxygenase-1 (HO-1) was analyzed. Western blot analysis of the lung homogenates of day 7, 14, 21 and 28 of AD and day 28 of Veh treated C57/Bl6 mice revealed an increase in HO-1 since day 7 of AD treatment, with a significant 24-fold increase at day 14 of AD treatment (Figures. 4.15A and B), after which it was gradually decreased. The immunohistochemical analysis for HO-1 and proSP-C performed on the serial lung sections revealed increased localization of HO-1 to AECII in AD treated (day 7, 14, 21 and 28) mice compared to the Veh treated (day 28) controls (Figure 4.15 C). In line with the AD treated lung homogenates, HO-1 expression was prominently upregulated (~ 2-fold) in AD treated isolated murine AECII (Figures 4.15D and E).

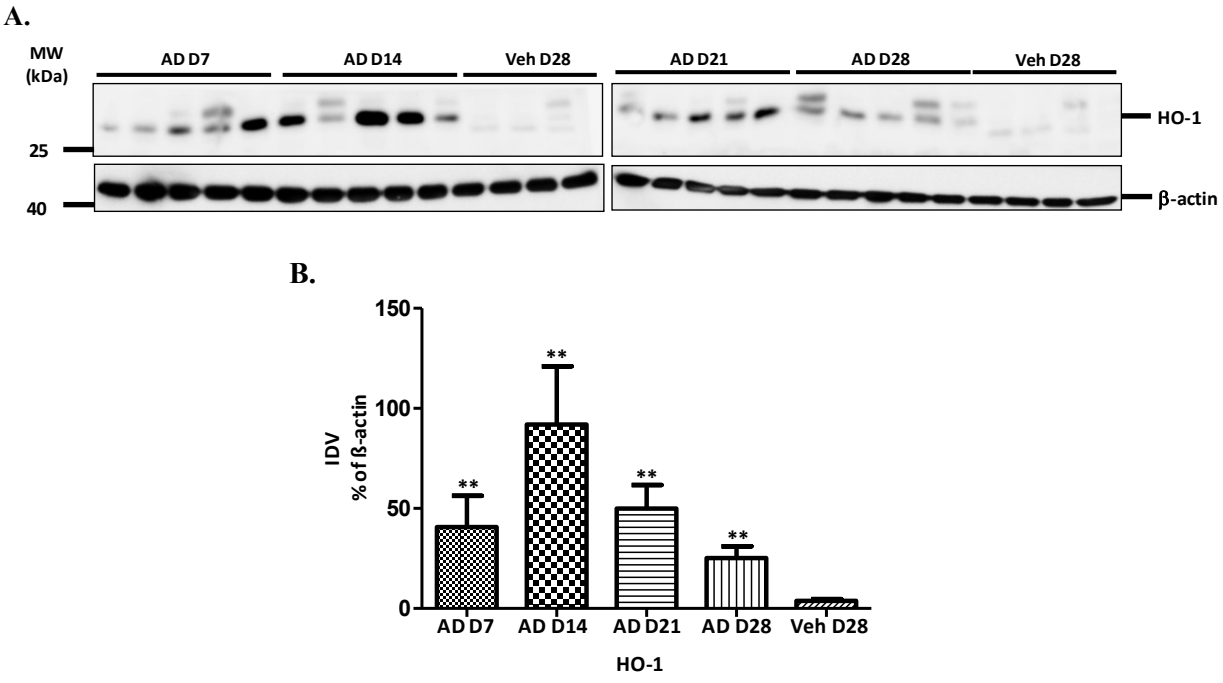

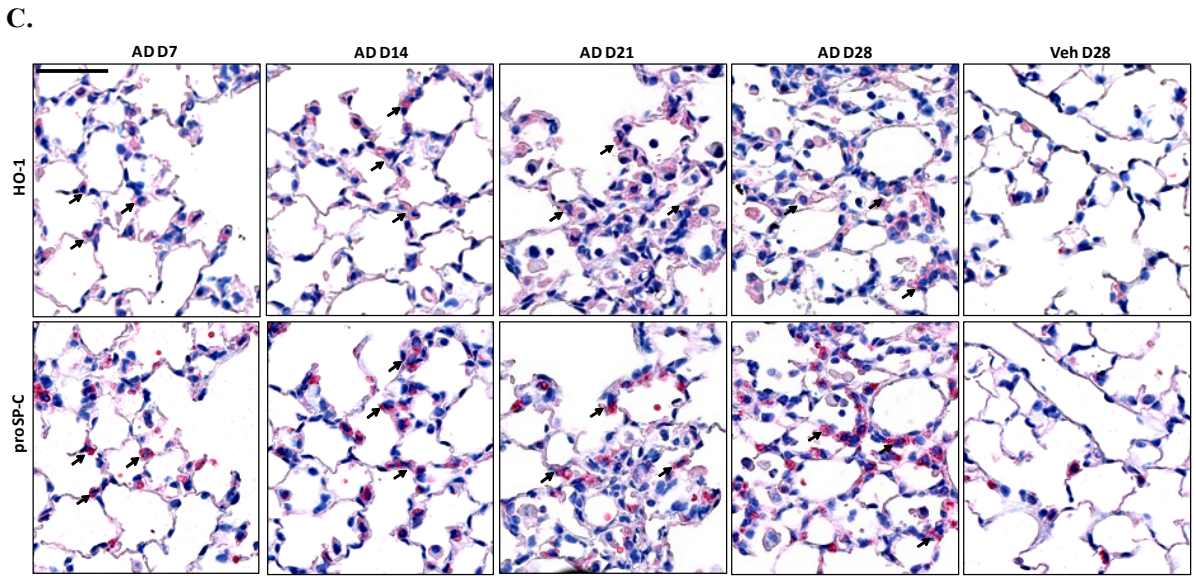
C.
AD D7
AD D14
AD D21
AD D28
Veh D28
HO-1
proSP-C

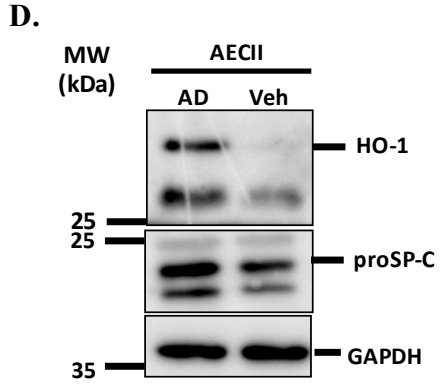
D.
MW
(kDa)
AECII
AD
Veh
HO-1
25
25
proSP-C
35
GAPDH

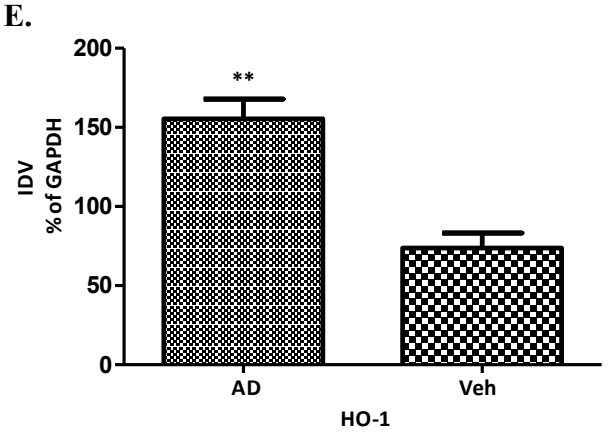
E.
IDV
% of GAPDH
200
150
100
50
0
**
AD
Veh
HO-1

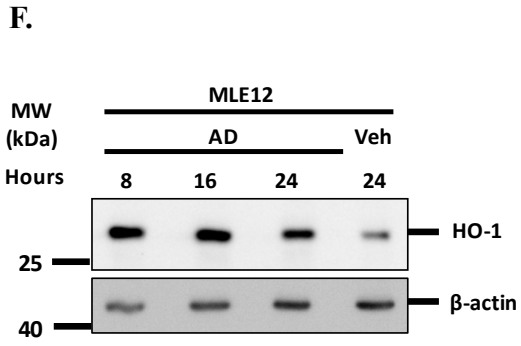
F.
MW
(kDa)
MLE12
AD
Veh
Hours
8
16
24
24
25
HO-1
40
β-actin

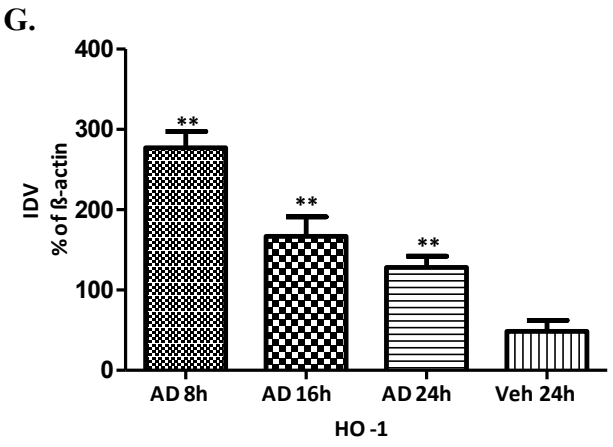
G.
IDV
% of ß-actin
400
300
200
100
0
**
**
**
AD 8h
AD 16h
AD 24h
Veh 24h
HO -1

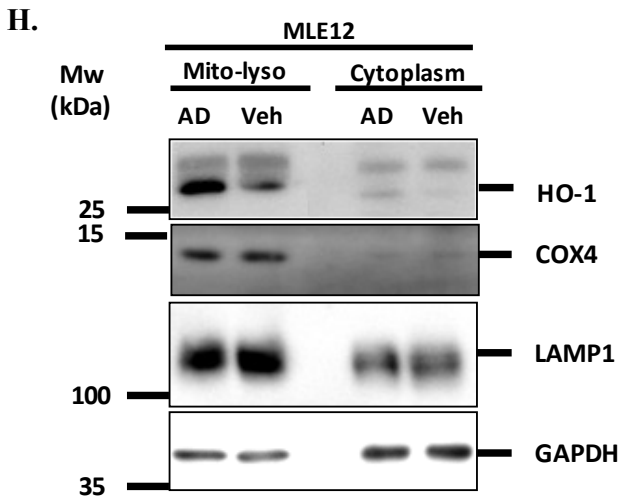

Figure 4.15. Increased HO-1 expression in AD treated mice lungs, primary AECII and MLE12 cells. (A) Western blot analysis of lung homogenates of (left) AD treated mice (day 7, 14) and Veh treated mice (day 28) and (right) AD treated mice (day 21, 28) and Veh treated mice (day 28) for HO-1 and β-actin (loading control). n = 5 mice per group. (B) Densitometry analysis of the HO-1 and β-actin blots and HO-1*100/β-actin ratio was calculated and represented as a bar graph. **p < 0.01. (C) Immunohistochemical analysis of serial lung sections of AD (day 7, 14, 21 and 28) and Veh (day 28) treated mice for HO-1 and proSP-C. Arrows indicate AECII showing increased HO-1 expression from day 7 of AD treatment. n = 5 mice per group. Scale bar = 50 μm. Original magnification: x400. (D) Representative western blot images for HO-1, proSP-C and GAPDH (loading control) from 24 hours of AD or Veh treated C57Bl/6 murine AECII' lysates. n = 3 independent experiments. (E) Densitometry analysis of triplicate blots of HO-1 and GAPDH and HO-1*100/GAPDH ratio was calculated and represented as a bar graph. **p < 0.01. (F) Representative western blot images for HO-1 and β-actin (loading control) from 8, 16 and 24 hours of AD and 24 hours of Veh treated MLE12 cells' lysates. n = 3 independent experiments. (G) Densitometry analysis of triplicate blots of HO-1 and β-actin and HO-1*100/β-actin ratio was calculated and represented as a bar graph. **p < 0.01. (H) Representative western blot images for HO-1, COX IV (Mitochondrial marker), LAMP1 (Lysosomal marker) and GAPDH (cytoplasmic marker) of the isolated cytoplasmic and mitochondrial-lysosomal (Mito-lyso) subcellular fractions from 8 hours of AD or Veh treated MLE12 cells. n = 3 technical replicates.

Similarly, immunoblot analysis of 8, 16 and 24 hours of AD treated MLE12 cells demonstrated a significant increase (~ 5 to 2-fold) in HO-1 expression (Figures 4.15F and G), with its expression decreasing over time in agreement with its expression pattern in AD treated mice lung homogenates. In addition, HO-1 protein significantly increased in the mitochondrial-lysosomal fraction obtained from 8 hours of AD treated MLE12 cells (Figure 4.15H).

When AD-induced oxidative stress was quenched using the antioxidant, NAC, a prominent decrease in the expression of HO-1 protein was noted in MLE12 cells co-treated with AD and NAC (2 mM) for 4 hours (Figures 4.16A and B). In line with this, co-treatment of isolated murine AECII with AD and NAC (2 mM) for 24 hours also demonstrated a significant decrease in the HO-1 protein level (Figures 4.16C and D). Therefore, it is evident that apart from initiating mitochondrial biogenesis and mitophagy, AD-induced oxidative stress also leads to increased antioxidative response in murine AECII.

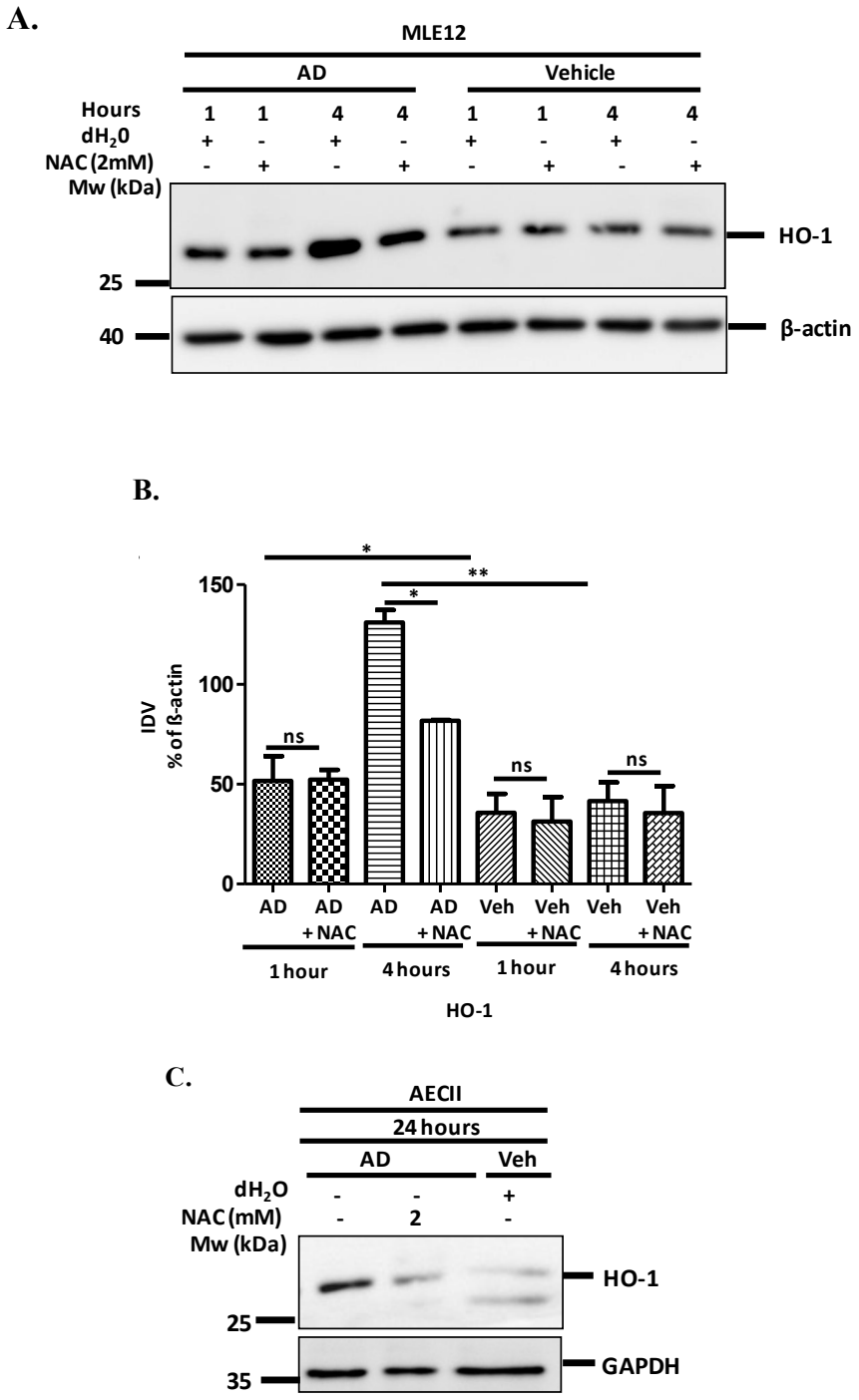

Figure 4.16. Decrease of AD-induced HO-1 by NAC treatment.
(A) Representative western blot images for HO-1 and β-actin (loading control) from 1 and 4 hours of N-acetyl-L-Cysteine (NAC) (2 mM) and AD or Veh co-treated MLE12 cells' lysates. n = 3 independent experiments. (B) Densitometry analysis of the triplicate blots of HO-1 and β-actin (loading control) and HO-1*100/β-actin ratio was calculated and represented as a bar graph. **p < 0.01, *p < 0.05, ns - no significance. (C) Representative western blot images for HO-1 and GAPDH (loading control) from 24 hours of N-acetyl-L-Cysteine (NAC) (2 mM) and AD or Veh co-treated C57Bl/6 murine AECIIs' lysates. n = 3 technical replicates. (D) Densitometry analysis of the triplicate blots of HO-1 and GAPDH (loading control) and HO-1*100/GAPDH ratio was calculated and represented as a bar graph. **p < 0.01, *p < 0.05.

4.4.2. HO-1 independent autophagy in AD treated murine AECII

Since HO-1 forms a major link between oxidative stress and autophagy and many studies demonstrate HO-1 dependent or independent autophagy in different disease conditions, we questioned if AD-induced autophagy was HO-1 dependent. In order to address this, siRNA mediated HO-1 knockdown (HO1si) versus non-targeting siRNA (NTsi) in MLE12 cells was performed for 48 hours, followed by AD or Veh treatment for 8 hours. Knockdown of HO-1 (Figures 4.17A and B) in AD treated MLE12 cells resulted in a further increase in LC3BII protein versus the vehicle (Figures 4.17A and C).

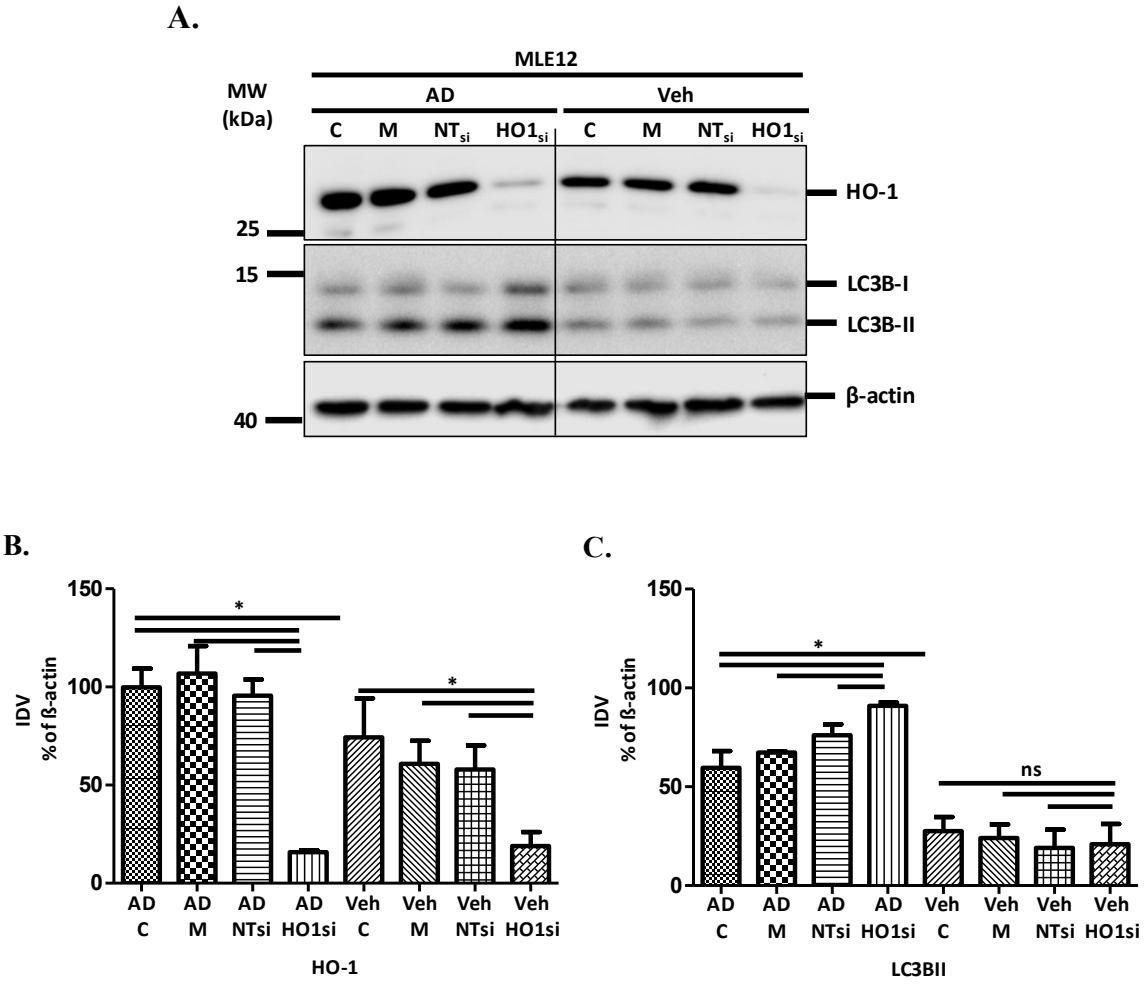

Figure 4.18. HO-1 independent autophagy in AD treated murine AECII.
(A) Representative western blot images for HO-1, LC3B and β-actin (loading control) from 8 hours of AD or Veh treated MLE12 cells transfected with non-targeting siRNA (NTsi) or HO-1 siRNA (HO1si). n = 3 independent experiments. (B and C) Densitometry analysis of triple target proteins' blots namely HO-1, LC3B and β-actin (loading control) and target protein*100/β-actin ratio was calculated and represented as bar graphs. *p < 0.05, ns - no significance.

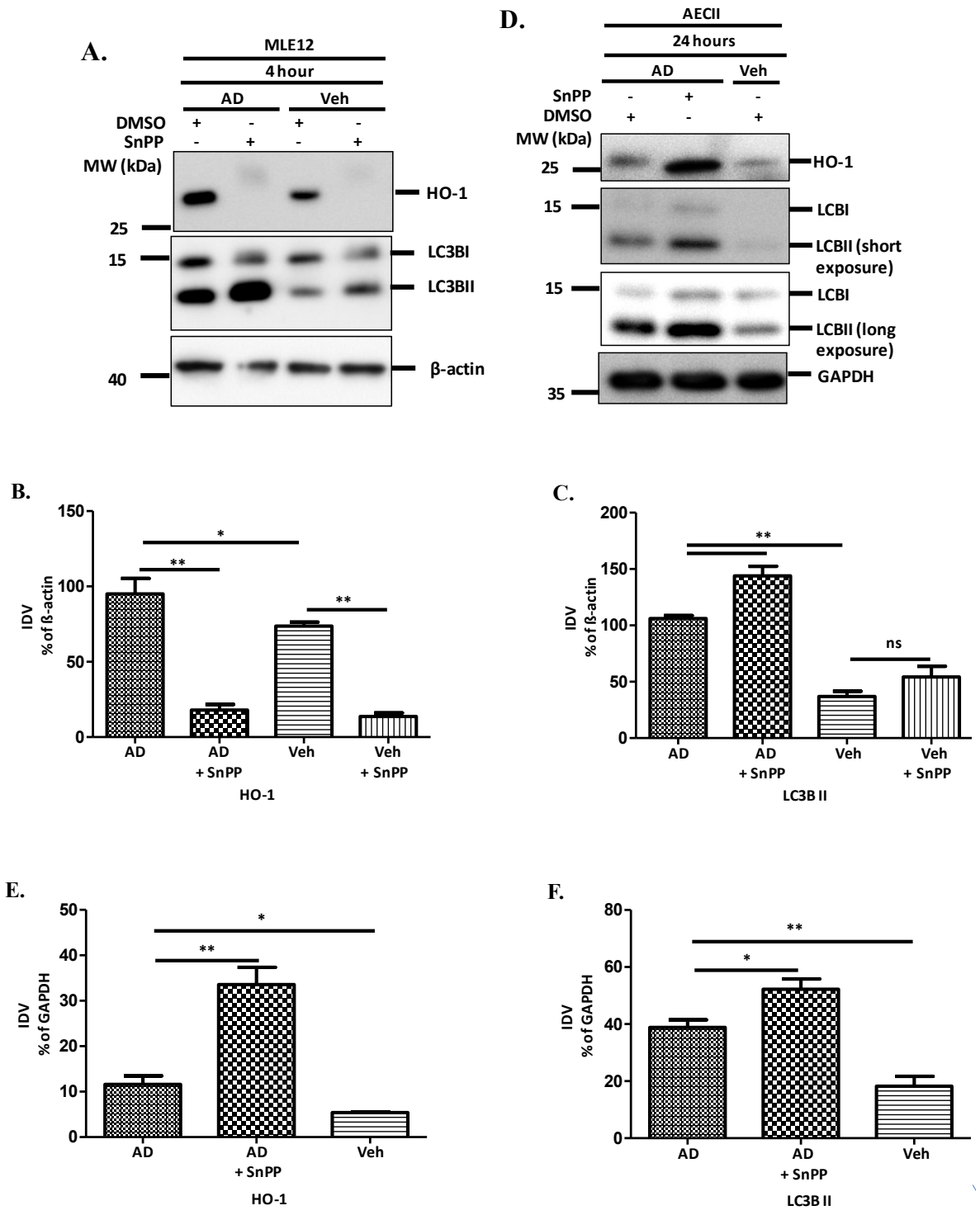

Figure 4.18. Decreased LC3BII production in AD treated AECII upon chemical inhibition of HO-1.
(A) Representative western blot images for HO-1, LC3B and β-actin (loading control) from 4 hours of SnPP and AD or Veh co-treated MLE12 cells. n = 3 independent experiments. (B and C) Densitometry analysis of triple target proteins' blots namely HO-1, LC3B and β-actin (loading control) and target protein*100/β-actin ratio was calculated and represented as bar graphs. **$p < 0.01$, *$p < 0.05$, ns - no significance. (D) Representative western blot images for HO-1, LC3B and GAPDH (loading control) from 24 hours of SnPP and AD or Veh co-treated isolated murine AECII. n = 3 technical replicates. (E and F) Densitometry analysis of triple target proteins' blots namely HO-1, LC3B and GAPDH (loading control) and target protein*100/GAPDH ratio was calculated and represented as bar graphs. **$p < 0.01$, *$p < 0.05$.

In line with this, increased LC3BII levels were observed when primary AECII or MLE12 cells were co-treated with AD and the chemically inhibitor of HO-1, tin protoporphyrin (25 μM), a pharmacological inhibitor of HO-1 for 24 hours and 4 hours respectively (Figures 4.18 A - F). These results thus imply that HO-1 does not induce autophagy in AD treated AECII but may serve cytoprotective under AD treatment.

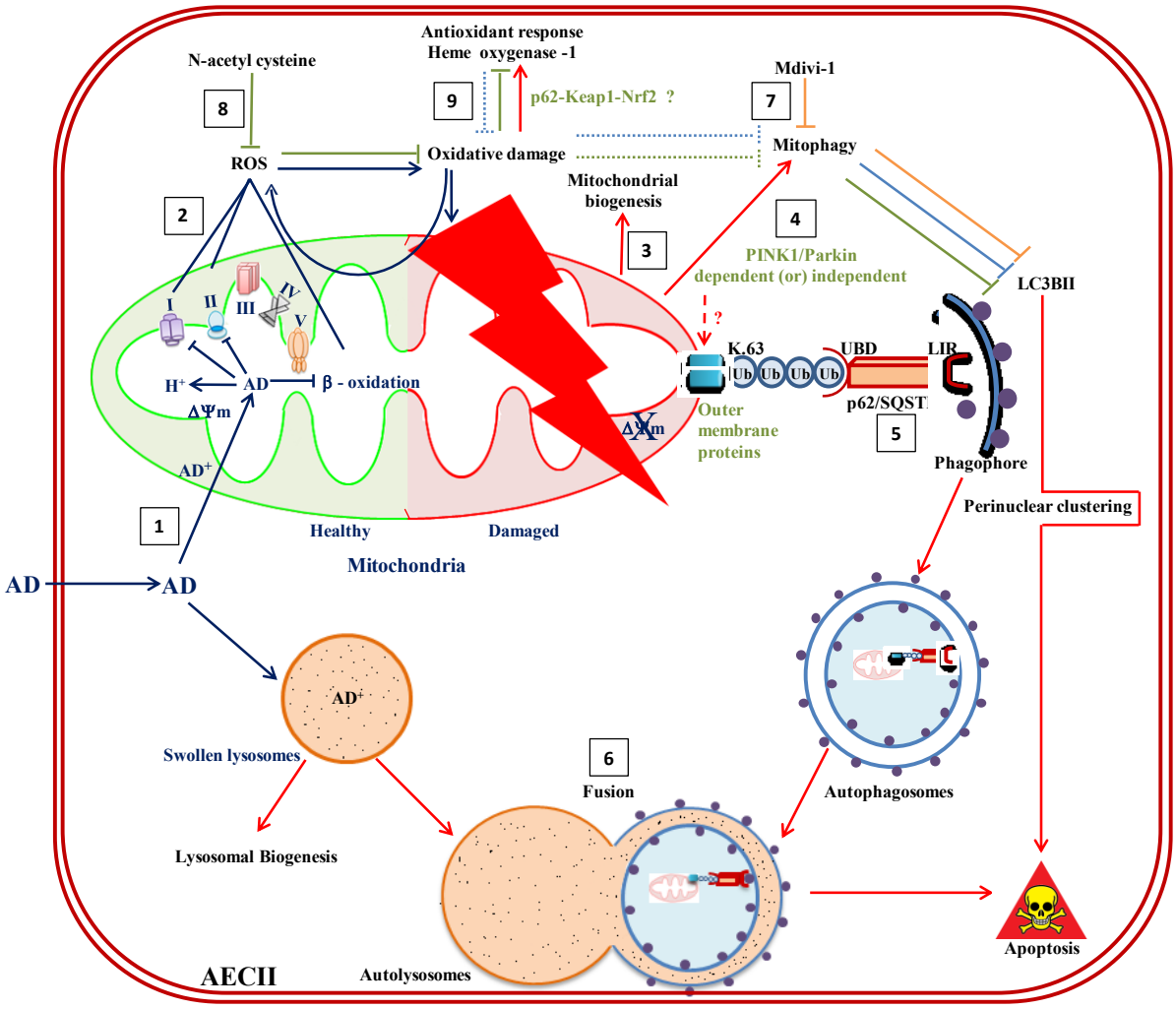

Figure 4.19: Proposed model for AD driven aberrant mitophagy and antioxidative response in AECII. (1) Upon entry into cells *viz* AECIIs (by simple diffusion or *via* organic cation transporters), the cationic drug, AD enters mitochondria due to the negative ΔΨm, where it gets protonated in the acidic intermembrane space and dissipates this acquired proton upon reaching the alkaline mitochondrial matrix. Here, the drug inhibits Complex I and Complex II of respiratory chain and the β-oxidation of lipids, resulting in generation of enormous ROS. (2) The increased ROS induces oxidative stress, which further damages the mitochondria, ultimately leading to a vicious cycle of production of even more ROS and more oxidative stress, thereby resulting in mitochondrial swelling and disruption of ΔΨm. (3) The oxidative damage inflicted on the mitochondria triggers mitochondrial biogenesis and mitophagy. (4) Mitophagy is initiated by fission of the damaged mitochondria from its healthy counterpart and primed (most probably) by PINK1/Parkin dependent or independent pathway, resulting in increased ubiquitination (ubiquitin.K63) of the outer membrane proteins of the damaged mitochondria. (5) The autophagy adapter protein, p62 then recognizes these ubiquitinated mitochondria *via* its UBA domain and targets them into the autophagosomes *via* its interaction with LC3 on the autophagosomes through the LIR. (6). The autophagosomes entrapping the damaged mitochondria are subsequently fused with the swollen lysosomes (since the cationic AD is also entrapped by the acidic lysosomes, where AD gets protonated and accumulated, resulting in endomembrane pH buffering leading to osmotic swelling and activation of lysosomal biogenesis as a feedback mechanism). (7, 8). Inhibition of AD- induced mitophagy or oxidative stress by mdivi-1 and NAC respectively reduces the rate of LC3B lipidation. Thus proving, AD steered oxidative stress drives aberrant mitophagy that probably leads to enhanced apoptosis of AECII. (9) AD-induced oxidative stress also increases the antioxidative response *via* HO-1, probably resulting from the activation of p62-Keap1-Nrf2 pathway. Further, HO-1does not induce autophagy, instead reduces it and serves to be cytoprotective. Text and arrows represented in blue are based on the facts derived from pre-existing literature as explained in the penultimate paragraph of section 1.1.5. Rest of the figure is depicted based on the findings of this study, except those represented in green text and dotted lines, which are mechanism that still remain to be proven in this model.

5. Discussion

The initial focus of the current study was to identify mechanisms underlying AD-induced apoptosis of alveolar epithelial cells. As an attempt to study this, siRNA mediated gene silencing of Cathepsin D was performed followed by AD treatment in MLE 12 cells. However, a significant decrease in cleaved caspase 3, a reliable terminal apoptosis marker, was not observed upon Cathepsin D knockdown under AD treatment conditions. It was further identified that AD treatment leads to increased lysosomal biogenesis, as indicated by increased LAMP1 & LAMP2 both in AD treated mice lungs as well as in AD treated MLE12 cells *in vitro*. In addition, AD induces macroautophagy and increased autophagy flux in alveolar epithelial cells and inhibition of LC3B, a pivotal protein of macroautophagy pathway, attenuates the extent of AD-induced apoptosis of alveolar epithelial cells *in vitro*. Further, in line with the fact that AD is a potential mitochondrial toxicant, a remarkable increase in ROS production; particularly a surge in superoxide radicals ($O_2^{\cdot-}$) generation has been recorded in AD treated mice MLE12 cells and a significant increase in mitochondrial biogenesis has also been shown in mice AECII following AD treatment. In continuum, AD has been effectively demonstrated to increase the expression of p62 (and not that of BNIP3, BNIP3L and NBR1 proteins) in AD treated mice AECII and to promote mitophagy *via* AD-induced p62 mediated targeting of dysfunctional mitochondria to autophagosomes and lysosomes in AECs. Furthermore, a prominent decrease in LC3B lipidation (LC3BII) has been shown upon inhibition of AD driven mitophagy (or) ROS with mdivi-1 and NAC respectively in mice AECs and a reduction in annexin V (apoptotic marker) staining has also been observed in AD treated AECs following mdivi-1 treatment. In addition, as a consequence of AD-induced oxidative stress, a significant increase in the expression of antioxidative protein, HO-1 has also been demonstrated in mice AECII upon AD treatment, but knockdown of HO-1 did not reveal a significant decrease in AD-induced autophagy. These studies indicate that **a)** AD-induced extensive apoptosis of AECII is LC3B dependent, **b)** AD steered oxidative stress drives aberrant mitophagy *via* p62 and **c)** AD-induced autophagy is HO-1 independent. (Figure 4.19).

5.1. Epithelial cell stress and apoptosis in response to AD treatment

5.1.1. AECII apoptosis in AD-induced pulmonary fibrosis

AD is a widely used anti-arrhythmic drug that causes fatal pulmonary toxicity, categorizing itself under drug induced interstitial lung diseases (ILD). The exact molecular mechanisms

underlying AD-induced pulmonary fibrosis remain obscure (Barbas-Filho *et al.,* 2001, Korfei *et al.,* 2008, Mahavadi *et al.,* 2010, Wang *et al.,* 2000). But it shares its pathomechnistic features with other forms of ILDs like idiopathic pulmonary fibrosis (IPF), where chronic injury and apoptosis of AECII, ensuing frustrated alveolar repair are now considered as key events (Coward *et al.,* 2010; Günther *et al.,* 2012; Mahavadi *et al.,* 2014; Birkelbach *et al.,* 2015). Another well characterized observation for ILDs is that injured AECII synthesizes a variety of pro-fibrotic enzymes, cytokines and growth factors (*E.g.* matrix metalloproteinase, TGF-β, tumour necrosis factor - α (TNFα), platelet derived growth factor (PDGF), that lead to excessive connective tissue (fibroblast/myofibroblast) deposition, aberrant tissue remodelling and subsequent destruction of the lung parenchyma that forms fibrotic lesions (Selman *et al.,* 2002), altogether resulting in progressive dyspnea, decline of lung function and, ultimately, death (American Thoracic Society/European Respiratory Society International Multidisciplinary Consensus Classification of the Idiopathic Interstitial Pneumonias.This joint statement of the American Thoracic Society (ATS), and the European Respiratory Society (ERS) was adopted by the ATS board of directors, June 2001 and by the ERS Executive Committee, June 2001, 2002). In line with this, extensive alveolar epithelial cell death and remarkably increased apoptosis of AECII in regions adjacent to the fibroblast foci in advanced fibrotic human lung were reported (Myers *et al.,* 1988; Uhal *et al.,* 1998). This concept was further supported by appealing observations like severe and pro-apoptotic endoplasmic reticulum (ER) stress signaling in AECII from UIP lungs due to familial and sporadic IPF (Korfei *et al.,* 2008) and shortened telomere length in the epithelium of sporadic IPF subjects (Alder *et al.,* 2008). Other apoptotic changes *viz* fine and uniformly dispersed chromatin within the nuclear membrane and swollen mitochondria with ruptured outer membrane have also been documented in the electron microscopic analysis of normal alveoli of IPF lungs (Barbas-Filho *et al.,* 2001). The concept of AECII injury as a triggering factor of lung fibrosis has also been supported by experimental data in animal models, where anti-apoptotic agents prevented bleomycin induced lung fibrosis (Wang *et al.,* 2000). AECII injury as a result of lysosomal and ER stress leading to apoptosis was also reported in Hermansky-Pudlak syndrome (HPS) associated lung fibrosis, a genetic model of lung fibrosis (Mahavadi *et al.,* 2010).

Along the same lines, direct exposure to AD has been demonstrated to induce apoptosis of human (Choi *et al.,* 2002, Nicolescu *et al.,* 2007) and other mammalian lung epithelial cells (Mahavadi *et al.,* 2014, Bargout *et al,* 2000). Likewise, induction of TGF-β in lung tissues of

AD treated rats (Chung *et al.,* 2001) and apoptosis of AECII in the rat as well as mouse model of AD-induced pulmonary fibrosis was also demonstrated (Uhal *et al.,* 2003; Mahavadi *et al.,* 2014). Such AECII apoptosis was accompanied by altered surfactant homeostasis and epithelial stress (ER and lysosomal stress) in AD treated mice (Mahavadi *et al.,* 2014), again supporting the concept of alveolar epithelial cell injury as a triggering factor in the development of lung fibrosis.

5.1.2. Lysosomal alterations in AD-induced pulmonary fibrosis

Studies from our group have reported increased accumulation of AD-induced multi-lamellar bodies (lysosome related organelles) and elevated lysosomal stress indicated by increased cathepsin D in mice AECII following AD treatment (Mahavadi *et al.,* 2014). Following this, AD driven macroautophagy, a lysosome dependent degradation pathway was also reported in mice AECII (Mahavadi *et al.,* 2015). So, in the present study an effort was made to decipher whether cathepsin D (or) macroautophagy pathway drives apoptosis in AD treated mice AECII. Unlike the HPS associated lung fibrosis, where cathepsin D was demonstrated to mediate apoptosis of alveolar epithelial cells (Mahavadi *et al.,* 2010), apoptosis of AD treated MLE12 cells was not mediated by cathepsin D. Instead, knockdown of the major macroautophagy protein, LC3B had resulted in drastic down regulation of cleaved caspase 3 in AD treated MLE12 cells, thus proving a macroautophagy dependent apoptotic pathway activation in mice AECII following AD treatment. This corroborates with few earlier findings where inhibition of LC3B *via* LC3siRNA inhibited the activation of caspase-3 and caspase-8 in cigarette smoke (CS) exposed human bronchial epithelial cells (BEAS-2b) (Kim *et al.,* 2008b) and LC3B knockout mice demonstrated significant decrease in apoptosis in the lungs after CS exposure (Chen *et al.,* 2010). In addition, LC3B knockdown also decreased proSP-C in AD treated MLE12 cells, implying macroautophagy dependent dysregulation of proSP-C in AECII following AD treatment. These observations therefore point towards a critical role of macroautophagy in AD-induced AECII apoptosis, proSP-C dysregulation.

5.1.2.1. Autophagy flux in AD-induced pulmonary fibrosis

In addition to AD steered lysosomal stress and macroautophagy (Mahavadi *et al.,* 2014; Mahavadi *et al.,* 2015), an increase in lysosomal biogenesis was also noticed in mice AECII upon AD treatment. This was evident by an increased expression and intense staining of LAMP1 and LAMP2 proteins in AD treated mice AECs. This is in line with the facts that AD

being a cationic amphiphilic drug gets protonated and accumulated in the acidic milieu of the lysosomes, followed by endomembrane pH buffering and inhibition of lysosomal enzymes *viz* phospholipases, which ultimately results in osmotic swelling and feedback activation of lysosomal biogenesis (Baritussio *et al.,* 2001, Marceau *et al.,* 2014). An increase in the lysosomal volume have also been reported in other cationic amphiphilic drugs *viz* imipramine (Funk and Krise, 2012) and elevated expression of LAMP proteins have also been demonstrated in other lysosomotrophic drugs like chloroquine (Chen *et al.,* 2011).

Under such proven circumstances of macroautophagy dependent apoptosis and surfactant dysfunction and increased lysosomal biogenesis in AD treated AECs, it was imperative to determine autophagy flux under AD treatment in order to know if AD induces (or) inhibits autophagy. An efficient fusion of autophagosomes and lysosomes was demonstrated in AD treated MLE12 cells confirming no blockage in the step of fusion of the autophagic pathway (Mahavadi *et al.,* 2015). So, in an attempt to find if AD induces a late stage autophagy inhibition, initial analyses were performed with Baf A1 inhibitor. Surprisingly, the AECs treated with AD and Baf A1 revealed loss of vacuolar cytopathology induced by AD. This observation was in complete agreement with the report of Morissette *et al.,* 2009, which demonstrates that Baf A1, a V-ATPase inhibitor prevents vacuolization and cellular uptake of AD. Thus, the notion of measuring autophagy flux for AD using Baf A1 was abandoned. Contrastingly, a study by Lee & colleagues reported that AD increases autophagy flux in lung epithelial cell lines by using Baf A1 as an autophagy inhibitor to study autophagy flux (Lee *et al.,* 2013). Therefore, measurement of autophagy flux in AD treated MLE12 cells were then performed using the autophagy inhibitor, chloroquine. Pre-treatment of cells with chloroquine, revealed an increase in LC3BII, compared to treatment with AD alone, indicating an increase in the autophagy flux in AECs following AD treatment. These observations are in full support of previously reported studies, where an induction of autophagy and increase in autophagy flux were reported in several other cell types (Lin *et al.,* 2015; Morrissette *et al.,* 2009).

5.1.3. Oxidative stress and mitophagy in AD-induced pulmonary fibrosis

5.1.3.1. ROS production in AD-induced pulmonary fibrosis

AD is a potential mitochondrial toxicant, well known to cause structural and functional perturbations to the mitochondria (Bolt *et al.,* 2001, Card *et.al.,* 1998). In fact, AD is metabolized by the P450 enzymes system to its metabolite, DEA. Both AD and DEA have

been shown to inhibit β-oxidation of fatty acids (Fromenty *et al.,* 1990b, Spaniol *et al.,* 2001) and respiratory chain complexes (I and II) and deplete ATP production (Fromenty *et al.,* 1990a, Bolt *et al.,* 2001, Felsar *et al.,* 2013). In intact hamster lung alveolar macrophages and preparations enriched with isolated AECII and non-ciliated bronchiolar epithelial clara cells, AD was demonstrated to decrease mitochondrial membrane potential within 2 hours of treatment, followed by ATP depletion at 6 hours of AD treatment (Bolt *et al.,* 2001). Nicolescu *et al.,* in 2008 reported that this preceding mitochondrial dysfunction has led to increased production of ROS in AD treated human peripheral lung epithelial HPL1A cells, where it has been demonstrated that incubating HPL1A cells with 100 μM AD for shorter incubations (< 2 hours) resulted in a decreased uptake of mitotracker orange, indicative of decreased mitochondrial integrity and release of Cyt C, whereas longer incubation times (≥ 6 hours) significantly increased ROS formation.

ROS are grouped amongst key players that modulate the pathogenesis of fibrotic lung diseases; including IPF and other forms of interstitial lung diseases *viz* the drug induced pulmonary fibrosis (Kinnula, 2008). ROS involved in various pathologies include radicals such as superoxide anion ($O_2^{\cdot-}$), hydroxyl ($HO^{\cdot}$), hydroperoxyl ($HOO^{\cdot}$), lipid peroxyl ($LOO^{\cdot}$), carbonate ($CO_3^{\cdot-}$) and non-radical molecules *viz* hydrogen peroxide (H_2O_2), singlet oxygen ($^1O_2$), and peroxynitrite anion ($ONOO^-$) (Nicolescu *et al.,* 2008). ROS inflicts oxidative damage on the mitochondrial lipids, DNA and proteins, which makes mitochondria further vulnerable to ROS production (Ashrafi and Schwarz, 2013). AD has been demonstrated to generate $^1O_2$ and $O_2^{\cdot-}$ photochemically in air-equalibrated aqueous solution (Onoue and Tsuda, 2006). In other studies, ESR measurements employing the spin trap, 5,5-Dimethyl-1-Pyrroline-N-Oxide (DMPO) displayed that AD and a non-iodinated AD analogue (DDIA) generates free radicals in simple chemical systems in the presence of oxygen (Taylor *et al.,* 2003, Nicolescu *et al.,* 2008). In consistence with this, ESR analysis performed in the current study with 8 hours of AD treated MLE12 cells employing the spin probe CMH revealed increased reactive oxygen species production; particularly a surge in $O_2^{\cdot-}$ production was evident. Corroborating increased ROS production under AD treatment, markers of oxidative stress *viz* 8-Isoprostane (a product of free radical mediated lipid peroxidation) and oxidized protein with carbonyl modifications have been recorded to be elevated in the BALF of IPF patients (Kliment *et al.,* 2006, Lenz *et al.,* 1996, Montuschi *et al.,* 1998) and in the exhaled breath condensates of interstitial lung disease (ILD) patients (Psathakis *et al.,* 2006, Kliment

et al., 2006, Kanoh *et al.,* 2005), indicating ROS driven oxidative stress to be one of the key players in the pathogenesis of pulmonary fibrosis.

Increased ROS also triggers the opening of mitochondrial permeability transition pore (mPTP), a trans bi-membrane channel, which allows the passage of solutes up to 1.5 kDa, including the release of Ca^{2+}, Cyt C, apoptosis inducing factor (AIF) and other pro-apoptotic proteins. Opening of mPTP might also lead to the influx of water into the mitochondrial matrix resulting in mitochondrial swelling (Hellebrand *et al.,* 2010, Galindo *et al.,* 2003). Increased ROS observed under AD treatment were also found to in line with the swollen mitochondria observed in the transmission electron micrograph of AECII from AD (day 7) treated mice (Unpublished data). AD-induced mitochondrial swelling have also been reported in the non-pulmonary cells such as the prostate cancer cell line DU145 (Mitrakas *et al.,* 2014), lymphocytes (Yasuda *et al.,* 1996), isolated rat liver mitochondria (Kaufmann *et al.,* 2003) and also in parasitic protozoans *viz Leishmania amazonensis* and *Trypanosoma cruzi* (De Macedo-Silva *et al.,* 2011, Adesse *et al.,* 2011). Although AD-induced mitochondrial swelling has been demonstrated, it should be noted that in certain studies AD has been reported as a mitochondrial permeability transition pore inhibitor (Hellebrand *et al.,* 2010, Varbiro *et al.,* 2003b). This dual property of AD has been associated with its dosage. At low concentrations, AD has been proven to inhibit Ca^{2+} induced mitochondrial swelling and prevent the release of pro-apoptotic factors but at higher concentrations, AD has been shown to induce cyclosporin A (CsA)- independent mitochondrial swelling (Varbiro *et al.,* 2003a,b). The AD metabolite, DEA also induces mitochondrial swelling at higher concentrations (Varbiro *et al.,* 2003b). Recently, increased swollen mitochondria with disorganised cristae were also described in the IPF lung (Patel *et al.,* 2015) and upon morphometric analyses of electron microscopy images, another study group revealed abnormally swollen and dysmorphic mitochondria with significantly increased mitochondrial area and frequency of large mitochondria exclusively in the AECII of IPF lungs (Bueno *et al.,* 2015). Of note, such impairment of mitochondrial function and its contribution towards alveolar epithelial cell death was also shown in asbestos induced lung fibrosis (Liu *et al.,* 2013; Cheresh *et al.,* 2015).

5.1.3.2. Mitochondrial mass in AD-induced pulmonary fibrosis

Apart from being the toxic by-products of oxidative metabolism, ROS are now considered signalling molecules that mediate redox regulation of several processes including

mitochondrial biogenesis and mitophagy (Yoboue *et al.,* 2012, Scherz-Shouval *et al.,* 2007). Mitochondrial biogenesis and mitophagy are closely coupled events that regulate cellular adaptation in response to mitochondrial malfunction, thus playing an active role in maintaining mitochondrial and cellular homeostasis. The significance of the intricate interplay between these two processes has been emphasized by the aberrantly increased mitochondrial content observed in different pathological conditions such as neurodegenerative and ageing associated diseases (Palikaras and Tavernarakis, 2014, Kubli and Gustafsson, 2012).

Mitochondrial biogenesis is a sophisticated multi-step process, which involves a highly co-ordinated transcription and translation of two different genomes (the nucleus and the mitochondria) and the recruitment, import and assembly of the resulting newly synthesized proteins and lipids into an expanding mitochondrial reticulum (Palikaras and Tavernarakis, 2014, Yoboue *et al.,* 2012). An increase in mitochondrial mass and mitochondrial DNA (mtDNA) content, reflecting an increase in mitochondrial biogenesis has been described in H_2O_2 treated human lung fibroblast cell line (Lee *et al.,* 2000). Similar study in the same cell line treated with H_2O_2 reported an increase in the mRNA levels of nuclear respiratory factor 1(NRF1), a transcription factor involved in mitochondrial biogenesis (Lee *et al.,* 2002). A recent study in a stable cell line expressing a frequently reported human surfactant protein C mutation of threonine for isoleucine at codon 73 (hSP-C^{I73T}), associated with ILD demonstrated an increase in the expression of mitochondrial component, cytochrome c oxidase subunit II (COX II), which is suggestive of a rise in the overall mitochondrial biomass (Hawkins *et al.,* 2015). Estimation of the mitochondrial content by quantifying the ratio of mitochondrial to genomic DNA (mtDNA/gDNA) in the AECII and fibroblasts of IPF lungs revealed a significant increase in mtDNA/gDNA ratio exclusively in the AECII of IPF lungs but not in the fibroblasts (Bueno *et al.,* 2015). In line with this, AD was shown to induce mitochondrial biogenesis in AECs. An increased expression of COX IV, a nuclear-encoded mitochondrial protein was observed in the AD treated mice lungs, AECII and MLE12 cells. In an earlier study employing AD, human hepatoma HepaRG cells were shown to induce the expression of peroxisome proliferator-activated receptor gamma co-activator 1-alpha (PPARGC1A) gene involved in mitochondrial biogenesis (Anthérieu *et al.,* 2011).

5.1.3.3. Mitophagy in AD-induced pulmonary fibrosis

Considering the facts that the ROS regulates Atg4 family of cysteine proteases that are important for autophagosome formation (Scherz-Shouval *et al.,* 2007) and that AD mediates AECII specific autophagy in murine model of AD-induced pulmonary fibrosis (Mahavadi e*t al.,* 2015), it was convincing to speculate that AD-induced ROS and mitochondrial dysfunction induces mitophagy in mice AECII. Increased co-localization of mitochondrial marker protein (COX IV) with autophagosomal (GFP-LC3B) and lysosomal marker proteins (LAMP1/cathepsin D) witnessed in AD treated MLE12 cells and AECII directly implies the entrapment of damaged mitochondria by autophagic machineries in AECII upon AD treatment. In an effort to find the possible pathway that directs such dysfunctional mitochondria into autophagic machinery, a methodical analysis of expression of different mitophagy proteins were performed in AD treated murine AECII.

Bnip3L and Bnip3 are the mitochondrial autophagy receptor proteins that directly target dysfunctional mitochondria into the autophagosomes *via* their binding to Atg8 family of proteins (Ding and Yin, 2012, Hanna *et al.,* 2012). In the present study, the expression of Bnip3L and Bnip3 were found to remain constant in AD treated mice lungs, AECII and MLE12 cells. The mitochondrial-lysosomal enriched fractions of AD and Veh treated MLE12 cells also exhibited unaltered expression of these proteins. In general, upregulation in the expression of these proteins have been reported during their active participations in mitophagy (Ding and Yin, 2012; Johansen and Lamark, 2011). Thus, the unaltered expression of these proteins rules out the possibility of their involvement in AD driven mitophagy in AECII. Concurrent analyses of the expression of autophagy adaptor proteins, p62 and NBR1 in mice AECII under AD treatment revealed a significant upregulation in the expression of p62 in AD treated mice AECII, whereas the expression of NBR1 (except in AD treated lung homogenate) remained constant in the AD treated murine AECII. This is in line with the previous study from our group that had demonstrated AD-induced transcriptional upregulation of p62 in AECs (Mahavadi *et al.,* 2015). In addition, the expressions of autophagic proteins ATG12-ATG5 and ATG7, which also play a pivotal role in mitochondrial clearance (Wu *et al.,* 2009, Liu *et al.,* 2012) were noted to be prominently increased in AECII upon AD treatment.

Such increase in p62 protein was also reported in both fibroblasts as well as in AECII of IPF lungs (Hawkins *et al.,* 2015, Bueno *et al.,* 2015). Although not reported under conditions of lung fibrosis, studies from other model systems *viz* drosophila reveal the recruitment of p62

to dysfunctional mitochondria and its crucial role in aggregation *via* its PB1 domain mediated polymerization (in a manner analogous to aggregation of polyubiquitinated proteins) results in the clearance of dysfunctional mitochondria (Park *et al.,* 2014, Geisler *et al.,* 2010, Narendra *et al.,* 2010). This led us to retrospect the role of increased p62 in AECII under AD treatment, specifically with reference to mitophagy. Akin to the aforementioned publications, p62 mediated targeting of dysfunctional mitochondria to the autophagic machinery was observed in AECs under AD treatment. This is evident from increased co-localization of p62 with GFP-LC3 and LAMP1/cathepsin D in AD treated MLE12 cells and AECII and also from increased p62 detected in the mitochondrial-lysosomal enriched fraction of AD treated MLE12 cells.

Although growing line of evidence strengthens the indispensable role of p62 in mitophagy, certain studies (Okatsu *et al.,* 2010, Narendra *et al.,* 2010)identified that p62 is essential only for perinuclear mitochondrial clustering but is not required for mitophagy. Okatsu *et al.,* 2010 reported that upon deletion of p62 in mouse embryonic fibroblasts (MEFs), a gross loss of mitochondrial perinuclear clustering was observed without hindering mitochondrial degradation. In contrast, Geisler *et al.,* 2010 demonstrated drastic inhibition of mitochondrial clearance in p62 knocked down HeLa cells. A straightforward explanation for these contrasting observations is the existence of functionally redundant proteins. For example, the loss of p62 could be compensated by the autophagy adaptor protein, NBR1 (Okatsu *et al.,* 2010, Narendra *et al.,* 2010). This may also explain the unaltered expression of NBR1 in AD treated AECII, where abundant p62 could be detected. Interestingly, although total protein level of NBR1 remained unaltered, it did co-localize with autophagosomes and lysosomes at few perinuclear loci of AD treated MLE12 cells. This may be explained as an outcome of polymerization of constantly expressed NBR1 *via* its PB1 domainunder AD treatment, where NBR1 can be part of (or) the chain terminator of a polymeric chain of p62 molecules (Johansen and Lamark, 2011).

Ubiquitination serves as the main denominator for targeting substrates *viz* protein aggregates, mitochondria, peroxisomes, ribosomes and invading bacteria to proteasomal or autophagic degradation, thus acting as a ‘Kiss of death’ signal (Kirkin *et al.,* 2009, Shaid *et al.,* 2013). The accumulation of p62 in ubiquitin-positive inclusions have been reported in several neurodegenerative and chronic liver diseases (Johansen and Lamark, 2011). The anchorage of ubiquitin to peroxisomes has been shown to be sufficient for p62 recruitment and pexophagy (Kim *et al.,* 2008a). Under AD treatment, an increased expression of ubiquitin.K63 was noticed in murine AECII. This is in line with increased accumulation of p62 observed in AD

treated AECII, which exhibits a stronger binding towards ubiquitin.K63 chain linkages (Kirkin *et al.,* 2009). Further, increased co-localization of ubiquitin.K63 with GFP-LC3B and LAMP1 was evident in MLE12 cells under AD treatment. Thus, increased ubiquitin.K63 drives the recruitment of p62 to the dysfunctional mitochondria, thereby targeting the ubiquitinated mitochondria into the autophagic machinery in AECII under AD treatment.

Parkin, a cytosolic E3 ubiquitin ligase, recruited onto the dysfunctional mitochondria upon PINK1 stabilization (Narendra *et al.,* 2008, Narendra *et al.,* 2010) is reported to be responsible for ubiquitinating (addition of polyubiquitin chains to lysine-63 or lysine-27) various mitochondrial outer membrane proteins *viz* voltage dependent anion channel (VDAC) (Geisler *et al.,* 2010) and induce mitophagy. This is a well established pathway that has emerged as a paradigm for mammalian mitophagy (Ashrafi and Schwarz, 2013), where mutations in either of genes have been shown to have serious impact on clearance of dysfunctional mitochondria (Lee *et al.,* 2010, Park *et al.,* 2006). Recent reports have demonstrated the involvement of other E3 ubiquitin ligases such as the Glycoprotein 78 (Gp78) in inducing mitophagy in a Parkin-independent pathway (Fu *et al.,* 2013). It still remains to be elucidated if PINK1/Parkin dependent or independent (involving Gp78 E3 ubiquitin ligase) ubiquitination of mitochondrial outer membrane proteins occurs in the murine model of AD-induced pulmonary fibrosis, amidst recent reports from two independent groups revealing quite contrasting observations on the expression of PINK1 protein in IPF (Bueno *et al.,* 2015; Patel *et al.,* 2015). In addition, another recent study reported elevated cytosolic and mitochondrial levels of parkin in a stable cell line expressing mutant human surfactant protein C, hSP-C^{I73T} (Hawkins *et al.,* 2015).

Division (or) fission of mitochondria is a prerequisite for mitophagy (Ding and Yin, 2012, Gomes and Scorrano, 2013), therefore inhibition of mitochondrial division should prevent mitophagy. Upon treatment of AD treated MLE12 cells with the pharmacological mitochondrial fission inhibitor, mdivi-1, a significant reduction in lipidation of LCB, *i.e.* LC3BII and reduction in annexin V staining was observed. This is coherent with decrease of cleaved caspase 3 witnessed in AD treated LC3B knocked down MLE12 cells. Thus, the inhibition of AD driven aberrant mitophagy displays the potential to prevent AECs apoptosis and serves to be cytoprotective. This is in line with many recent studies revealing cytoprotection offered by mdivi-1 in several different scenarios such as - protection against cell death induced by cigarette smoke in pulmonary epithelial cells *in vitro* (Mizumura *et al.,* 2014), attenuation of spinal cord ischemia-reperfusion (IR) injury by reducing neuronal apoptosis (Liu *et al.,* 2015), prevention of apoptosis of cardiomyocytes and improving

cardiac function induced by renal IR in acute cardiorenal syndrome (Sumida *et al.,* 2015) and inhibition of IR injury in primary hippocampal cells by preventing oxygen - glucose deprived cell death (Wang *et al.,* 2014).

NAC is a thiol-containing antioxidant that scavenges several ROS. NAC also acts as a cellular source of cysteine for the endogenous production of glutathione (GSH) and suppresses the activation of transcription factors *viz* NF- κB (Day, 2008). NAC is used in the clinical settings for various purposes especially in context of its antioxidative potential (Durukan *et al.,* 2002). Similar to mdivi-1, reduced LC3B lipidation was observed in AD treated mice AECII when AD-induced ROS were quenched using the antioxidant NAC. This reduced LC3B indicates the probable potential of NAC to prevent AECII apoptosis induced by AD steered oxidative stress. This observation with NAC was in coherence with its therapeutic potential that had been recently reported to curb AD-induced liver injury in a patient (Mudalel *et al.,* 2015) and with the prevention of cytotoxicity demonstrated in AD treated mouse fibroblasts (Durukan *et al.,* 2002). Both oral and inhaled NAC treatment have been demonstrated to avert drug (*E.g.* bleomycin (or) AD) induced lung fibrosis in rats, mice and hamsters (Day, 2008). In addition, the oral therapy in IPF patients with this FDA approved mucolytic drug exhibited an increase in the GSH levels in the ELF of the patients' lungs. Although some improvements have been reported in exercise desaturation and high-resolution CT images in IPF patients upon NAC inhalation therapy, little to modest changes were noted in the pulmonary function tests and quality-of-life scores (Day, 2008). In spite of this, the latest INSIGHTS-IPF registry reports treatment of 33.7 % of IPF patients in Germany with NAC, ranking second in preference to the treatment with the recently approved FDA drug, pirfenidone (44.2 % of the patients) (Behr *et al.,* 2015).

5.1.4. Antioxidative response *via* HO-1 in AD-induced pulmonary fibrosis

Since alveolar oxidative stress is resultant of disequilibrium between oxidants and antioxidants (Markart *et al.,* 2009) and an increased ROS production has been demonstrated in AD treated AECs, an initiative was made to analyze the expression of the antioxidative protein, HO-1 under AD treatment. HO-1 is a major inducible antioxidant protein that catalyzes the conversion of heme into biliverdin IXα, carbon monoxide and Fe^{2+} (Donnelly and Barnes, 2001). HO-1 is upregulated in response to a variety of stimuli *viz* free heme, oxidative stress, inflammation, heavy metals, UV radiation and so on (Bindu *et al.,* 2011). HO-1 also forms a major link to autophagy, and depending on the insult, has been reported to

either increase or decrease autophagy in varied pathological conditions (Yun *et al.,* 2014, Lin *et al.,* 2014, Li *et al.,* 2013, Bolisetty *et al.,* 2010, Kim *et al.,* 2008b). In complete agreement with the AD-induced ROS, a substantial increase in the expression of the HO-1 was observed in AD treated mice AECII. In particular, increase in HO-1 protein was evident in the mitochondrial-lysosomal enriched fraction of AD treated MLE12 cells, which implies an increased localization of HO-1 to mitochondria in AECs under AD treatment. This is in line with studies demonstrating translocation of HO-1 to mitochondria under conditions of increased oxidative stress (Bolisetty *et al.,* 2013, Bindu *et al.,* 2011). Further, decreased HO-1 expression was noted in mice AECII upon co-treatment with AD and NAC, which confirms that AD-induced oxidative stress is indeed responsible for the upregulation of HO-1 expression in mice AECII.

With an increased HO-1 expression observed in AD treated AECII, it was considered important to decipher the role of HO-1 and to address if HO-1 is involved in inducing autophagy in AECs upon AD treatment. siRNA mediated knockdown of HO-1 in AECs under AD treatment and chemical inhibition of HO-1 using SnPP in AD treated MLE12 cells and AECII revealed prominent increase in LC3BII levels. This increase in lipidated LC3B upon HO-1 knockdown (or) chemical inhibition of HO-1 indicated a HO-1 independent autophagy in AECs under AD treatment. Although AD-induced antioxidative response *via* HO-1 does not seem to completely avert AD driven macroautophagy, its absence did further aggravate macroautophagy under AD treatment, which might contribute further towards AD-induced apoptosis. Thus, the increased expression of HO-1 in AECs upon AD treatment might be cytoprotective.

The nuclear factor erythroid 2 (NF-E2)-related factor 2 - Kelch-like erythroid cell-derived protein with CNC homology (ECH)-associated protein 1 (Nrf2 - Keap1) signaling pathway is considered as one of the vital cellular defense and survival pathways (Jaramillo and Zhang, 2013). Nrf2 is a transcription factor, which upon translocation to the nucleus upregulates the expression of antioxidant response element (ARE motif) dependent genes like HO-1, in an effort to combat cellular insults such as oxidative stress (Ji *et al.,* 2015). In the absence of oxidative stress, Nrf2 is associated with the E3-ubiquitin ligase, Keap1 and remains inactive in the cytoplasm. Thus, its dissociation from Keap1 activates Nrf2 and facilitates its nuclear translocation. The protein p62 is one of the well known players that can execute this job for Nrf2. Through its KIR domain, p62 can interact with Keap1 and free Nrf2 (Puissant *et al.,* 2012). It is thus possible that the increased HO-1 expression witnessed under AD treatment might be a result of the activation of p62-Nrf2 antioxidative signaling pathway, since AD has

been demonstrated to induce p62 in mice AECII. It is also to be noted that the p62 promoter harbours ARE motif, hence the activation of Nrf2 by p62 drives its own transcription, thereby contributing to the process of induction of a positive feedback loop (Puissant *et al.,* 2012). In line with this, transcriptional upregulation of p62 had been documented in AD treated MLE12 cells (Mahavadi *et al.,* 2015). Although compensatory mechanism for oxidative stress with upregulated expression of Nrf2 and elevated production of low-molecular weight non-enzymatic antioxidants had been demonstrated in IPF patients, they are found to be insufficient to counterbalance the oxidative stress (Markart *et al.,* 2009).

Taken together, the current study demonstrates AD-induced macroautophagy to be anti-survival in AECII and AD-induced oxidative stress to drive aberrant p62-mediated mitophagy, that probably drives AECII apoptosis and thereby into development and progression of AD-induced pulmonary fibrosis.

6. Summary

Amiodarone (AD) is a bi-iodinated benzofuran derivative, classified as Class III anti-arrhythmic drug. Despite its therapeutic potential, AD inflicts several cardiac and extra-cardiac side effects. Being a cationic amphiphilic drug, AD exhibits high lipophilicity. This aids in the accumulation of the drug and its metabolite, N-desethylamiodarone (DEA) in high lipid containing organs *viz* adipose tissue, thyroid, liver, lungs and so on, thereby causing potentially harmful off-target effects. Although AD mediated thyroid and ophthalmic effects are more prevalent, AD-induced pulmonary toxicity (AIPT) is often fatal. Severe pulmonary toxicity has been reported in patients receiving even low doses of AD. Pulmonary fibrosis is one of the most frequently reported manifestations of AIPT. Although the precise molecular mechanism underlying AIPT still remains obscure, interplay between several direct and indirect mechanisms such as cytotoxic insult, immune mediated inflammatory process and angiotensin system activation might contribute towards the development of AIPT. Direct exposure to AD has been shown to induce apoptosis in various mammalian lung cell types including the human alveolar epithelial cells (AECs) *in vitro*. Apoptosis of alveolar epithelial cells (AECII) has been suggested to be a prime factor driving the development of pulmonary fibrosis.

In earlier studies from our group, murine model for AD-induced pulmonary fibrosis had been established and a systematic analysis of the same had revealed prominent alterations in the surfactant homeostasis, increased endoplasmic reticulum (ER) and lysosomal stress alongside with apoptosis of AECII. In line with the increased lysosomal stress, an increase in the number and size of lamellar bodies and LC3B lipidation (macroautophagy marker) and LC3 positive vacuoles were observed in AD treated murine AECII. In continuum, in the current study an effort was made to determine the mechanisms underlying AD-induced apoptosis of AECII, particularly to decipher the role of macroautophagy, whether it is a pro- or anti-survival and then determine autophagy flux in AECs under AD treatment. Since AD is also a potential mitochondrial toxicant, well known to cause mitochondrial dysfunction and generate reactive oxygen species (ROS), further attempt was made to examine if AD promotes mitochondrial autophagy (mitophagy) in murine model of AD-induced pulmonary fibrosis and thereby discern its probable role. In addition, the antioxidative response *via* heme oxygenase-1 (HO-1) and its role has also been investigated.

Since AD significantly increases the expression of cathepsin D in AECII and cathepsin D mediate apoptosis in AECII in the mouse model of Hermansky-Pudlak syndrome associated

lung fibrosis, it was reasonable to speculate the AD-induced AECII apoptosis might be mediated by cathepsin D. siRNA mediated gene silencing of cathepsin D in AD treated MLE12 cells didn't result in a significant decrease in cleaved caspase 3, the terminal apoptotic marker. As AD was found to induce lysosomal biogenesis (evident from prominently increased Lysosomal-associated membrane protein 1 and 2 (LAMP1 and LAMP2) expression in AECs under AD treatment) and increase autophagy flux in MLE12 cells upon treatment with chloroquine, inhibition of the lysosome dependent degradative pathway, macroautophagy was hypothesized to attenuate AD-induced AECII apoptosis. Knockdown of the major macroautophagy protein, LC3B in AD treated MLE12 cells using siRNA resulted in prominent decrease in cleaved caspase 3, indicating the anti-survival role of macroautophagy in AECII upon AD treatment.

Further, being a mitochondrial toxicant, AD was shown to increase ROS production in MLE12 cells, particularly a surge in superoxide ($O_2^{\cdot-}$) radical generation was observed upon AD treatment and a prominent increase in mitochondrial biogenesis, indicated by increased COX IV expression was also noted in AD treated AECII. In addition, AD was demonstrated to increase the expression of p62 (and not that of the other mitophagy markers *viz* BNIP3, BNIP3L and cargo receptor protein, NBR1) in AD treated murine AECII. Furthermore, AD was shown to promote mitophagy *via* AD-induced p62 mediated targeting of mitochondria to autophagosomes and lysosomes, which is evident from the co-localization of p62, ubiquitin.K63 and COX IV with LC3B (autophagosomal marker) and LAMP2/cathepsin D (lysosomal marker). Inhibition of AD-induced mitophagy or ROS in AECs using mdivi-1 and NAC respectively yielded substantial decrease in LC3B lipidation. In addition, reduction in annexinV (apoptotic marker) staining was documented in AD treated MLE12 cells following mdivi-1 treatment. As a result of AD-induced oxidative stress, a significant increase in the expression of antioxidative protein, HO-1 was recorded in AD treated murine AECII and the knockdown analysis using HO-1siRNA in MLE12 cells revealed AD-induced autophagy to be HO-1 independent.

Collectively, the present study demonstrates that a) AD-induced AECII apoptosis is LC3B dependent and thus AD-induced macroautophagy is anti-survival in AECII b) AD increases oxidative stress and drives aberrant mitophagy *via* p62 resulting in AECII apoptosis c) AD-induced autophagy is HO-1 independent.

7. Zusammenfassung

Amiodaron (AD) ist ein bi-iodiniertes Benzofuran-Derivat welches als Klasse-III Antiarrhythmikum klassifiziert ist. Trotz des therapeutischen Potentials weist AD mehrere Nebenwirkungen innerhalb und außerhalb des Herz-Kreislaufs auf.Als kationisches amphiphiles Molekül ist AD hoch lipophil. Dies führt zur Anreichunerung des Moleküls und seines Metabolits, N-Desethylamiodaron (DEA) in Organen mit hohem Lipid-Anteil wie unter anderem Adiposem Gewebe, Schilddrüse, Leber und Lunge, welches potentiell schädliche Nebenwirkungen verursacht. Obwohl AD-vermittelte Effekte auf Schilddrüse und Sehorgane häufiger auftreten, ist AD verursachte Lungen-Toxizität (AIPT) häufig tödlich. Selbst in Patienten die nur geringe Mengen von AD zu sich genommen haben, wurde von schwerer Lungen-Toxizität berichtet.Lungenfibrose ist eine der am häufigsten gemeldeten Symptome von AIPT. Obwohl der genaue molekulare Mechanismus von AIPT noch unbekannt ist, kann die Entwicklung von AIPT durch Zusammenspiel von mehreren direkten und indirekten Mechanismen wie zytotoxische Schädigung, Immunsystem-basierte Entzündungsprozesse und Aktivierung des Angiotensin-Systems unterstützt werden. Es wurde gezeigt, dass direkte Exposition von AD in verschiedenen Säugetier-Lungen-Zelltypen wie humanen alveolaren Epithelzellen (AECs) in vitro Apoptose auslösen kann. Apoptose der alveolaren Epithelzellen (AECII) gilt als einer der wichtigsten Faktoren für die Entwicklung der Lungenfibrose.

In vorrangehenden Studien unserer Forschungsgruppe wurde ein Mausmodell für AD-induzierte Lungenfibrose etabliert. Systematische Analyse offenbarte prominente Veränderungen in der Tensid Homeostase, erhöhter Stress im endoplasmatischen Retikulum und in Lysosomen in Verbindung mit Apoptose der AECII. Im Einklang mit dem erhöhten lysosomalen Stress wurde auch ein Anstieg in der Anzahl und Größe der Lamellarkörpern und LC3B Lipidation (ein Makroautophagie-Marker) und der LC3-positiven Vakuolen in AD-behandelten murinen AECII entdeckt. Als Fortführung dieser Arbeit wurde in der aktuellen Studie versucht den Mechanismus der AD-induzierten Apoptose in AECII aufzudecken. Inbesondere war das Ziel die Rolle der Makroautophagie, entweder als Pro- oder Anti-Überlebensfaktor, zu entschlüsseln und den autophagischen Fluss in AECs unter AD Behandlung zu bestimmen. Da AD potentiell toxisch für Mitochondrien ist, bekannt dafür mitochondriale Funktionsstörungen zu verursachen und reaktive Sauerstoffspezies (ROS) zu generieren, wurde weiterhin versucht aufzuklären ob AD mitochondriale Autophagie (Mitophagie) im Mausmodell der AD-induzierten Lungenfibrose fördert.

Zusätzlich wurde die Rolle der antioxidativen Antwort über Heme Oxygenase-1 (HO-1) erforscht.

Da AD die Expression von Cathepsin D in AECII signifikant erhöht und da Cathepsin D Apoptose von AECII im Mausmodell der Hermansky-Pudlak Syndroms assoziierten Lungenfibrose vermittelt, lag die Vermutung nahe, dass AD-induzierte AECII Apoptose durch Cathepsin D vermittelt wird. Gen-Stilllegung von Cathepsin D durch siRNA in AD behandelten MLE12 Zellen führte zu keiner signifikanten Verringerung der Spaltung von Caspase 3, dem terminalen Marker der Apoptose. Da entdeckt wurde, dass AD Biogenese der Lysosomen induziert (offensichtlich durch erhöhte Expression von Lyosomal-associated membrane protein 1 und 2 (LAMP1 und LAMP2) in AECs nach Behandlung mit AD) und den autophagischen Fluss in MLE12 Zellen nach Behandlung mit Chloroquine erhöhte, ein Inhibitor des Lysosom-abhängigen zersetzenden Signalwegs, wurde angenommen, dass Makroautophagie AD-induzierte AECII Apoptose reduziert. Herrunterregulieren des wichtigsten Makroautophagie-Proteins, LC3B, in AD-behandelten MLE12 Zellen mittels siRNA resultierte in prominenter Verringerung der Spaltung von Caspase 3 und zeigte somit die Anti-Überlebensrolle der Makroautophagie in AECII nach AD Behandlung. Weiterhin, da AD als toxisch für Mitochondrien bekannt ist, wurde gezeigt, dass AD ROS Produktion in MLE12 Zellen erhöht, inbesondere Generierung von Superoxid (O2-) nach Behandlung mit AD und eine Erhöhung mitochondrialer Biogenese wurde beobachtet, angezeigt durch erhöhte COX IV Expression in AD-behandelten AECII.

Zusätzlich wurde gezeigt dass AD die Expression von p62 (und nicht die der anderen Mitophagie Marker BNIP3, BNIP3L und Cargo Receptor Protein, NBR1) in AD-behandelten murinen AECII erhöhte. Weiterhin wurde gezeigt dass AD Mitophagie über AD-induziertes p62-vermitteltes Zielen der Mitochondrien zu Autophagosomen und Lysosomen verursacht, offensichtlich durch Kolokalisierung von p62, Ubiquitin K63 und COX IV mit LC3B (Autophagosomaler Marker) und LAMP2/Cathepsin D (Lysosomaler Marker). Inhibierung der AD-induzierten Mitophagie oder ROS in AECs mittels mdivi-1 und NAC führte zu substantieller Verringerung der LC3B Lipidation Expression. Zusätzlich wurde Reduktion in der AnnexinV-Färbung (Apoptose Marker) in AD-behandelten MLE12 Zellen nach mdivi-1 Behandlung festgestellt. Als Resultat des AD-induzierten oxidativen Stresses wurde ein signifikanter Anstieg der Expression des antioxidativen Proteins, HO-1, in AD-behandelten murinen AECII entdeckt und in einer Gen-Stilllegungsanalyse mit HO-1 siRNA gezeigt, dass in MLE12 Zellen AD-induzierte Autophagie HO-1 unabhängig ist.

Zusammengefasst zeigt die aktuelle Studie, dass a) AD-induzierte AECII Apoptose LC3B-abhängig ist und damit AD-induzierte Makroautophagie einen Anti-Überlebensfaktor für AECII darstellt, b) AD den oxidativen Stress erhöht und anomale Mitophagie mittels p62 antreibt was in AECII Apoptose resultiert, c) AD-induzierte Autophagie HO-1 unabhängig ist.

8. Appendix

8.1. List of primary antibodies

Name	Source	Dilution	Purpose	Company
Annexin V	Rabbit	1:50	IF	Abcam
ATG12-ATG5	Rabbit	1:1000	WB	Abcam
ATG7	Rabbit	1:1000	WB	Sigma-Aldrich
ATG7	Rabbit	1:500	IHC	Sigma-Aldrich
b-actin	Rabbit	1:30000	WB	Abcam
BNIP3	Rabbit	1:1000	WB	Abcam
BNIP3L	Rabbit	1:1000	WB	Cell signalling
CathepsinD	Goat	1:500	WB	R&D Systems
CathepsinD	Goat	1:100	IF	R&D Systems
Cleaved caspase 3	Rabbit	1:1000	WB	Cell signalling
COX IV	Rabbit	1:1000	WB	Cell signalling
COX IV	Rabbit	1:100	IHC	Cell signalling
COX IV	Rabbit	1:100	IF	Cell signalling
GAPDH	Rabbit	1:1000	WB	Abcam
HO-1	Rabbit	1:500	WB	Enzo lifesciences
HO-1	Rabbit	1:200	IHC	Enzo lifesciences
LAMP1	Rat	1:1000	WB	Santa Cruz
LAMP1	Rat	1:25	IF	Santa Cruz
LAMP2	Rat	1:1000	WB	Millipore
LAMP2	Rat	1:25	IF	Millipore
LC3B	Rabbit	1:1000	WB	Abcam
LC3B	Rabbit	1:100	IF	Abcam
LC3B	Goat	1:25	IF	Santa Cruz
NBR1	Rabbit	1:1000	WB	Proteintech
NBR1	Rabbit	1:100	IF	Proteintech
p62	Rabbit	1:10000	WB	Sigma-Aldrich
p62	Rabbit	1:100	IF	Sigma-Aldrich
p62	Rabbit	1:200	IHC	Sigma-Aldrich
proSp-C	Rabbit	1:500	WB	Millipore
proSp-C	Rabbit	1:50	IF	Millipore

proSp-C	Rabbit	1:500	IHC	Millipore
Ubiquitin.lysine 63 specific	Rabbit	1:25	IF	Millipore

WB:Western blotting, IHC:Immunohistochemistry, IF:Immunofluorescence

8.2. List of secondary antibodies

Name	Source	Dilution	Company
Anti-rabbit	Swine	1:2000	Dako
Anti-goat	Rabbit	1:2000	Dako
Anti-rat	Rabbit	1:2000	Dako

8.3. List of fluorescent labelled secondary antibodies

Name	Dilution	Company
Donkey anti-Rabbit IgG (H+L) Secondary Antibody, Alexa Fluor® 488 conjugate	1:400	Life technologies
Donkey anti-Rabbit IgG (H+L) Secondary Antibody, Alexa Fluor® 555 conjugate	1:400	Life technologies
Donkey anti-Rat IgG (H+L) Secondary Antibody, Alexa Fluor® 488 conjugate	1:400	Life technologies
Donkey anti-Goat IgG (H+L) Secondary Antibody, Alexa Fluor® 488 conjugate	1:400	Life technologies

9. References

1. Adesse D, Azzam EM, Meirelles Mde N, Urbina JA, Garzoni LR, **2011**, Amiodarone inhibits Trypanosoma cruzi infection and promotes cardiac cell recovery with gap junction and cytoskeleton reassembly in vitro, *Antimicrob Agents Chemother*, 55(1):203-10.

2. American Thoracic Society; European Respiratory Society. American Thoracic Society/European Respiratory Society International Multidisciplinary Consensus Classification of the Idiopathic Interstitial Pneumonias. This joint statement of the American Thoracic Society (ATS), and the European Respiratory Society (ERS) was adopted by the ATS board of directors, June 2001 and by the ERS Executive Committee, June 2001, **2002**, *Am J Respir Crit Care Med*. 165:277-304.

3. Alder JK, Chen JJ, Lancaster L, Danoff S, Su SC, Cogan JD, Vulto I, Xie M, Qi X, Tuder RM, Phillips JA 3rd, Lansdorp PM, Loyd JE, Armanios MY, **2008**, Short telomeres are a risk factor for idiopathic pulmonary fibrosis. *Proc Natl Acad Sci U S A*. 105:13051-6.

4. Anthérieu S, Rogue A, Fromenty B, Guillouzo A, Robin MA, **2011**, Induction of vesicular steatosis by amiodarone and tetracycline is associated with up-regulation of lipogenic genes in HepaRG cells, *Hepatology*, 53:1895-905.

5. Ashrafi G, Schwarz TL, **2013**, The pathways of mitophagy for quality control and clearance of mitochondria, *Cell Death Differ*, 20:31-42.

6. Barbas-Filho JV, Ferreira MA, Sesso A, Kairalla RA, Carvalho CR, Capelozzi VL, **2001**, Evidence of type II pneumocyte apoptosis in the pathogenesis of idiopathic pulmonary fibrosis (IFP)/usual interstitial pneumonia (UIP), *J Clin Pathol*, 54:132-8.

7. Bargout R, Jankov A, Dincer E, Wang R, Komodromos T, Ibarra-Sunga O, Filippatos G, Uhal BD, **2000**, Amiodarone induces apoptosis of human and rat alveolar epithelial cells in vitro, *Am J Physiol Lung Cell Mol Physiol*, 278:L1039-44.

8. Baritussio A, Marzini S, Agostini M, Alberti A, Cimenti C, Bruttomesso D, Manzato E, Quaglino D, Pettenazzo A, **2001**, Amiodarone inhibits lung degradation of SP-A and perturbs the distribution of lysosomal enzymes, *Am J Physiol Lung Cell Mol Physiol*, 281:L1189-99.

9. Bedrossian CW, Warren CJ, Ohar J, Bhan R, **1997**, Amiodarone pulmonary toxicity: cytopathology, ultrastructure, and immunocytochemistry. *Ann Diagn Pathol,* 1:47-56.

10. Begriche K, Igoudjil A, Pessayre D, Fromenty B, **2006**, Mitochondrial dysfunction in NASH: causes, consequences and possible means to prevent it, *Mitochondrion*, 6:1-28.

11. Behr J, Kreuter M, Hoeper MM, Wirtz H, Klotsche J, Koschel D, Andreas S, Claussen M, Grohé C, Wilkens H, Randerath W, Skowasch D, Meyer FJ, Kirschner J, Gläser S, Herth FJ, Welte T, Huber RM, Neurohr C, Schwaiblmair M, Kohlhäufl M, Höffken G, Held M, Koch A, Bahmer T, Pittrow D, **2015**, Management of patients with idiopathic

pulmonary fibrosis in clinical practice: the INSIGHTS-IPF registry, *Eur Respir J*. pii: ERJ-02176-2014. [Epub ahead of print]

12. Bindu S, Pal C, Dey S, Goyal M, Alam A, Iqbal MS, Dutta S, Sarkar S, Kumar R, Maity P, Bandyopadhyay U, **2011**, Translocation of heme oxygenase-1 to mitochondria is a novel cytoprotective mechanism against non-steroidal anti-inflammatory drug-induced mitochondrial oxidative stress, apoptosis, and gastric mucosal injury, *J Biol Chem*. 286:39387-402.

13. Birkelbach B, Lutz D, Ruppert C, Henneke I, Lopez-Rodriguez E, Günther A, Ochs M, Mahavadi P, Knudsen L, **2015**, Linking progression of fibrotic lung remodeling and ultrastructural alterations of alveolar epithelial type II cells in the amiodarone mouse model. *Am J Physiol Lung Cell Mol Physiol*. 309:L63-75.

14. Bolisetty S, Traylor A, Zarjou A, Johnson MS, Benavides GA, Ricart K, Boddu R, Moore RD, Landar A, Barnes S, Darley-Usmar V, Agarwal A, **2013**, Mitochondria-targeted heme oxygenase-1 decreases oxidative stress in renal epithelial cells, *Am J Physiol Renal Physiol*, 305:F255-64.

15. Bolisetty S, Traylor AM, Kim J, Joseph R, Ricart K, Landar A, Agarwal A, **2010**, Heme oxygenase-1 inhibits renal tubular macroautophagy in acute kidney injury, *J Am Soc Nephrol*, 21:1702-12.

16. Bolt MW, Card JW, Racz WJ, Brien JF, Massey TE, **2001**, Disruption of mitochondrial function and cellular ATP levels by amiodarone and N-desethylamiodarone in initiation of amiodarone-induced pulmonary cytotoxicity, *J Pharmacol Exp Ther*, 298:1280-9.

17. Bueno M, Lai YC, Romero Y, Brands J, St Croix CM, Kamga C, Corey C, Herazo-Maya JD, Sembrat J, Lee JS, Duncan SR, Rojas M, Shiva S, Chu CT, Mora AL, **2015**, PINK1 deficiency impairs mitochondrial homeostasis and promotes lung fibrosis. *J Clin Invest*. 125:521-38.

18. Cantin AM, Hubbard RC, Crystal RG, **1989**, Glutathione deficiency in the epithelial lining fluid of the lower respiratory tract in idiopathic pulmonary fibrosis, *Am Rev Respir Dis*, 139:370-2.

19. Card JW, Lalonde BR, Rafeiro E, Tam AS, Racz WJ, Brien JF, Bray TM, Massey TE, **1998**, Amiodarone-induced disruption of hamster lung and liver mitochondrial function: lack of association with thiobarbituric acid-reactive substance production, *Toxicol Lett*, 98:41-50.

20. Chang SN, Hwang JJ, Hsu KL, Tsai CT, Lai LP, Lin JL, Tseng CD, Chiang FT, **2007**, Amiodarone-related pneumonitis, *J Formos Med Assoc*, 106:411-7.

21. Chen PM, Gombart ZJ, Chen JW, **2011**, Chloroquine treatment of ARPE-19 cells leads to lysosome dilation and intracellular lipid accumulation: possible implications of lysosomal dysfunction in macular degeneration, *Cell Biosci*, 1:10.

22. Chen ZH, Lam HC, Jin Y, Kim HP, Cao J, Lee SJ, Ifedigbo E, Parameswaran H, Ryter SW, Choi AM, **2010**, Autophagy protein microtubule-associated protein 1 light chain-3B (LC3B) activates extrinsic apoptosis during cigarette smoke-induced emphysema, *Proc Natl Acad Sci U S A*, 107:18880-5.

23. Cheresh P, Morales-Nebreda L, Kim SJ, Yeldandi A, Williams DB, Cheng Y, Mutlu GM, Budinger GR, Ridge K, Schumacker PT, Bohr VA, Kamp DW, **2015**, Asbestos-induced pulmonary fibrosis is augmented in 8-oxoguanine DNA glycosylase knockout mice. *Am J Respir Cell Mol Biol*. 52:25-36.

24. Chung MJ, Lee KS, Franquet T, Müller NL, Han J, Kwon OJ, **2005**, Metabolic lung disease: imaging and histopathologic findings. *Eur J Radiol*, 54:233-45.

25. Chung WH, Bennett BM, Racz WJ, Brien JF, Massey TE, **2001**, Induction of c-jun and TGF-beta 1 in Fischer 344 rats during amiodarone-induced pulmonary fibrosis, *Am J Physiol Lung Cell Mol Physiol*, 281:L1180-L1188.

26. Coward WR, Saini G, Jenkins G, **2010**, The pathogenesis of idiopathic pulmonary fibrosis, *Ther Adv Respir Dis,* 4:367-88.

27. Day BJ, **2008**, Antioxidants as potential therapeutics for lung fibrosis. *Antioxid Redox Signal*, 10:355-70.

28. De Macedo-Silva ST, de Oliveira Silva TL, Urbina JA, de Souza W, Rodrigues JC, **2011**, Antiproliferative, Ultrastructural, and Physiological Effects of Amiodarone on Promastigote and Amastigote Forms of Leishmania amazonensis, *Mol Biol Int*, 2011:876021.

29. Dharmarajan TS, Shah AB, Dharmarajan L, **2008**, Amiodarone-induced pulmonary toxicity: potentially fatal, recognize early during life, *J Am Geriatr Soc*, 56:1363-5.

30. Ding WX, Yin XM, **2012**, Mitophagy: mechanisms, pathophysiological roles, and analysis, *Biol Chem*, 393:547-64.

31. Donnelly LE, Barnes PJ, **2001**, Expression of heme oxygenase in human airway epithelial cells, *Am J Respir Cell Mol Biol*, 24:295-303.

32. Durukan AB, Erdem B, Durukan E, Sevim H, Karaduman T, Gurbuz HA, Gurpinar A, Yorgancioglu C, **2012**, May toxicity of amiodarone be prevented by antioxidants? A cell-culture study, *J Cardiothorac Surg*, 7:61.

33. Ernawati DK, Stafford L, Hughes JD, **2008**, Amiodarone-induced pulmonary toxicity. *Br J Clin Pharmaco,* 66:82-7.

34. Eskelinen EL, **2006**, Roles of LAMP-1 and LAMP-2 in lysosome biogenesis and autophagy. Mol Aspects Med, 27:495-502.

35. Felser A, Blum K, Lindinger PW, Bouitbir J, Krähenbühl S, **2013**, Mechanisms of hepatocellular toxicity associated with dronedarone-a comparison to amiodarone, *Toxicol Sci*, 131:480-90.

36. Feng Y, He D, Yao Z, Klionsky DJ, **2014**, The machinery of macroautophagy, *Cell Res,* 24:24-41.

37. Fromenty B, Fisch C, Berson A, Letteron P, Larrey D, Pessayre D, **1990a**, Dual effect of amiodarone on mitochondrial respiration. Initial protonophoric uncoupling effect followed by inhibition of the respiratory chain at the levels of complex I and complex II, *J Pharmacol Exp Ther*, 255:1377-84.

38. Fromenty B, Fisch C, Labbe G, Degott C, Deschamps D, Berson A, Letteron P, Pessayre D, **1990b**, Amiodarone inhibits the mitochondrial beta-oxidation of fatty acids and produces microvesicular steatosis of the liver in mice, *J Pharmacol Exp Ther*, 255:1371-6.

39. Fu M, St-Pierre P, Shankar J, Wang PT, Joshi B, Nabi IR, **2013**, Regulation of mitophagy by the Gp78 E3 ubiquitin ligase, *Mol Biol Cell*, 24:1153-62.

40. Funk RS, Krise JP, **2012**, Cationic amphiphilic drugs cause a marked expansion of apparent lysosomal volume: implications for an intracellular distribution-based drug interaction, *Mol Pharm*, 9:1384-95.

41. Galindo MF, Jordán J, González-García C, Ceña V, **2003**, Reactive oxygen species induce swelling and cytochrome c release but not transmembrane depolarization in isolated rat brain mitochondria, *Br J Pharmacol*, 139:797-804.

42. Geisler S, Holmström KM, Skujat D, Fiesel FC, Rothfuss OC, Kahle PJ, Springer W, **2010**, PINK1/Parkin-mediated mitophagy is dependent on VDAC1 and p62/SQSTM1, *Nat Cell Biol*, 12:119-31.

43. Gomes LC, Scorrano L, **2013**, Mitochondrial morphology in mitophagy and macroautophagy, *Biochim Biophys Acta*, 1833:205-12.

44. Günther A, Korfei M, Mahavadi P, von der Beck D, Ruppert C, Markart P, **2012**, Unravelling the progressive pathophysiology of idiopathic pulmonary fibrosis, *Eur Respir Rev*, 21:152-60.

45. Hanna RA, Quinsay MN, Orogo AM, Giang K, Rikka S, Gustafsson ÅB, **2012**, Microtubule-associated protein 1 light chain 3 (LC3) interacts with Bnip3 protein to selectively remove endoplasmic reticulum and mitochondria via autophagy, *J Biol Chem*, 287:19094-104.

46. Hawkins A, Guttentag SH, Deterding R, Funkhouser WK, Goralski JL, Chatterjee S, Mulugeta S, Beers MF, **2015**, A non-BRICHOS SFTPC mutant (SP-CI73T) linked to

interstitial lung disease promotes a late block in macroautophagy disrupting cellular proteostasis and mitophagy, *Am J Physiol Lung Cell Mol Physiol*, 308:L33-47.

47. Hellebrand EE, Varbiro G, **2010**, Development of mitochondrial permeability transition inhibitory agents: a novel drug target, *Drug Discov Ther*, 4:54-61.

48. Hostetler KY, Giordano JR, Jellison EJ, **1988**, *In vitro* inhibition of lysosomal phospholipase A1 of rat lung by amiodarone and desethylamiodarone, *Biochim Biophys Acta*, 959:316-21.

49. Jaramillo MC, Zhang DD, **2013**, The emerging role of the Nrf2-Keap1 signaling pathway in cancer, *Genes Dev*, 27:2179-91.

50. Jarand J, Lee A, Leigh R, **2007**, Amiodaronoma: an unusual form of amiodarone-induced pulmonary toxicity, *CMAJ*, 176:1411-3.

51. Ji LL, Sheng YC, Zheng ZY, Shi L, Wang ZT, **2015**, The involvement of p62-Keap1-Nrf2 antioxidative signaling pathway and JNK in the protection of natural flavonoid quercetin against hepatotoxicity, *Free Radic Biol Med*, pii:S0891-5849(15)00159-8.

52. Johansen T, Lamark T, **2011**, Selective autophagy mediated by autophagic adapter proteins, *Autophagy*, 7:279-96.

53. Kanoh S, Kobayashi H, Motoyoshi K, **2005**, Exhaled ethane: an in vivo biomarker of lipid peroxidation in interstitial lung diseases, *Chest*. 128:2387-92.

54. Kaufmann P, Török M, Hänni A, Roberts P, Gasser R, Krähenbühl S, **2005**, Mechanisms of benzarone and benzbromarone-induced hepatic toxicity, *Hepatology*, 41:925-35.

55. Kim PK, Hailey DW, Mullen RT, Lippincott-Schwartz J, **2008a**, Ubiquitin signals autophagic degradation of cytosolic proteins and peroxisomes, *Proc Natl Acad Sci U S A*, 105:20567-74.

56. Kim HP, Wang X, Chen ZH, Lee SJ, Huang MH, Wang Y, Ryter SW, Choi AM, **2008b**, Autophagic proteins regulate cigarette smoke-induced apoptosis: protective role of heme oxygenase-1, *Autophagy*, 4:887-95.

57. Kinnula VL, **2008**, Redox imbalance and lung fibrosis, *Antioxid Redox Signal*, 10:249-52.

58. Kinnula VL, Hodgson UA, Lakari EK, Tan RJ, Sormunen RT, Soini YM, Kakko SJ, Laitinen TH, Oury TD, Pääkkö PK, **2006**, Extracellular superoxide dismutase has a highly specific localization in idiopathic pulmonary fibrosis/usual interstitial pneumonia, *Histopathology*, 49:66-74.

59. Kirkin V, McEwan DG, Novak I, Dikic I, **2009**, A role for ubiquitin in selective autophagy, *Mol Cell*, 34:259-69.

60. Klionsky DJ, Abdalla FC, Abeliovich H, *et al.,* **2012**, Guidelines for the use and interpretation of assays for monitoring autophagy, *Autophagy*, 8:445-544.

61. Korfei M, Ruppert C, Mahavadi P, Henneke I, Markart P, Koch M, Lang G, Fink L,Bohle RM, Seeger W, Weaver TE, Guenther A, **2008**, Epithelial endoplasmic reticulum stress and apoptosis in sporadic idiopathic pulmonary fibrosis, *Am J Respir Crit Care Med*, 178:838-46.

62. Korolchuk VI, Menzies FM, Rubinsztein DC, **2010**, Mechanisms of cross-talk between the ubiquitin-proteasome and autophagy-lysosome systems, *FEBS Lett*. 584(7):1393-8.

63. Kubli DA, Gustafsson ÅB, **2012**, Mitochondria and mitophagy: the yin and yang of cell death control, *Circ Res*, 111:1208-21.

64. Lee HC, Yin PH, Chi CW, Wei YH, **2002**, Increase in mitochondrial mass in human fibroblasts under oxidative stress and during replicative cell senescence, *J Biomed Sci*, 9:517-26.

65. Lee HC, Yin PH, Lu CY, Chi CW, Wei YH, **2000**, Increase of mitochondria and mitochondrial DNA in response to oxidative stress in human cells, *Biochem J*, 348:425-32.

66. Lee JY, Nagano Y, Taylor JP, Lim KL, Yao TP, **2010**, Disease-causing mutations in parkin impair mitochondrial ubiquitination, aggregation, and HDAC6-dependent mitophagy, *J Cell Biol*, 189:671-9.

67. Lee KY, Oh S, Choi YJ, Oh SH, Yang YS, Yang MJ, Lee K, Lee BH, **2013**, Activation of autophagy rescues amiodarone-induced apoptosis of lung epithelial cells and pulmonary toxicity in rats, *Toxicol Sci*, 136:193-204.

68. Lee TS, Chau LY, **2002**, Heme oxygenase-1 mediates the anti-inflammatory effect of interleukin-10 in mice, *Nat Med*, 8:240-246.

69. Lenz AG, Costabel U, Maier KL, **1996**, Oxidized BAL fluid proteins in patients with interstitial lung diseases, *Eur Respir J*, 9:307-12.

70. Li CW, Lin YF, Liu TT, Wang JY, **2013**, Heme oxygenase-1 aggravates heat stress-induced neuronal injury and decreases autophagy in cerebellar Purkinje cells of rats, *Exp Biol Med (Maywood)*, 238:744-54.

71. Lin CW, Chen YS, Lin CC, Chen YJ, Lo GH, Lee PH, Kuo PL, Dai CY, Huang JF, Chung WL, Yu ML, **2015**, Amiodarone as an autophagy promoter reduces liver injury and enhances liver regeneration and survival in mice after partial hepatectomy. *Sci Rep*. 5:15807.

72. Lin TK, Chen SD, Chuang YC, Lin HY, Huang CR, Chuang JH, Wang PW, Huang ST, Tiao MM, Chen JB, Liou CW, **2014**, Resveratrol partially prevents rotenone-induced neurotoxicity in dopaminergic SH-SY5Y cells through induction of heme oxygenase-1 dependent autophagy, *Int J Mol Sci*, 15:1625-46.

73. Liu G, Cheresh P, Kamp DW, **2013**, Molecular basis of asbestos-induced lung disease. *Annu Rev Pathol*. 8:161-87.

74. Liu JM, Yi Z, Liu SZ, Chang JH, Dang XB, Li QY, Zhang YL, **2015**, The mitochondrial division inhibitor mdivi-1 attenuates spinal cord ischemia-reperfusion injury both in vitro and in vivo: Involvement of BK channels, *Brain Res*, pii: S0006-8993(15)00230-9.

75. Liu L, Feng D, Chen G, Chen M, Zheng Q, Song P, Ma Q, Zhu C, Wang R, Qi W, Huang L, Xue P, Li B, Wang X, Jin H, Wang J, Yang F, Liu P, Zhu Y, Sui S, Chen Q, **2012**, Mitochondrial outer-membrane protein FUNDC1 mediates hypoxia-induced mitophagy in mammalian cells, *Nat Cell Biol*, 14:177-85.

76. Mahavadi P, Korfei M, Henneke I, Liebisch G, Schmitz G, Gochuico BR, Markart P, Bellusci S, Seeger W, Ruppert C, Guenther A, **2010**, Epithelial stress and apoptosis underlie Hermansky-Pudlak syndrome-associated interstitial pneumonia, *Am J Respir Crit Care Med*, 182:207-19.

77. Mahavadi P, Henneke I, Ruppert C, Knudsen L, Venkatesan S, Liebisch G,Chambers RC, Ochs M, Schmitz G, Vancheri C, Seeger W, Korfei M, Guenther A, **2014**, Altered surfactant homeostasis and alveolar epithelial cell stress in amiodarone-induced lung fibrosis, *Toxicol Sci*, 142:285-97.

78. Mahavadi P, Knudsen L, Venkatesan S, Henneke I, Hegermann J, Wrede C, Ochs M, Ahuja S, Chillappagari S, Ruppert C, Seeger W, Korfei M, Guenther A, **2015**, Regulation of macroautophagy in amiodarone induced pulmonary fibrosis, *Journal of pathology: clinical research*, I:252-263.

79. Marceau F, Bawolak MT, Lodge R, Bouthillier J, Gagné-Henley A, Gaudreault RC, Morissette G, **2012**, Cation trapping by cellular acidic compartments: beyond the concept of lysosomotropic drugs, *Toxicol Appl Pharmacol*, 259:1-12.

80. Marceau F, Roy C, Bouthillier J, **2014**, Assessment of cation trapping by cellular acidic compartments, *Methods Enzymol*, 534:119-31.

81. Markart P, Luboeinski T, Korfei M, Schmidt R, Wygrecka M, Mahavadi P, Mayer K, Wilhelm J, Seeger W, Guenther A, Ruppert C, **2009**, Alveolar oxidative stress is associated with elevated levels of nonenzymatic low-molecular-weight antioxidants in patients with different forms of chronic fibrosing interstitial lung diseases, *Antioxid Redox Signal*, 11:227-40.

82. Mizumura K, Cloonan SM, Nakahira K, Bhashyam AR, Cervo M, Kitada T, Glass K, Owen CA, Mahmood A, Washko GR, Hashimoto S, Ryter SW, Choi AM, **2014**, Mitophagy-dependent necroptosis contributes to the pathogenesis of COPD, *J Clin Invest*, 124:3987-4003.

83. Montuschi P, Ciabattoni G, Paredi P, Pantelidis P, du Bois RM, Kharitonov SA, Barnes PJ, **1998**, 8-Isoprostane as a biomarker of oxidative stress in interstitial lung diseases. *Am J Respir Crit Care Med*, 158:1524-7.

84. Morissette G, Ammoury A, Rusu D, Marguery MC, Lodge R, Poubelle PE, Marceau F, **2009**, Intracellular sequestration of amiodarone: role of vacuolar ATPase and macroautophagic transition of the resulting vacuolar cytopathology, *Br J Pharmacol*, 157:1531-40.

85. Mudalel ML, Dave KP, Hummel JP, Solga SF, **2015**, N-acetylcysteine treats intravenous amiodarone induced liver injury, *World J Gastroenterol*, 21:2816-9.

86. Muqit MM, Abou-Sleiman PM, Saurin AT, Harvey K, Gandhi S, Deas E, Eaton S, Payne Smith MD, Venner K, Matilla A, Healy DG, Gilks WP, Lees AJ, Holton J, Revesz T, Parker PJ, Harvey RJ, Wood NW, Latchman DS, **2006**, Altered cleavage and localization of PINK1 to aggresomes in the presence of proteasomal stress, *J Neurochem*, 98:156-69.

87. Myers JL, Katzenstein AL, **1998**, Epithelial necrosis and alveolar collapse in the pathogenesis of usual interstitial pneumonia. *Chest*, 94(6): 1309-1311.

88. Narendra D, Kane LA, Hauser DN, Fearnley IM, Youle RJ, **2010**, p62/SQSTM1 is required for Parkin-induced mitochondrial clustering but not mitophagy; VDAC1 is dispensable for both, *Autophagy*, 6(8):1090-106.

89. Narendra D, Tanaka A, Suen DF, Youle RJ, **2008**, Parkin is recruited selectively to impaired mitochondria and promotes their autophagy, *J Cell Biol*, 183:795-803.

90. Nicolescu AC, Ji Y, Comeau JL, Hill BC, Takahashi T, Brien JF, Racz WJ, Massey TE, **2008**, Direct mitochondrial dysfunction precedes reactive oxygen species production in amiodarone-induced toxicity in human peripheral lung epithelial HPL1A cells, *Toxicol Appl Pharmacol*, 227:370-9.

91. Nikaido A, Tada T, Nakamura K, Murakami M, Banba K, Nishii N, Fuke S, Nagase S, Sakuragi S, Morita H, Ohe T, Kusano KF, **2010**, Clinical features of and effects of angiotensin system antagonists on amiodarone-induced pulmonary toxicity, *Int J Cardiol*, 140:328-35.

92. Okatsu K, Saisho K, Shimanuki M, Nakada K, Shitara H, Sou YS, Kimura M, Sato S, Hattori N, Komatsu M, Tanaka K, Matsuda N, **2010**, p62/SQSTM1 cooperates with Parkin for perinuclear clustering of depolarized mitochondria, *Genes Cells*, 15:887-900.

93. Olshansky B, Sami M, Rubin A, Kostis J, Shorofsky S, Slee A, Greene HL; NHLBI AFFIRM Investigators, 2005, Use of amiodarone for atrial fibrillation in patients with preexisting pulmonary disease in the AFFIRM study. *Am J Cardiol,* 95:404-5.

94. Onoue S, Tsuda Y, **2006**, Analytical studies on the prediction of photosensitive/phototoxic potential of pharmaceutical substances, *Pharm Res*, 23:156-64.

95. Otsuka M, Takahashi H, Shiratori M, Chiba H, Abe S, **2004**, Reduction of bleomycin induced lung fibrosis by candesartan cilexetil, an angiotensin II type 1 receptor antagonist, *Thorax*, 59:31-8.

96. Ott MC, Khoor A, Leventhal JP, Paterick TE, Burger CD, **2003**, Pulmonary toxicity in patients receiving low-dose amiodarone, *Chest*, 123:646-51.

97. Otterbein LE, Soares MP, Yamashita K, Bach FH, **2003**, Heme oxygenase-1: unleashing the protective properties of heme, *Trends Immunol*, 24:449-55.

98. Palikaras K, Tavernarakis N, **2014**, Mitochondrial homeostasis: the interplay between mitophagy and mitochondrial biogenesis, *Exp Gerontol*, 56:182-8.

99. Papiris SA, Triantafillidou C, Kolilekas L, Markoulaki D, Manali ED, **2010**, Amiodarone: review of pulmonary effects and toxicity, *Drug Saf*, 33:539-58.

100. Park J, Lee SB, Lee S, Kim Y, Song S, Kim S, Bae E, Kim J, Shong M, Kim JM, Chung J, **2006**, Mitochondrial dysfunction in Drosophila PINK1 mutants is complemented by parkin, *Nature*, 441:1157-61.

101. Park S, Choi SG, Yoo SM, Son JH, Jung YK, **2014**, Choline dehydrogenase interacts with SQSTM1/p62 to recruit LC3 and stimulate mitophagy, *Autophagy*, 10:1906-20.

102. Patel AS, Song JW, Chu SG, Mizumura K, Osorio JC, Shi Y, El-Chemaly S, Lee CG, Rosas IO, Elias JA, Choi AM, Morse D, **2015**, Epithelial cell mitochondrial dysfunction and PINK1 are induced by transforming growth factor-beta1 in pulmonary fibrosis. *PLoS One*, 10(3):e0121246.

103. Psathakis K, Mermigkis D, Papatheodorou G, Loukides S, Panagou P, Polychronopoulos V, Siafakas NM, Bouros D, **2006**, Exhaled markers of oxidative stress in idiopathic pulmonary fibrosis, *Eur J Clin Invest*, 36:362-7.

104. Puissant A, Fenouille N, Auberger P, **2012**, When autophagy meets cancer through p62/SQSTM1, *Am J Cancer Res*, 2:397-413.

105. Range FT, Hilker E, Breithardt G, Buerke B, Lebiedz P, **2013**, Amiodarone-induced pulmonary toxicity--a fatal case report and literature review, *Cardiovasc Drugs Ther*, 27:247-54.

106. Scherz-Shouval R, Shvets E, Fass E, Shorer H, Gil L, Elazar Z, **2007**, Reactive oxygen species are essential for autophagy and specifically regulate the activity of Atg4. *EMBO J*, 26:1749-60.

107. Selman M, Pardo A. **2002**. Idiopathic pulmonary fibrosis: an epithelial/fibroblastic cross-talk disorder, *Respir Res*, 3:3.

108. Shaid S, Brandts CH, Serve H, Dikic I, **2013**, Ubiquitination and selective autophagy, Cell Death Differ, 20:21-30.

109. Slebos DJ, Ryter SW, van der Toorn M, Liu F, Guo F, Baty CJ, Karlsson JM, Watkins SC, Kim HP, Wang X, Lee JS, Postma DS, Kauffman HF, Choi AM, **2007**, Mitochondrial localization and function of heme oxygenase-1 in cigarette smoke-induced cell death. *Am J Respir Cell Mol Biol*, 36:409-417.

110. Somani P, Bandyopadhyay S, Gross SA, Morady F, Dicarlo LA, **1987**, Amiodarone and multilamellar inclusion bodies, *Br J Clin Pharmacol*, 24:237-9.

111. Spaniol M, Bracher R, Ha HR, Follath F, Krähenbühl S, **2001**, Toxicity of amiodarone and amiodarone analogues on isolated rat liver mitochondria, *J Hepatol*, 35:628-36.

112. Stadler K, Ha HR, Ciminale V, Spirli C, Saletti G, Schiavon M, Bruttomesso D, Bigler L, Follath F, Pettenazzo A, Baritussio A, **2008**, Amiodarone alters late endosomes and inhibits SARS coronavirus infection at a post-endosomal level, *Am J Respir Cell Mol Biol*, 39:142-9.

113. Sumida M, Doi K, Ogasawara E, Yamashita T, Hamasaki Y, Kariya T, Takimoto E, Yahagi N, Nangaku M, Noiri E, **2015**, Regulation of Mitochondrial Dynamics by Dynamin-Related Protein-1 in Acute Cardiorenal Syndrome, *J Am Soc Nephrol*, pii: JASN.2014080750.

114. Tait SW, Green DR, **2012**, Mitochondria and cell signalling, *J Cell Sci*, 125:807-15.

115. Taylor MD, Antonini JM, Roberts JR, Leonard SS, Shi X, Gannett PM, Hubbs AF, Reasor MJ, **2003**, Intratracheal amiodarone administration to F344 rats directly damages lung airway and parenchymal cells, *Toxicol Appl Pharmacol*,188:92-103.

116. Uhal BD, Joshi I, Hughes WF, Ramos C, Pardo A, Selman M, **1998**, Alveolar epithelial cell death adjacent to underlying myofibroblasts in advanced fibrotic human lung, *Am J Physiol*, 275:L1192-9.

117. Uhal BD, Wang R, Laukka J, Zhuang J, Soledad-Conrad V, Filippatos G, **2003**, Inhibition of amiodarone-induced lung fibrosis but not alveolitis by angiotensin system antagonists, *Pharmacol Toxicol*, 92:81-7.

118. Van Cott TE, Yehle KS, DeCrane SK, Thorlton JR, **2013**, Amiodarone-induced pulmonary toxicity: case study with syndrome analysis, *Heart Lung*, 42:262-6.

119. Varbiro G, Toth A, Tapodi A, Bognar Z, Veres B, Sumegi B, Gallyas F Jr, **2003b**, Protective effect of amiodarone but not N-desethylamiodarone on postischemic hearts through the inhibition of mitochondrial permeability transition, *J Pharmacol Exp Ther*, 307:615-25.

120. Varbiro G, Toth A, Tapodi A, Veres B, Sumegi B, Gallyas F Jr, **2003a**, Concentration dependent mitochondrial effect of amiodarone, *Biochem Pharmacol*, 65:1115-28.

121. Vassallo P, Trohman RG, **2007**, Prescribing amiodarone: an evidence-based review of clinical indications, *JAMA*, 298:1312-22.

122. Wang J, Wang P, Li S, Wang S, Li Y, Liang N, Wang M, **2014**, Mdivi-1 prevents apoptosis induced by ischemia-reperfusion injury in primary hippocampal cells via inhibition of reactive oxygen species-activated mitochondrial pathway, *J Stroke Cerebrovasc Dis*, 23:1491-9.

123. Wang R, Ibarra-Sunga O, Verlinski L, Pick R, Uhal BD, **2000**. Abrogation of bleomycin-induced epithelial apoptosis and lung fibrosis by captopril or by a caspase inhibitor, *Am J Physiol Lung Cell Mol Physiol*, 279:L143-51.

124. Wirawan E, Vanden Berghe T, Lippens S, Agostinis P, Vandenabeele P, **2012**, Autophagy: for better or for worse, *Cell Res*, 22:43-61.

125. Wu JJ, Quijano C, Chen E, Liu H, Cao L, Fergusson MM, Rovira II, Gutkind S, Daniels MP, Komatsu M, Finkel T, **2009**, Mitochondrial dysfunction and oxidative stress mediate the physiological impairment induced by the disruption of autophagy, *Aging (Albany NY)*, 1:425-37.

126. Yasuda SU, Sausville EA, Hutchins JB, Kennedy T, Woosley RL, **1996**, Amiodarone-induced lymphocyte toxicity and mitochondrial function, *J Cardiovasc Pharmacol*, 28:94-100.

127. Yoboue ED, Devin A, **2012**, Reactive oxygen species-mediated control of mitochondrial biogenesis, *Int J Cell Biol*, 2012:403870.

128. Yun N, Cho HI, Lee SM, **2014**, Impaired autophagy contributes to hepatocellular damage during ischemia/reperfusion: heme oxygenase-1 as a possible regulator, *Free Radic Biol Med*, 68:168-77.

129. Zhang J, **2013**, Autophagy and Mitophagy in Cellular Damage Control. *Redox Biol*, 1:19-23.

10. Declaration

Hiermit erkläre ich, dass ich die vorliegende Arbeit selbständig und ohne unzulässige Hilfe oder Benutzung anderer als der angegebenen Hilfsmittel angefertigt habe. Alle Textstellen, die wörtlich oder sinngemäß aus veröffentlichten oder nichtveröffentlichten Schriften entnommen sind, und alle Angaben, die auf mündlichen Auskünften beruhen, sind als solche kenntlich gemacht. Bei den von mir durchgeführten und in der Dissertation erwähnten Untersuchungen habe ich die Grundsätze guter wissenschaftlicher Praxis, wie sie in der „Satzung der Justus-Liebig-Universität Gießen zur Sicherung guter wissenschaftlicher Praxis“ niedergelegt sind, eingehalten sowie ethische, datenschutzrechtliche und tierschutzrechtliche Grundsätze befolgt. Ich versichere, dass Dritte von mir weder unmittelbar noch mittelbar geldwerte Leistungen für Arbeiten erhalten haben, die im Zusammenhang mit dem Inhalt der vorgelegten Dissertation stehen, oder habe diese nachstehend spezifiziert. Die vorgelegte Arbeit wurde weder im Inland noch im Ausland in gleicher oder ähnlicher Form einer anderen Prüfungsbehörde zum Zweck einer Promotion oder eines anderen Prüfungsverfahrens vorgelegt. Alles aus anderen Quellen und von anderen Personen übernommene Material, das in der Arbeit verwendet wurde oder auf das direkt Bezug genommen wird, wurde als solches kenntlich gemacht. Insbesondere wurden alle Personen genannt, die direkt und indirekt an der Entstehung der vorliegenden Arbeit beteiligt waren. Mit der Überprüfung meiner Arbeit durch eine Plagiatserkennungssoftware bzw. ein internetbasiertes Softwareprogramm erkläre ich mich einverstanden.

Ort, Datum **Unterschrift**

11. Acknowledgements

First of all, I would like to express my gratitude to my supervisor, **Prof. Dr. Andreas Günther** for his guidance and support in completing my Ph.D. I also extend my sincere thanks to **Prof. Dr. Joachim Geyer** for accepting to be my co-supervisor and guiding me.

I am very much thankful to **Prof. Dr. Werner Seeger** and **Dr. Rory. E. Morty** for accepting me into the "Molecular Biology and Medicine of Lung" Programme, where I had been provided ample opportunities, to explore and talk science in-depth, with peers and world-renowned scientists. I also would like to thank **Dr. Florian Veit**, **Dr. Dorothea Peters** and all other MBML team members for their all time support. My hearty thanks to "Giessen Graduate centre for Life sciences" team as well, for enrolling me into their graduation programme, in particular to **Dr. Lorna Lueck** for her friendly guidance.

My special thanks to **Prof. Dr. Saverio Bellusci**, **Dr. Elie El Agha** and **Amit Shrestha** for their tremendous assistance in using immunofluorescence microscopy. I also would like to acknowledge **Prof. Dr. Norbert Weißmann** and **Susan Scheibe** for their support in performing ESR analysis. I also would like to thank **PD Dr. Markus O Henke** for his support.

I also want to express my thanks to my other lab members **Dr. Poornima Mahavadi, Dr. Martina Korfei, Dr. Clemens Ruppert** and **Dr. Roxana Wasnick** for their support. My special thanks to **Dr. Ingrid Henneke** and **Stefanie Hezel** for their great assistance with the animal work. I extend my gratitude to technicians **Moritz Wattenbach**, **Silke Händel** and all other students from our group for their timely helps and kind support. I also thank **Jasmin Wagner** and **Cornelia Scheld** for their help in administrative works.

My heartfelt thanks to my teachers **Dr. Shanmugasundaram, Dr. Suguna Shanmugasundaram, Dr. Shenbagarathai Rajaiah, Dr. Isabel William, Priya Rajendran, Anburani, Lourdh Mary, Kausalya Srinivasan, Sunita Gupta** and all my other beloved teachers from college and school for being highly inspirational and for nurturing self-confidence in me. My very special thanks to **Asha Kannan**, my high school biology teacher, without whom I would have never chosen biological science as my career. Thanks a lot mam for always being there for me.

Acknowledgements

Almost nothing is possible without a caring family and loving friends. I am forever thankful to my mother, **Gunasundari**, thanks a lot ma, for being there in my ups and downs and teaching me to always stand for what is right. You are my strongest pillar of support. I am also always indebted to **my grandmother, uncles, aunt, nephew and cousins** for their ever-lasting love and belief in me. My hearty thanks to **Appa, Amma, Anni** and my soulmate, **Anjan**, for their enormous love, care and support.

Finally, my loving thanks to my dear MBML friends, **Luciana, Jordi, Siva, Balram, Ivana, Mariola, Jan, Christina, Anna, Karla, Salma, Katherin** and my close buddies **Vanitha, Gopal, Prathyusha dhi, Govind anna, Abhinav, Badri anna, Priya akka, Mainu, Balaprabhu, Ranjith** and my all other friends. I would have never completed my thesis without all your support. Thank you very much guys!!!